A Measurement of the Oscillation of Neutrinos in the mode $\nu_\mu \rightarrow \nu_x$

A Dissertation Presented

by

Eric David Sharkey

to

The Graduate School

in Partial Fulfillment of the Requirements

for the Degree of

Doctor of Philosophy

in

Physics

State University of New York
at
Stony Brook

May 2002

State University of New York
at Stony Brook

The Graduate School

Eric David Sharkey

We, the dissertation committee for the above candidate for the Doctor of Philosophy degree, hereby recommend acceptance of the dissertation.

Dr. Chang Kee Jung
Advisor
Professor of Physics

Dr. Milind Diwan
Physicist

Dr. Chris Jacobsen
Professor of Physics

Dr. Robert Shrock
Professor of Physics

This dissertation is accepted by the Graduate School.

Graduate School

Abstract of the Dissertation

A Measurement of the Oscillation of Neutrinos in the mode $\nu_\mu \rightarrow \nu_x$

by

Eric David Sharkey

Doctor of Philosophy

in

Physics

State University of New York at Stony Brook

2002

A search for neutrino oscillations in the mode $\nu_\mu \rightarrow \nu_x$ was done using 4.8×10^{19} protons on target in the K2K neutrino beamline. K2K is a long baseline neutrino oscillation experiment using a neutrino beam produced at the KEK 12 GeV proton synchrotron, a near detector system at KEK and a far detector (Super–Kamiokande) in Kamioka, Japan. The experiment started taking data in 1999 and has successfully run for over two years. This corresponds to an expectation of $80.6^{+7.3}_{-8.0}$ events in the Super–Kamiokande detector in the absence of neutrino oscillations. The observation of only 56 events is sufficient to rule out the nonoscillation hypothesis at the 97% confidence level. Deviations of the observed far detector neutrino energy spectrum from predictions can rule out nonoscillation at the 68% confidence level and at the 99% when combined with the event rate analysis. The allowed region obtained in the oscillation parameter space is consistent with region published by Super–Kamiokande.

To my wife, Lisa,
who stood by me
despite my absence.

Contents

List of Figures

List of Tables

Acknowledgements

No thesis can ever be completed without the help and assistance of others and in modern high energy physics this is especially true. I owe a great deal of thanks to all of the members of K2K and Super–Kamiokande experiments, the staff of the SUNY Stony Brook Physics Department, and all of my friends and family. Mere words cannot express how grateful I am to all of these people. This section could easily be expanded to fill a volume in and of itself, but time and space constraints do not allow it.

In particular, I would like to thank my advisor, Chang Kee Jung, who has gone beyond just teaching good physics to teaching how to be a good physicist. His ever open door, loose reigns, yet watchful and caring eye have guided me along this journey.

I would also like to thank the other senior members of the Stony Brook neutrino group. Two of our post-docs, Clark McGrew and Jim Hill, have been with me for all or most of my graduate career. Among many other things, I would like to thank Clark for his insightful code and Jim for always having the time to explain anything. Our other faculty and researchers, Chiaki Yanagisawa and Kai Martens have also been helpful to me.

My entire graduate experience would have been a lot more difficult without my two trailblazers, Brett Viren and Christopher Mauger. I thank Brett for introducing me to Debian and being a fellow Linux geek in general. This thesis is modeled on Brett's own thesis and contains many elements borrowed from his description of Super–Kamiokande. I thank Christopher for sharing his verve for physics and for pulling me out of my chair, kicking and screaming, to get a little fresh air from time to time. Christopher has also gone beyond the call of duty to use his skills with the Japanese language to assist the deaf, dumb, and illiterate *gaijin* such as myself.

My time in Japan would not have been the same were it not for the KEK staff members working on K2K, especially Taku Ishida, and Makoto Sakuda. Ishida*san*'s inspiring spirit and unparalleled modesty make him a truly unique individual and I thank him for all of the support he has given to me without even realizing it. I thank Sakuda*san* for taking care of all of us foreign re-

searchers and for being the oil which keeps this experiment running smoothly. I also want to thank Yoshinari Hayato for managing to keep things running at all.

I am in debt to all the other "Americans" who have worked along side me at KEK, and Steve Boyd and Chris Walter in particular. I thank Steve for his bright and cheery disposition and catchy positive mental outlook, and Chris for his wise and sage advice both about physics and about diplomacy. Steve and Chris are largely responsible for the work on the scintillating fiber tracker which I will present in this thesis. Among many other things, I also thank Jeff Wilkes, for his web page describing maximum likelihood fitting, Hans Berns for his work on the GPS timing system, and Mark Messier for the clear description of the Super–Kamiokande oscillation analysis among other things in his thesis.

My work involving the kiloton detector would not have been possible without the guidance and support of Yoshitaka Itow. I also thank Tsuyoshi Nakaya for his clear analysis of the one kiloton fully contained data, which is also presented in this thesis.

I thank the other Stony Brook students for their help and companionship: Super–Kamiokande graduate students Florian Goebel and Matthew Malek, and the undergraduate students who have accompanied me on my many trips to Japan Rachel Reese, Brett Williams, Melissa Pawlowski[1], Toseef Raza, and Tokufumi Kato.

I would like to thank the K2K spokesperson Koichiro Nishikawa for taking charge of things and making sure that everything important got done, as well as the United States Department of Energy for allowing me to be a part of it.

Since I am notoriously bad with paperwork, I would like to send extra special thanks to those who have made sure that everything got straightened out when I needed a little help. Joan Napolitano, Alice Dugan, and Pat Peiliker have made up for many of my shortcomings.

Of course, I never could have begun this research without first passing the introductory courses, and for this I thank James Cade Bodley, without whom I likely wouldn't have survived my first year at Stony Brook.

And last, but certainly not least, I thank my wife Lisa for having the patience to stick with me, and for making it all worthwhile.

[1] now Melissa Casey

Chapter 1

Introduction

The neutrino is a fascinating particle. It's one of the most common types of particles in the universe, but because of its largely inert nature it is one of the most difficult to detect and understand.

It has been over 70 years since the conception of the neutrino, but this shy particle is still reluctant to give up its secrets.

1.1 History of Neutrino Physics

The first evidence for the existence of neutrinos came from the study of beta decay. In beta decay, as it was understood prior to 1930, an unstable atomic nucleus would emit a beta ray and transform into a new element. For example, $He^6 \rightarrow Li^6 + \beta$. In a decay of this nature, the mass of the parent nucleus is always heavier than the sum of the masses of the daughter nucleus and the beta particle. This mass difference is released as energy in the reaction, in this case, about 3.5 MeV.

The problem with this picture was that the observed energy spectrum of the released beta particles didn't conform to expectations. It is a requirement of the laws of conservation of energy and momentum that the distribution of energy between the daughter products of a two body fixed energy decay should be the same in every occurrence of that decay. This should result in a line spectrum for the beta particles of a given isotope, however what was observed was a continuous spectrum[1], varying from the predicted energy down to zero. This observation seemed to violate the principle of conservation of energy.

The solution to this problem was the introduction of the neutrino. By introducing an unseen particle in the equation $He^6 \rightarrow Li^6 + \beta + \overline{\nu}$, beta decay was no longer a two body decay, and the neutrino could carry away the energy that appeared to be missing from the beta spectrum.

On December 4, 1930, Wolfgang Pauli wrote this letter to the Tubingen congress:

> Dear Radioactive Ladies and Gentlemen,
>
> As the bearer of these lines, to whom I graciously ask you to listen, will explain to you in more detail, how because of the "wrong" statistics of the N and Li^6 nuclei and the continuous beta spectrum, I have hit upon a desperate remedy to save the "exchange theorem" of statistics and the law of conservation of energy. Namely, the possibility that there could exist in the nuclei electrically neutral particles, that I wish to call neutrons [1], which have spin 1/2 and obey the exclusion principle and which further differ from light quanta in that they do not travel with the velocity of light. The mass of the neutrons should be of the same order of magnitude as the electron mass and in any event not larger than 0.01 proton masses. The continuous beta spectrum would then become understandable by the assumption that in beta decay a neutron is emitted in addition to the electron such that the sum of the energies of the neutron and the electron is constant...
>
> I agree that my remedy could seem incredible because one should have seen those neutrons very earlier if they really exist. But only the one who dare can win and the difficult situation, due to the continuous structure of the beta spectrum, is lighted by a remark of my honoured predecessor, Mr Debye, who told me recently in Bruxelles: "Oh, It's well better not to think to this at all, like new taxes". From now on, every solution to the issue must be discussed. Thus, dear radioactive people, look and judge. Unfortunately, I cannot appear in Tubingen personally since I am indispensable here in Zurich because of a ball on the night of 6/7 December. With my best regards to you, and also to Mr Back.
>
> Your humble servant
> . W. Pauli

Despite this early prediction, direct experimental evidence for the existence of the neutrino was not revealed until 1956 when Clyde Cowan and Fred Reines

---

[1] The particle we now call the neutron wasn't discovered by Chadwick until 1932. This namespace collision was entirely coincidental. The particle which Pauli refers to as a neutron was redubbed the neutrino in 1933 by Enrico Fermi.

announced the detection of neutrinos emanating from the Savannah River nuclear power plant[2, 3].

This experiment involved inverse beta decay. In inverse beta decay, a nucleus absorbs an antineutrino, converting a proton into a neutron and a positron, as in the reaction $p+\overline{\nu} \rightarrow n+e^+$. The positron will quickly annihilate with an electron producing two gammas.

The target consisted of 10.7 ft^3 of liquid scintillator doped with cadmium chloride. Both cadmium and chlorine have large cross sections for neutron capture. Naturally occurring cadmium is a mixture of eight different stable isotopes. When exposed to neutrons, the lighter isotopes can absorb, or capture, a neutron and become an excited state of the next heaviest isotope. The nucleus will then de-excite with the emission of a few gamma rays. Although chlorine is also capable of neutron capture, the cross section for cadmium is so high that it absorbs the bulk of the neutrons. Because neutron capture cross sections increase as neutron energy decreases, the neutron typically must slow down, or thermalize, before being absorbed. This leads to a delay between the gammas observed from the e^+e^- annihilation and the neutron capture gammas.

Inverse beta decay can be easily tagged by observing the gammas from the e^+e^- annihilation followed by the gammas produced in the neutron capture a few microseconds later. Although the cross section for such a reaction is low, the enormous flux generated by the reactor was enough to observe neutrinos at a rate significantly above background.

1.1.1 The Solar Neutrino Problem

In the 1960's and '70's the focus of neutrino physics shifted from mere detection of neutrinos to more sophisticated experiments aimed at utilizing neutrinos as a probe for other areas of physics research. Ultimately these experiments would reveal as much about the neutrinos themselves as the physics they attempted to study.

Just as neutrinos are produced in radioactive decays and nuclear reactors, neutrinos are also produced inside the sun, which is really just the largest nuclear reactor in our solar system. The primary interaction that occurs in the sun is the fusion of protons into alpha particles. This doesn't occur in a single step, but occurs as a complex chain of events which results in a rather unique neutrino spectrum. It was felt that direct observation of solar neutrinos would help verify solar models.

In 1968, results from the Homestake experiment revealed that observations of the solar neutrino flux fell below predicted levels. The Homestake

experiment was based on the reaction $Cl^{37} + \nu \rightarrow Ar^{37} + e^-$. 100,000 gallons of perchloroethylene[2] (C_2Cl_4) were used as a target material and placed 4850 feet underground in the Homestake Gold Mine in South Dakota. The perchloroethylene could be processed to extract and detect individual atoms of Argon.

Using a nucleosynthesis solar model, Bahcall, Bahcall, and Shaviv [4] predicted a counting rate of 7.5 ± 3 SNU[3], but Homestake set an upper limit of 3 SNU [5]. This was the first evidence for what came to be known as the solar neutrino problem. Over time, systematic errors on both theory and experiment were reduced, but the discrepancy remained.

Many possible explanations of this problem were offered by the scientific community over the next few years, including the possibility of neutrino oscillations by Gribov and Pontecorvo in 1969 [6].

Particle oscillations may occur when a particle's energy eigenstates are a quantum mechanical mixture of two or more other observable states, such as flavor eigenstates. As the particle travels, the probability of observing one state over another will oscillate. The amount of mixing between these states can be described by a parameters called the mixing angles.

In the 1960's and 70's, neutrino oscillations as a solution for the solar neutrino problem were not well accepted since it seemed that large mixing angles were required while it was already known that mixing angles for quarks were small.

In the 1980's and 90's radiochemical experiments using gallium targets (SAGE[7], Gallex[8]) and electronic experiments using water targets (Kamiokande, Super–Kamiokande) confirmed the deficit in the observed flux. Figure 1.1 summarizes experimental results to date.

1.1.2 The Atmospheric Neutrino Anomaly

Another natural source of neutrinos is cosmic radiation. Cosmic rays entering the atmosphere are primarily protons. When these high energy cosmic ray protons strike the Earth's atmosphere, a nuclear reaction can occur which ultimately results in neutrino production. Unlike solar neutrinos or neutrinos produced in radioactive decays, which are all electron type neutrinos, atmospheric neutrinos come in both electron type and muon type varieties.

---

[2]This is essentially dry cleaning fluid. Neutrino experiments are truly a case where Woolite just won't do.

[3]SNU stands for Solar Neutrino Unit and is equivalent to 10^{-36} captures per target atom per second.

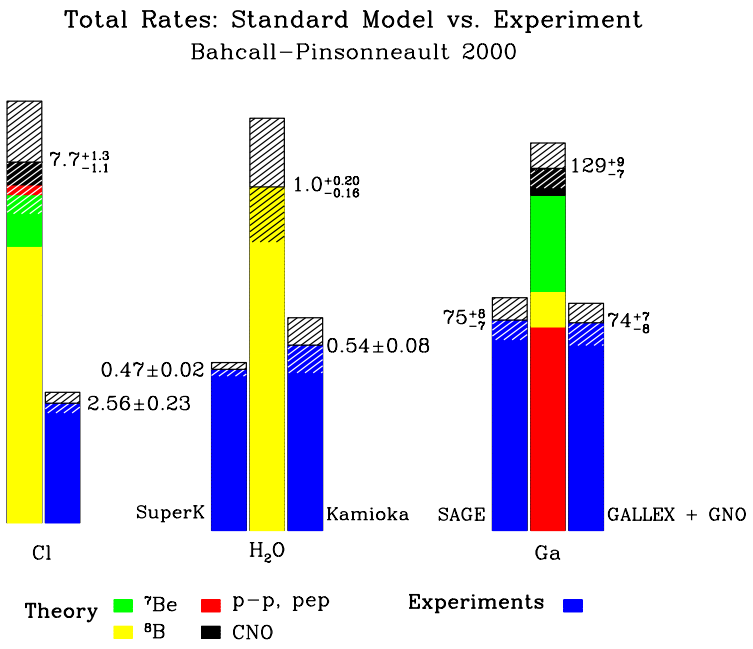

Figure 1.1: This figure summarizes the expected solar neutrino event rate for three different detector types. [9] Beside each prediction are the observations by corresponding experiments. Colors indicate the component reactions which are responsible for the generation of observable neutrinos in each detector, while hatched regions indicate experimental or theoretical error.

The most common particles produced by protons colliding with nuclei are pions. In nearly all cases pions decay to muons, and muons to electrons. In each case where a lepton is produced in such a decay, a balancing antilepton of the same flavor must also be produced if lepton flavor number is to be conserved. This decay chain, along with the corresponding decays of the π^+, is responsible for the bulk of atmospheric neutrino production.

$$\pi^- \rightarrow \mu^- + \overline{\nu}_\mu$$
$$\mu^- \rightarrow e^- + \nu_\mu + \overline{\nu}_e$$

It is then clear that muon type neutrinos should be expected to outnumber electron type neutrinos by approximately two to one. The exact ratio depends on neutrinos produced from the decay of other particles (primarily kaons) and the number of muons which will reach the earth's surface without decaying, but even with these factors included, the expected ratio is still about 2:1 for neutrino energies less than 5 GeV.

Atmospheric neutrinos provide an interesting probe into the possibility of neutrino oscillation because, unlike solar neutrino studies, it is not necessary to know the absolute flux or neutrino interaction cross sections as precisely. When calculating expected flavor ratios in the presence of oscillations, these quantities largely cancel out.

While the solar neutrino spectrum has a mean energy of just a few MeV, atmospheric neutrinos typically have a much higher energy. Because of this, the radiochemical techniques used in the Homestake, SAGE, and Gallex experiments are not appropriate. While earlier experiments had observed the presence of atmospheric neutrinos[11, 12] the first two experiments seriously study them were IMB[13, 14] and Kamiokande[15, 16] built in 1982 and in 1983 respectively. Both of these experiments followed similar designs, each consisting of a large tank of water surrounded by photomultiplier tubes which could detect Čerenkov radiation emitted by high energy particles. Built with the primary purpose of looking for proton decay, these detectors had to deal with "background" events generated by atmospheric neutrinos.

Studies of this atmospheric neutrino background did not show the expected flavor ratio. To take out detector effects, each experiment calculated a double ratio, R, defined as the observed flavor ratio divided by the observation predicted by a Monte Carlo simulation.

$$R = \frac{\mu_{DATA}/e_{DATA}}{\mu_{MC}/e_{MC}}$$

Here, μ_{DATA} represents the number of observed muon-like events while μ_{MC} represents the predicted number of such events in a Monte Carlo simulation assuming no oscillation. Likewise, e_{DATA} and e_{MC} are the observed and predicted electron-like events.

IMB measured R=$0.54 \pm 0.05 \pm 0.07$, which was consistent with Kamiokande's measurement of 0.60 ± 0.06. Neither experiment was consistent with the expectation of R=1.0.

Again, as with the solar neutrino experiments, there appeared to be a problem with the observed atmospheric neutrino interaction rates. The predicted number of muon neutrinos was thought to be well known relative to electron neutrinos, but experiments were only detecting about half the expected number of muon type neutrinos. This became known as the atmospheric neutrino anomaly and was considered as further evidence for neutrino oscillation.

Later experiments using iron targets (Soudan[17], Frejus[19, 20]) initially saw no such discrepancy. In 1996 Super–Kamiokande, the successor experiment to Kamiokande, went online and confirmed the results of previous water Čerenkov experiments at a much higher precision, measuring R=$0.65 \pm 0.02 \pm$

0.05 for sub-GeV events, and R=$0.67 \pm 0.03 \pm 0.08$ for multi-GeV events. It appeared that there was a disagreement between the water target and iron target experiments, but as time passed and statistics improved, the Soudan measurement dropped to $0.68 \pm 0.11 \pm 0.06$[18]. Figure 1.2 shows a summary of these results.

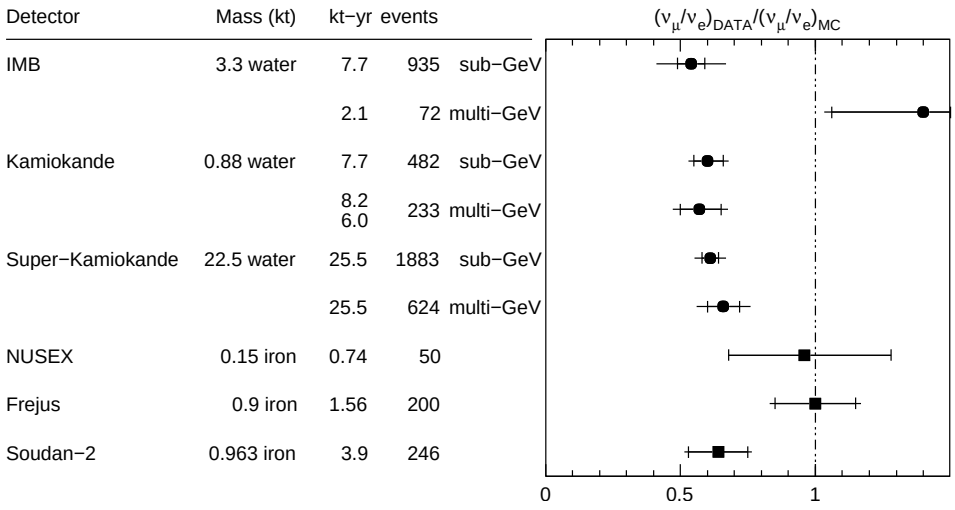

Figure 1.2: Summary of some observations of the atmospheric neutrino double ratio, R. $R = 1$ is perfect agreement with standard model predictions.

1.2 Neutrino Oscillations

I've now mentioned neutrinos and neutrino oscillations several times without providing a rigorous definition. This section will give an introduction of the standard model of particle physics and overview of neutrinos oscillation.

1.2.1 Neutrinos in the Standard Model

Physicists refer to the leading explanation of particles and fields as we know them as the *standard model*. The standard model consists of a collection of elementary particles and rules for their interactions.

Table 1.1 shows the standard model's elementary fermions. Fermions are what most people think of as ordinary matter. They obey the Pauli exclusion principle which states that no two fermions can occupy the same space at the

Leptons		
Flavor	Q	Mass
ν_e (electron neutrino)	0	< 15 eV/c^2
e (electron)	-1	0.511 MeV/c^2
ν_μ (muon neutrino)	0	< 0.19 MeV/c^2
μ (muon)	-1	105.7 MeV/c^2
ν_τ (tau neutrino)	0	< 18 MeV/c^2
τ (tau)	-1	1.78 GeV/c^2

Quarks		
Flavor	Q	Mass
u (up)	+2/3	$\sim$3 MeV/c^2
d (down)	-1/3	$\sim$6 MeV/c^2
c (charm)	+2/3	$\sim$1.3 GeV/c^2
s (strange)	-1/3	$\sim$100 MeV/c^2
t (top)	+2/3	$\sim$175 GeV/c^2
b (bottom)	-1/3	$\sim$4.3 GeV/c^2

Table 1.1: Lepton and Quark summary

same time with the same quantum numbers. Anything you can pick up and touch is composed of fermions.

In contrast to the fermions, the gauge bosons listed in Table 1.2 may coexist in any number at the same place and time. Gauge bosons are usually thought of as force carriers. They are responsible for mediating the four fundamental forces: electromagnetism, the weak force, the strong force, and gravity.

Force	Particle	Mass	Charge
Electro-magnetic	γ (photon)	0	0
Weak	W^-	80.4 GeV/c^2	-1
	W^+	80.4 GeV/c^2	+1
	Z^0	91.2 GeV/c^2	0
Strong	8 $\times$ g (gluon)	0	0
Gravity	graviton	0	0

Table 1.2: Force carrier summary

We can divide the fermions into two categories called quarks and leptons. Quarks are particles which don't exist in isolation but can combine to form mesons and baryons, including protons and neutrons. Quarks can interact with all of the bosons so quarks can be affected by all of the fundamental forces. By contrast leptons can be free particles but they don't interact with gluons, so they're not affected by the strong force.

Leptons come in both charged and uncharged varieties. The charged leptons are the electron, muon and tau particles, while the uncharged leptons are their corresponding neutrinos. Since the carrier of the electromagnetic force, the photon, can only interact with charged particles, neutrinos are not affected

by the electromagnetic force. In order to detect neutrinos, we must rely on the weak force, which is why neutrinos are so difficult to measure.

1.2.2 The Physics of Oscillations

Particle oscillations are a purely quantum mechanical phenomenon. Oscillation between two or more quantum mechanical states may occur if the states are of different energies and are not themselves energy eigenstates. In general, particles created in weak interactions are not created in energy eigenstates. Since neutrinos are only created in weak interactions, it's not surprising that their flavor eigenstates, which we denote as $|\nu_e\rangle$, $|\nu_\mu\rangle$, and $|\nu_\tau\rangle$, are not necessarily energy eigenstates, which we shall call $|\nu_1\rangle$, $|\nu_2\rangle$, and $|\nu_3\rangle$.

Each set of states, the flavor eigenstates and the energy eigenstates, forms a basis for describing the set of particles known as neutrinos. Each state in one basis may be represented as a linear combination of states in the other basis. In this sense, each energy eigenstate is said to be a mixture of the flavor eigenstates and vice versa. If the coefficients in this linear combination are not strictly 1 or 0, then the states are said to mix.

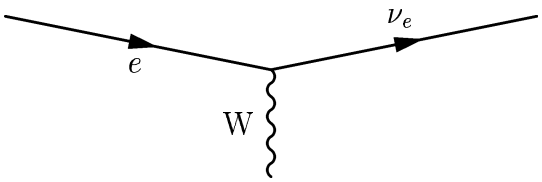

Figure 1.3: Feynman diagram depicting neutrino production via the weak interaction. A charged lepton, such as an electron, may emit a W, leaving a neutrino.

For simplicity, let us temporarily neglect $|\nu_\tau\rangle$ and consider two flavor mixing between $|\nu_e\rangle$ and $|\nu_\mu\rangle$. Considering all three generations simultaneously is not fundamentally different, but it is more complicated.

We can express the flavor eigenstates in terms of the energy eigenstates by the introduction of a parameter, θ, called the mixing angle.

$$|\nu_\mu\rangle = \sin(\theta)|\nu_1\rangle + \cos(\theta)|\nu_2\rangle$$

$$|\nu_e\rangle = \cos(\theta)|\nu_1\rangle - \sin(\theta)|\nu_2\rangle$$

For time independent Hamiltonians, the time evolution operator is:

$$\mathcal{U}(t, t_0) = \exp\left[\frac{-iH(t-t_0)}{\hbar}\right] = e^{-iE(t-t_0)/\hbar}$$

$$\mathcal{U}(t)|\nu_\mu; t_0\rangle = |\nu_\mu; t\rangle$$

The probability of observing an electron neutrino from what was once a pure muon neutrino, $P_{\nu_\mu \to \nu_e}$, is then given by:

$$|\langle\nu_e|\nu_\mu; t\rangle|^2$$

$$|\nu_\mu; t\rangle = e^{-iE_1 t/\hbar}\sin(\theta)|\nu_1\rangle + e^{-iE_2 t/\hbar}\cos(\theta)|\nu_2\rangle$$

$$\begin{aligned}
|\langle\nu_e|\nu_\mu; t\rangle|^2 &= |\cos(\theta)\sin(\theta)(e^{-iE_1 t/\hbar} - e^{-iE_2 t/\hbar})|^2 \\
&= \frac{1}{2}\sin^2(2\theta)[1 - \cos((E_1 - E_2)t/\hbar)] \\
&= \sin^2(2\theta)\sin^2(\frac{1}{2}(E_1 - E_2)t/\hbar) \\
&= \sin^2(2\theta)\sin^2((\sqrt{m_1^2 + p^2} - \sqrt{m_2^2 + p^2})t/2\hbar)
\end{aligned}$$

If $E_1, E_2 \gg m_1, m_2$ then this can be approximated by:

$$\approx \sin^2(2\theta)\sin^2((m_1^2 - m_2^2)L/4\hbar cE)$$

Expressing this in terms of quantities relevant to this experiment we find the familiar oscillation formula:

$$P_{\nu_\mu \to \nu_e} = \sin^2(2\theta)\sin^2(1.27 \times L/E \times \Delta m^2) \tag{1.1}$$

where L is the distance between the detectors (in km) and E is the neutrino energy (in GeV) and Δm^2 is the difference in the square of the neutrino masses (in eV^2).

To expand this derivation to three flavor oscillations it's necessary to replace single mixing angle θ with three independent mixing angles, θ_{12}, θ_{13}, and θ_{23}, as well as one additional complex phase factor. These angles can be used to form a CKM style unitary mixing matrix as follows:

$$\begin{pmatrix}
c_{12}c_{13} & s_{12}c_{13} & s_{13} \\
-s_{12}c_{23} - c_{12}s_{23}s_{13} & c_{12}c_{23} - s_{12}s_{23}s_{13} & s_{23}c_{13} \\
s_{12}s_{23} - c_{12}c_{23}s_{13} & -c_{12}s_{23} - s_{12}c_{23}s_{13} & c_{23}c_{13}
\end{pmatrix}$$

where s_{ij} and c_{ij} stand for $\sin(\theta_{ij})$ and $\cos(\theta_{ij})$ respectively. Likewise we need two independent values of Δm^2: Δm^2_{12} and Δm^2_{23}. Δm^2_{13} is obviously just the sum of Δm^2_{12} and Δm^2_{23}. In the general case of N neutrinos, there are $N-1$ values of Δm^2, $(N^2-N)/2$ values of θ, and $N-2$ complex phase factors.

1.2.3 Previous Measurements of Oscillations

Prior to the design and construction of K2K, there were several measurements made by other experiments which were suggestive of neutrino oscillations. As mentioned previously, one possible solution of the solar and atmospheric neutrino anomalies was neutrino oscillation, but "missing neutrinos" alone are not enough to tag oscillation as the only possible explanation.

One advantage the electronic experiments have over their radiochemical cousins is the ability to estimate neutrino direction. Although the neutrino itself is not observed, the direction of the charged lepton created during an interaction can be accurately measured. Although the charged lepton direction is nearly isotropic in the center of mass frame, the Lorentz boost will orient these leptons toward the direction of the neutrino in the lab frame. As the neutrino energy increases, the correlation between neutrino direction and charged lepton direction improves.

Atmospheric neutrinos detected going downward have only traveled the short distance from the upper atmosphere to the earth's surface ($15 \sim 30$ km), while neutrinos traveling upward have traveled the entire diameter of the earth. The oscillation probability in Equation 1.1 varies sinusoidally with L. If oscillation were to explain the atmospheric neutrino anomaly, we might see this variation in the measured flux as a function of the neutrino's angle relative to the vertical, also known as the zenith angle. The zenith angle distributions measured by Super–Kamiokande are shown in Figure 1.5. For certain sets of oscillation parameters, we would expect an R value of 1 at small angles and deviations from 1 at larger angles. Figure 1.6 shows the Super–Kamiokande measurement of the zenith angle dependence of the double ratio.

The zenith angle dependence can also be seen in the upward going muon angle distribution. An upward going muon is defined as any muon observed with a zenith angle less than 90°. Downward going muons are primarily cosmic ray muons which manage to penetrate the rock overburden, but no muon can penetrate the entire earth. Upward going muons are the result of neutrino interactions in the rock beneath the detector. Figure 1.7 shows the Super–Kamiokande upward going muon distribution.

When the zenith angle and upward going muon distributions are taken in conjunction with the flavor ratio, a fit can be made to determine the two

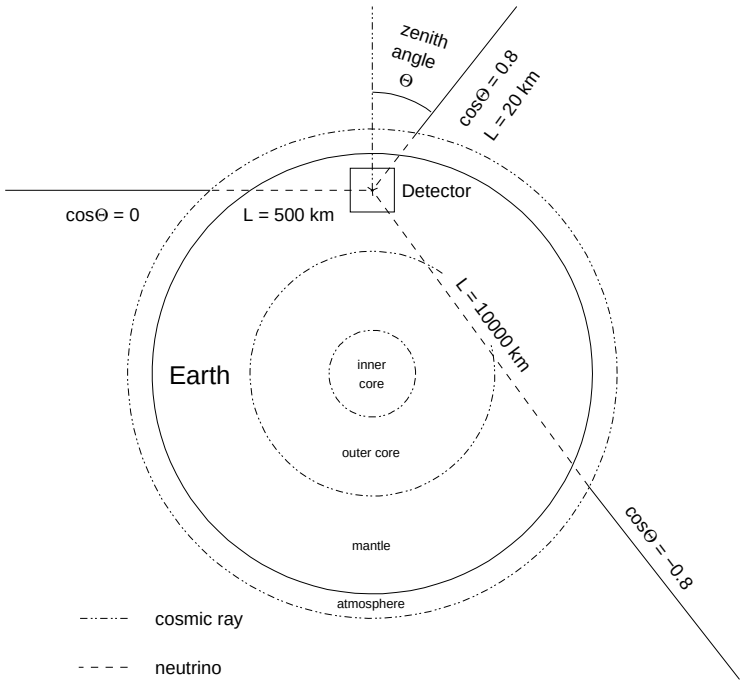

Figure 1.4: Neutrinos with different zenith angles will have traveled different distances before striking the detector.

free parameters in the oscillation probability, the mixing angle and the mass square difference. Traditionally we plot this in the parameter space formed by Δm^2 and $\sin^2(2\theta)$. A summary of the results from fits to the data from Super–Kamiokande along with other experiments are shown in Figure 1.8 for $\nu_\mu \to \nu_e$ and Figure 1.9 for $\nu_\mu \to \nu_\tau$. With the double ratio, zenith angle, and upward going muon distributions all in agreement, the Super–Kamiokande collaboration formally announced evidence for neutrino oscillation in 1998[21].

Another experiment to announce a positive signal for neutrino oscillation was the Liquid Scintillator Neutrino Detector experiment (LSND)[22, 23] at the Los Alamos Meson Physics Facility. This experiment used a proton beam on a water target to produce pions. The pions decayed in flight via $\pi^+ \to \mu^+ + \nu_\mu$. The resulting muons were then trapped in a beam stop and decayed at rest via $\mu^+ \to e^+ + \nu_e + \overline{\nu}_\mu$. Both decays were studied and examined for the presence of excessive numbers of electron-like events which would be a signal for $\nu_\mu \to \nu_e$ oscillations. LSND reported an observation of 40 events with an expected background of 21.9 ± 2.1 for decay in flight, and 22 events with a background of 4.6 ± 0.6 for decay at rest.

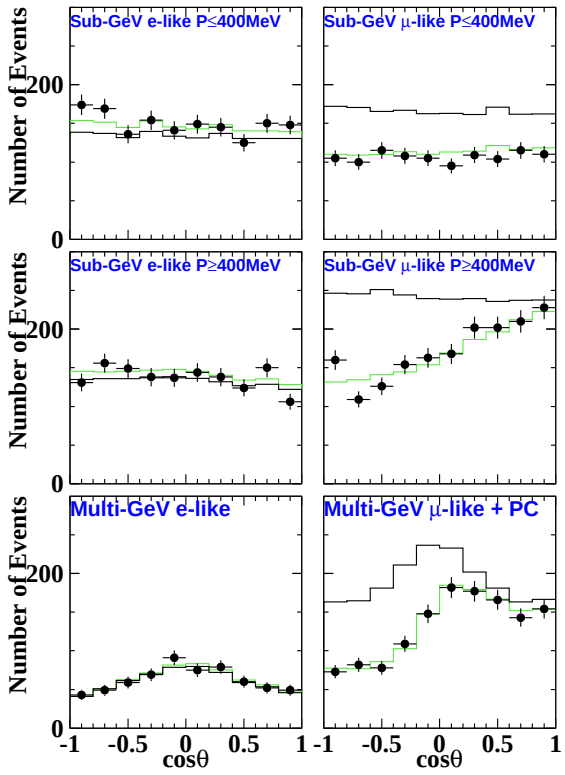

Figure 1.5: Super–Kamiokande neutrino zenith angle distributions. Upward-going particles have $\cos\Theta < 0$ and downward-going particles have $\cos\Theta > 0$. The solid black line shows the Monte Carlo expectation for no oscillations normalized to the data live-time. The grey line is the best-fit expectation for $\nu_\mu \leftrightarrow \nu_\tau$ oscillations with the overall flux normalization fitted as a free parameter.

This result is somewhat troubling. We've seen that with three neutrino flavors, there are only two independent values of Δm^2. However, as can be seen in Figures 1.8 and 1.9, the value of Δm^2 required by LSND is much larger than those suggested by solar and atmospheric neutrino observations. Thus, in order for all experiments to be consistent, there would need to be at least three independent values of Δm^2 and four mass eigenstates. Furthermore, large chunks of the LSND allowed region have been ruled out by other experiments such as BNL E-776[24], KARMEN[25], and CHOOZ[26]. There has also been some controversy over the purity of the early LSND events[27, 28]. It is hoped that this controversy will be resolved by MiniBooNE, a Fermilab experiment with a sensitivity covering the LSND allowed region completely. MiniBooNE

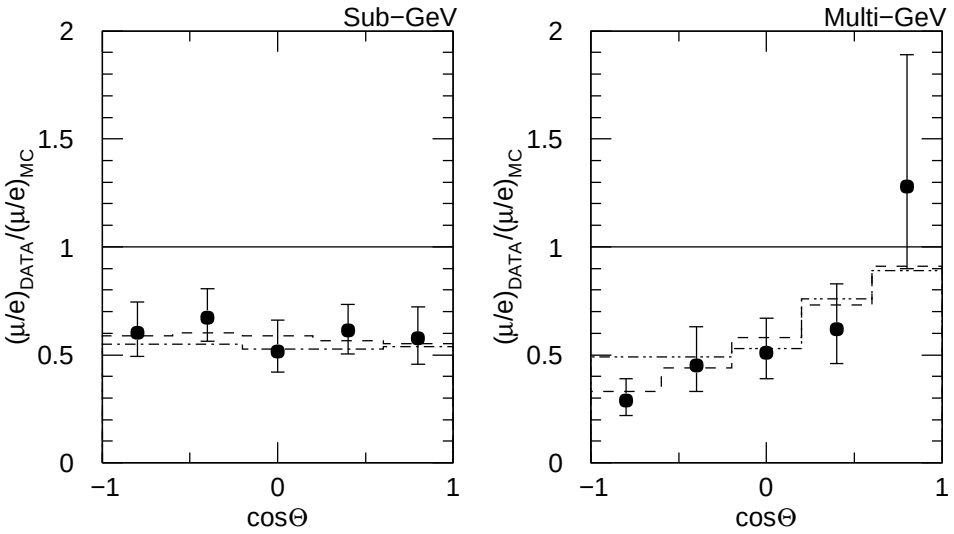

Figure 1.6: The Super–Kamiokande zenith angle distribution of the ratio $(\mu/e)_{exp}/(\mu/e)_{MC}$. In the left panel, the dashed curve is the best neutrino oscillation fit to the full data set, while the dot-dash line is the sub-GeV sample alone. In the right panel, the line histograms are the expectations from the neutrino oscillations, in the mode $\nu_\mu \to \nu_e$ (dashed) or $\nu_\mu \to \nu_\tau$ (dotted), with the best fit values of parameter region. In the absence of oscillations these figures should be flat at 1.

plans to start taking data in 2002.

1.3 Nailing Down Neutrino Oscillations with a Controlled Beam

Although previous experiments have demonstrated strong evidence for neutrino oscillation, it is important to confirm or deny this evidence by further experimentation. For this reason, the KEK to Kamioka, or K2K, experiment was designed and constructed.

K2K will duplicate many of the conditions of the atmospheric neutrino measurements but with fewer unknowns. The first long baseline experiment of its kind, the K2K experiment seeks to use a pure beam of artificially produced muon neutrinos aimed at the Super–Kamiokande detector. The path length of the neutrinos, L, will be known precisely, and the initial flux, flavor ratio, and energy spectrum will be measured at the beam's creation point by a near detector system. By using Equation 1.1 it is then possible to deduce possible

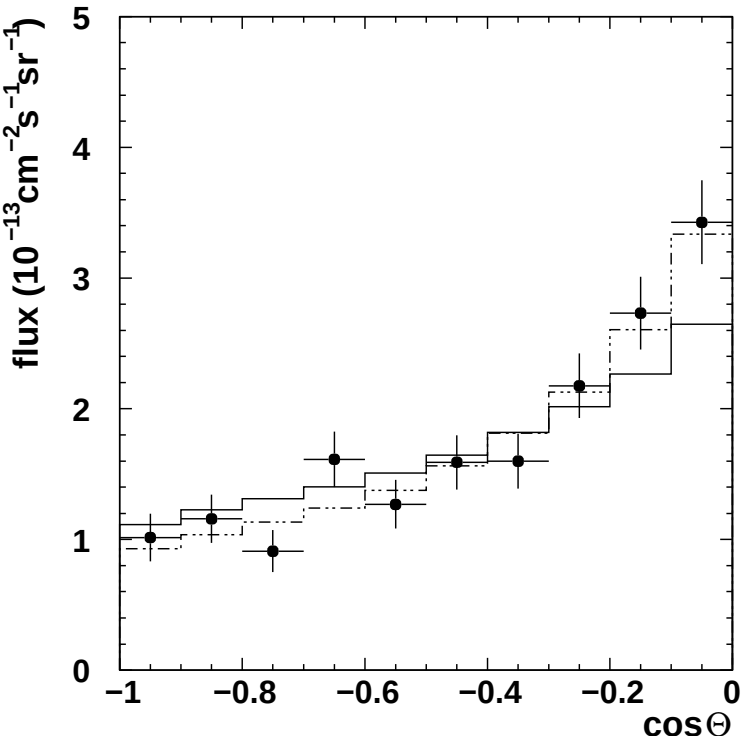

Figure 1.7: The Super–Kamiokande upward going muon zenith angle distribution. The solid line is the expectation for the shape in the absence of oscillations (the normalization has been allowed to float). The dashed line is with an oscillation fit.

values of $\sin^2(2\theta)$ and Δm^2.

1.4 The K2K and Super–Kamiokande Collaborations

Discussion of the K2K experiment cannot be held without the inclusion of the Super–Kamiokande experiment. Although there is a large overlap in equipment, software, and personnel, the K2K collaboration and the Super–Kamiokande collaboration are separate entities with independent sources of funding and separate governing bodies.

The Super–Kamiokande collaboration consists of 22 institutions and about 125 physicists, primarily from Japan and the United States with a few from Poland and Korea. The host institution is the Institute for Cosmic Ray Re-

search (ICRR) of the University of Tokyo.

The K2K collaboration consists of about 100 physicists from 19 institutions in Japan, the United States, Korea, and Poland. The experiment is jointly hosted by Japan's High Energy Accelerator Research Organization, or KEK[4] for short, and the University of Tokyo.

[4]KEK originally stood for *Ko Enerugi Kenkyujo* which translates to High Energy Laboratory, but the expansion of KEK has since been changed to *Ko Enerugi Kaso-kuki Kankyu-kiko* (High Energy Accelerator Research Organization).

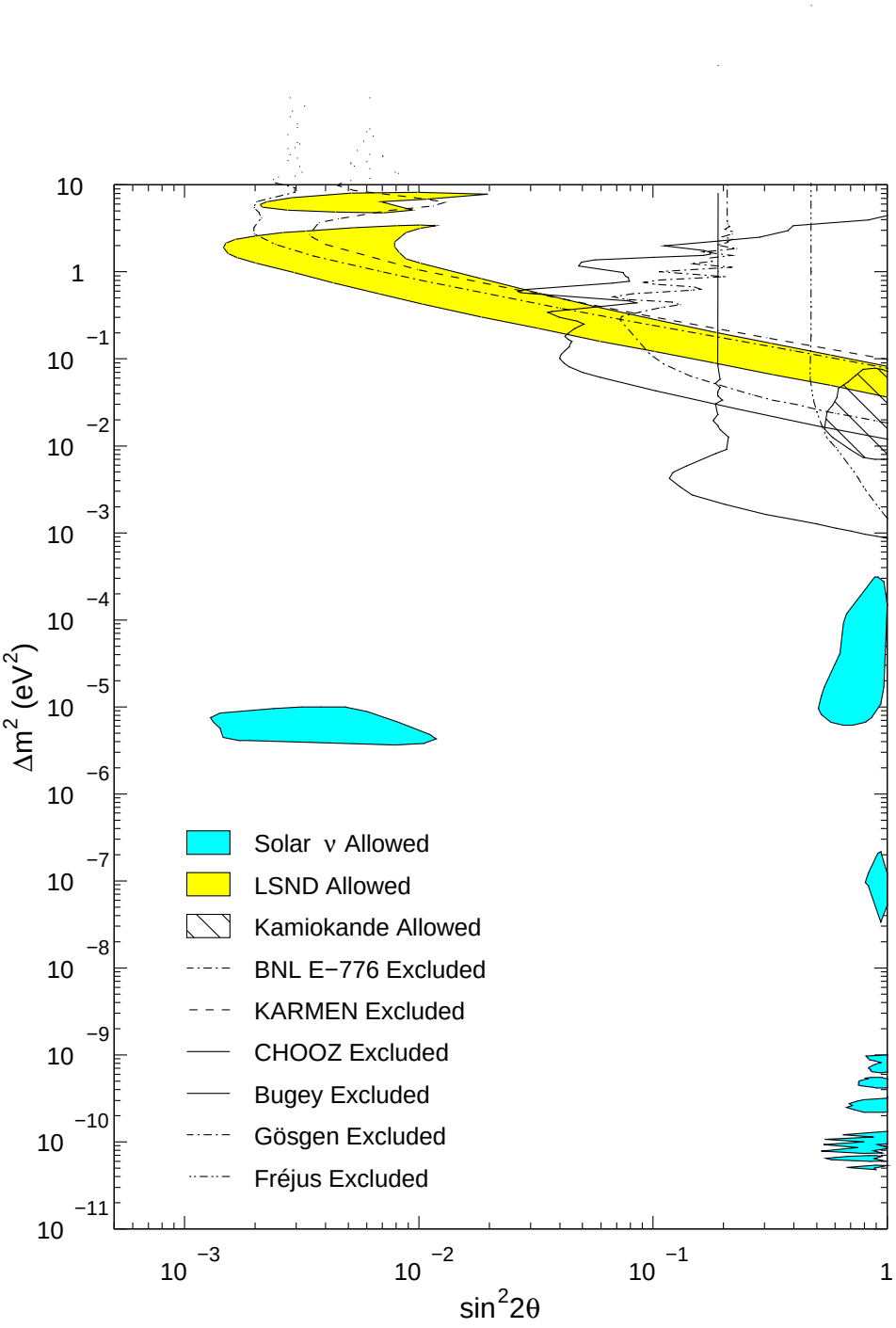

Figure 1.8: $\nu_\mu \rightarrow \nu_e$ neutrino oscillation parameter allowed and excluded regions for many recent neutrino experiments. Exclusion regions all exclude regions to the right of the curve.

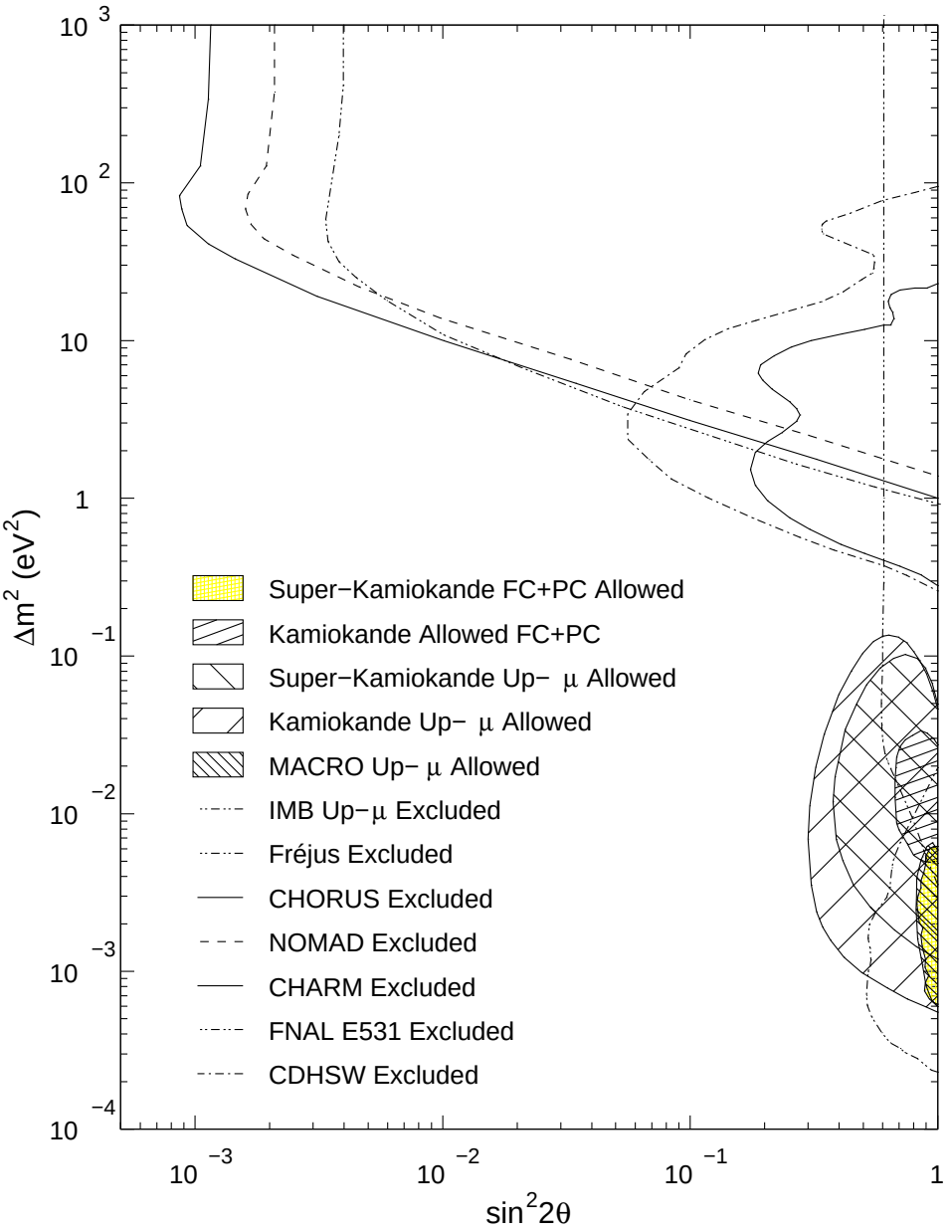

Figure 1.9: $\nu_\mu \rightarrow \nu_\tau$ neutrino oscillation parameter allowed and excluded regions for Super–Kamiokande and other experiments. Exclusion regions all exclude regions to the right of the curve.

Chapter 2

The K2K Long Baseline Experiment

The primary purpose of the K2K Experiment is to study neutrino oscillations. The basic idea is to produce a beam of muon neutrinos which will pass through two detector systems, each capable of measuring neutrino flux as a function of flavor and energy. The measurement in the first, or near, detector will be used to extrapolate a prediction for the flux at the second, or far, detector. The comparison of the predicted and observed fluxes can be used to determine if neutrino oscillation is taking place. A schematic layout of the experiment is shown in Figure 2.1.

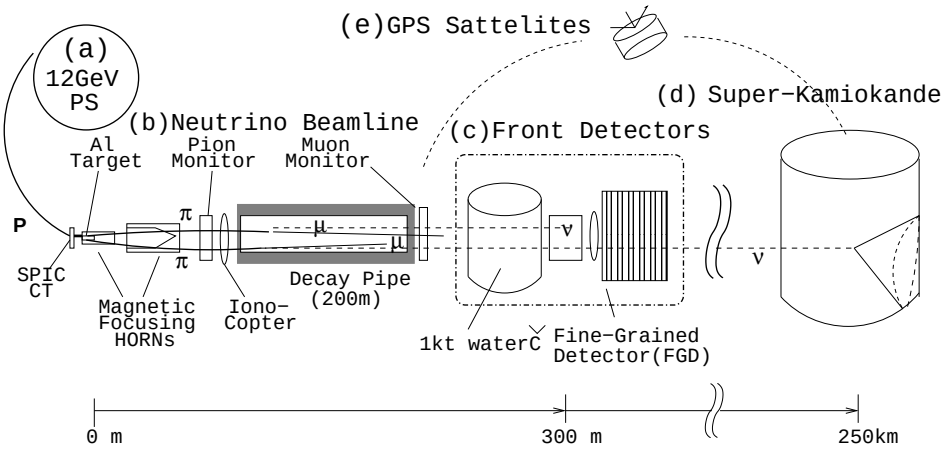

Figure 2.1: General Overview of the K2K Experiment

The design parameters of the K2K experiment (beamline length, energy spectrum, etc.) were optimized to be most sensitive to the oscillation parameter space suggested by the Kamiokande experiment, which was the most significant result at the time. The expected sensitivity is shown in Figure 2.2. Newer results from the Super–Kamiokande collaboration suggest lower values

of Δm^2 for which K2K is not well optimized, however it is still possible to probe large portions of the Super–Kamiokande allowed region.

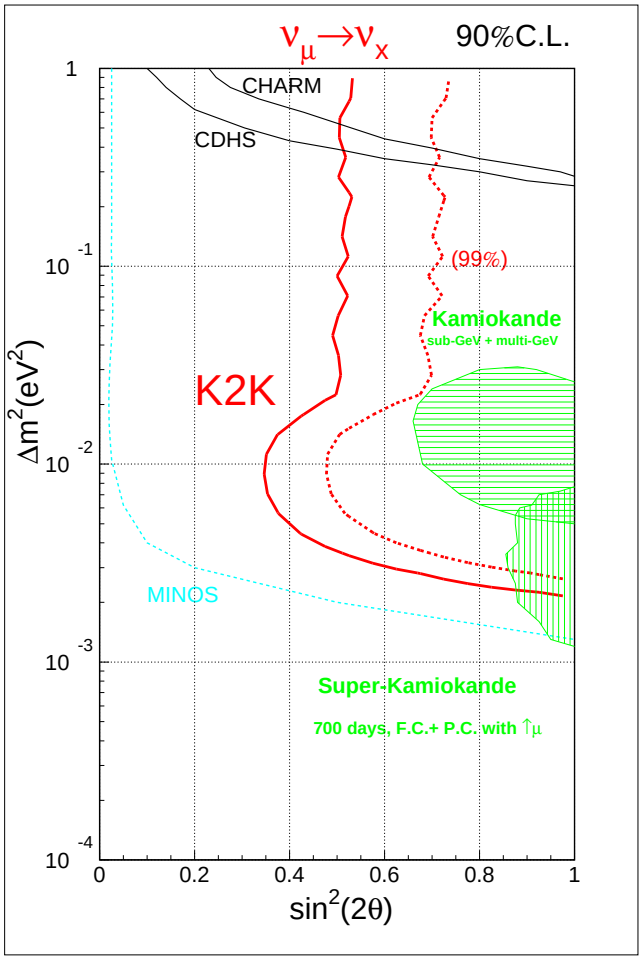

Figure 2.2: Expected sensitivity of the K2K experiment for $\nu_\mu \rightarrow \nu_x$. CDHS and Charm were experiments which took place at CERN in the 1970's and 80's. The MINOS experiment is a successor to K2K and is scheduled to take data in 2005.

2.1 The Neutrino Beam and Beam Monitors

The K2K neutrino beam is created by slamming protons from the KEK proton synchrotron onto a fixed aluminum target. Large numbers of pions along with other hadrons will be produced in these collisions. The pions are

focused by a pair of horn magnets and allowed to travel down a decay pipe. The pions then decay into predominantly muons and muon type neutrinos. The muons are absorbed by a beamstop, but the neutrinos continue on to form the K2K neutrino beam. In order to understand the beam properties, careful measurements are made of the protons, pions, and muons produced at various positions along the beam path.

2.1.1 The KEK Proton Synchrotron

The KEK proton synchrotron is 339 meters in circumference and can store 9 bunches of about 6×10^{11} protons each. The protons are ramped up to a kinetic energy of 12 GeV over the course of 2.2 seconds and then fast extracted from the accelerator in a single turn. The accelerator is immediately refilled and the process repeats. We refer to each extraction of nine bunches as one spill. Figure 2.3 shows the time structure of a single spill. Each spill lasts 1.1 μs with about 30 ns separating each bunch.

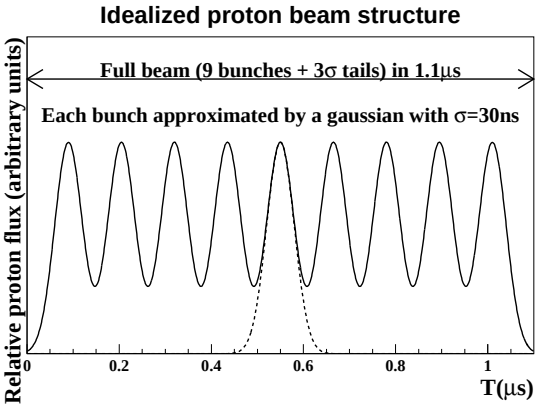

Figure 2.3: Idealized beam timing

2.1.2 The Target and Horns

The proton target is a 60 cm long cylindrical aluminum rod with a 3 cm diameter. It is embedded in the upstream part of the axis of the first horn. Figure 2.4 shows the target station. Each horn is hollow and carries a current of 250 kA which is pulsed to avoid excessive heating and reduce the electrical cost. The current travels down the outside of each horn and is

returned along the center. This sets up a circular magnetic field inside each horn. The field appears to run counter-clockwise when looking downstream so it will tend to bend positively charged particles toward the beam center and negatively charged particles away. The horns are carefully shaped so that particles moving out from the target at large angles will spend more time in the magnetic field region than particles moving mostly forward. This property allows for the direction of the maximum possible number of pions down the beamline.

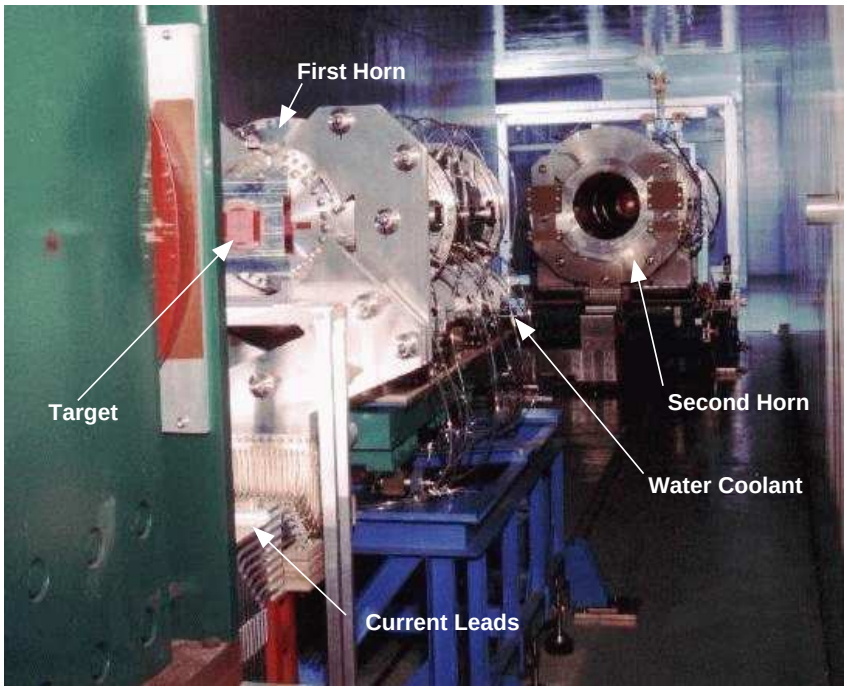

Figure 2.4: K2K Target and Horn Magnets

2.1.3 The Pion Monitor

In order to ensure an accurate prediction of the flux at Super–Kamiokande, it is necessary to know as much about the neutrino beam as possible. To this end, beam monitoring detectors have been constructed.

The pion monitor is a ring imaging gas Čerenkov counter. The pion monitor measurement is destructive, so this detector is only inserted into the beam periodically to check beam properties. It consists of a large gas volume containing a wedge shaped segment of a spherical mirror. As the pions created

at the target pass through the gas, Čerenkov light is emitted, reflected off the mirror, and focused on an array of photomultiplier tubes (PMTs).[1] Figure 2.5 shows a schematic depiction of the pion monitor.

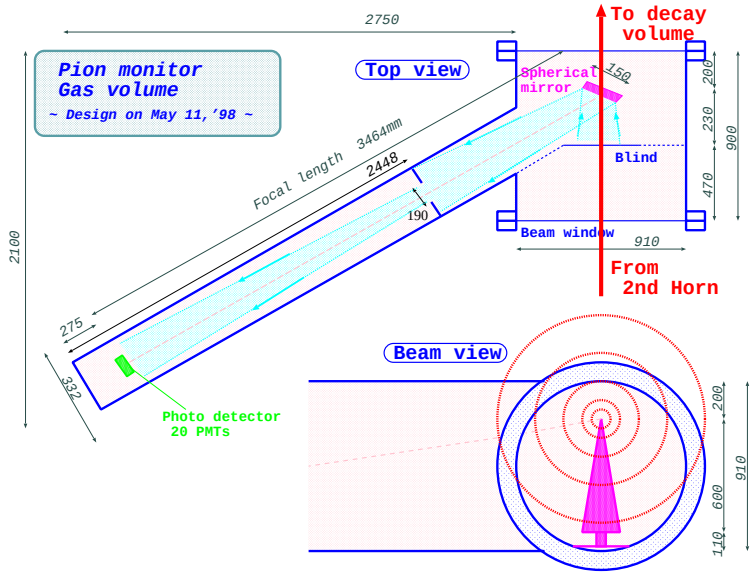

Figure 2.5: Pion Monitor Schematic. The pion monitor consists of gas volume containing a spherical mirror segment which reflects Čerenkov light to an array of PMTs which sit outside the pion beam. The point of the mirror wedge is aligned with the center of the beam.

Čerenkov radiation [29, 30] is a very useful phenomenon for building detectors for high energy physics experiments. When an electrically charged particle passes through a medium composed of other charged particles there is an interaction between the electromagnetic fields. Furthermore, in such a medium, the effective propagation time of an electromagnetic field will be lengthened due to interactions with the medium, effectively reducing the speed of light. If a particle is traveling faster than the effective speed of light, its own electromagnetic field will interfere with itself constructively and produce Čerenkov photons.

For a particle of a given speed, the direction of the Čerenkov photons is fixed relative to the particle's own motion. This angle is given by Equation 2.1.

[1] PMTs will be described in detail in Section 2.2.4.

$$\cos\theta_c = \frac{1}{\beta n(\lambda)}, \tag{2.1}$$

Here β is the speed of the particle in units of c and $n(\lambda)$ is the index of refraction of the medium at a wavelength of λ.

This fixed direction is critical. As the particles move through the pion monitor, the Čerenkov photons for a given particle are reflected into a ring pattern by the mirror, *regardless of of the position of the particle.* The pattern of Čerenkov light is recorded by a strip of photomultiplier tubes. Particles of different speeds will produce rings of differing size, while particles of differing direction will produce rings with a different center. By adjusting the index of refraction of the gas, it is possible to deconvolve these effects and reconstruct the distribution of both the speed and direction of the particles. Furthermore, since the pions move faster than the protons, it is possible to measure the distribution of pion momenta and angles without interference from protons. The distributions of Čerenkov light and final derived momentum distribution are shown in Figures 2.6 and 2.7.

2.1.4 The Ionocopter

One of the problems with the pion monitor is that it can only measure the vertical component of the angle of particles relative to the central beam direction and can't even see the upper portion of the beam at all. In order to build its momentum distribution, cylindrical symmetry must be assumed. It's desirable to know whether this assumption is justified. The "ionocopter" was designed and constructed to measure this symmetry.

The basic idea is simple. Take two ionization chambers and spin them around. We assume that each spill produces a similar distribution of particles, so by rotating a set of chambers around the beam, the relative intensity of different segments in ϕ can be easily mapped out. Figure 2.8 shows a picture of the device.

As with the pion monitor, the ionocopter's measurement is destructive to the beam, so it's only rolled in occasionally. The ionocopter has two ionization chambers, each with 22 5 cm square pads arranged in a 2×11 grid. The detector spins around the beam axis and has a 220° range of motion, allowing overlap in the sensitive region of the two chambers. This overlap allows for relative calibration of chamber sensitivity. The relative sensitivity of individual pads can be checked by moving the detector horizontally ± 5 cm.

In initial runs, the angular position of the detector was recorded by an optical position encoder, but the electronics contained in this device failed

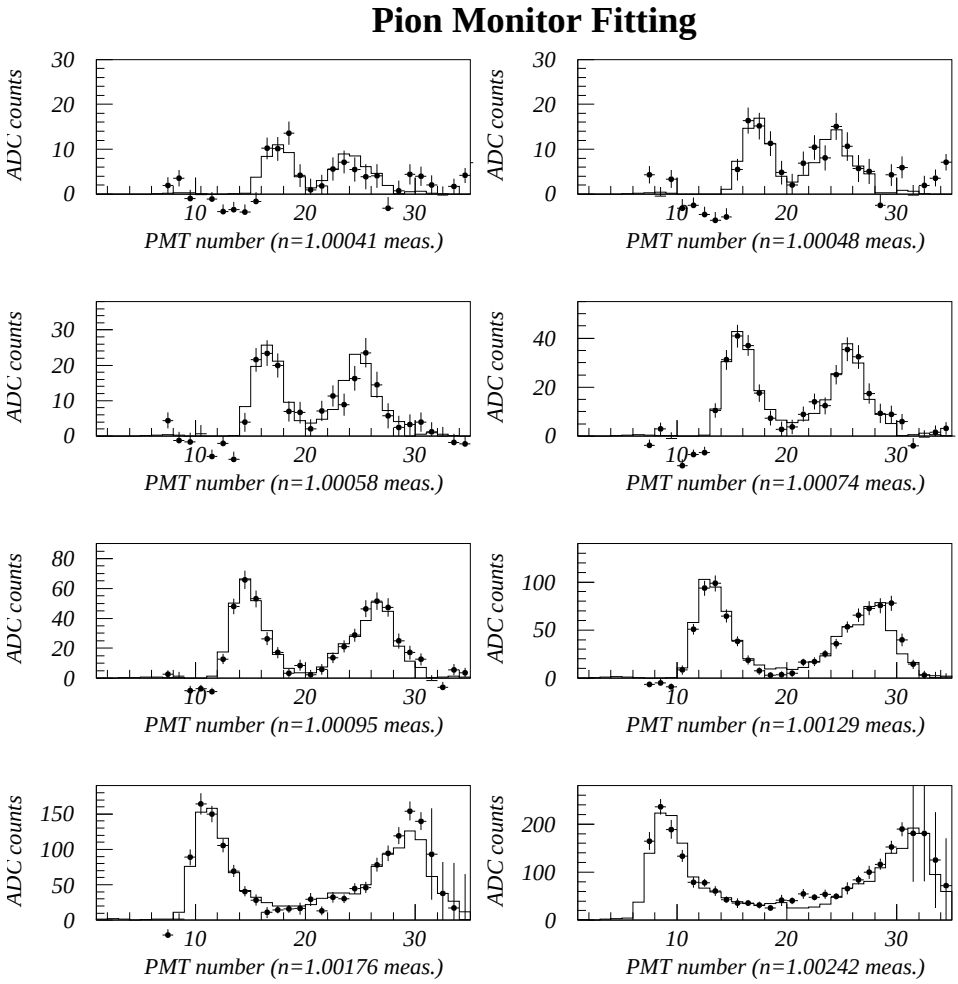

Figure 2.6: Raw Čerenkov light distributions for eight indices of refraction as recorded by the pion monitor. Because the PMTs are arranged in a linear strip, a Čerenkov ring is recorded as two peaks. Each distribution represents the superposition of light formed by pions of many momenta and directions.

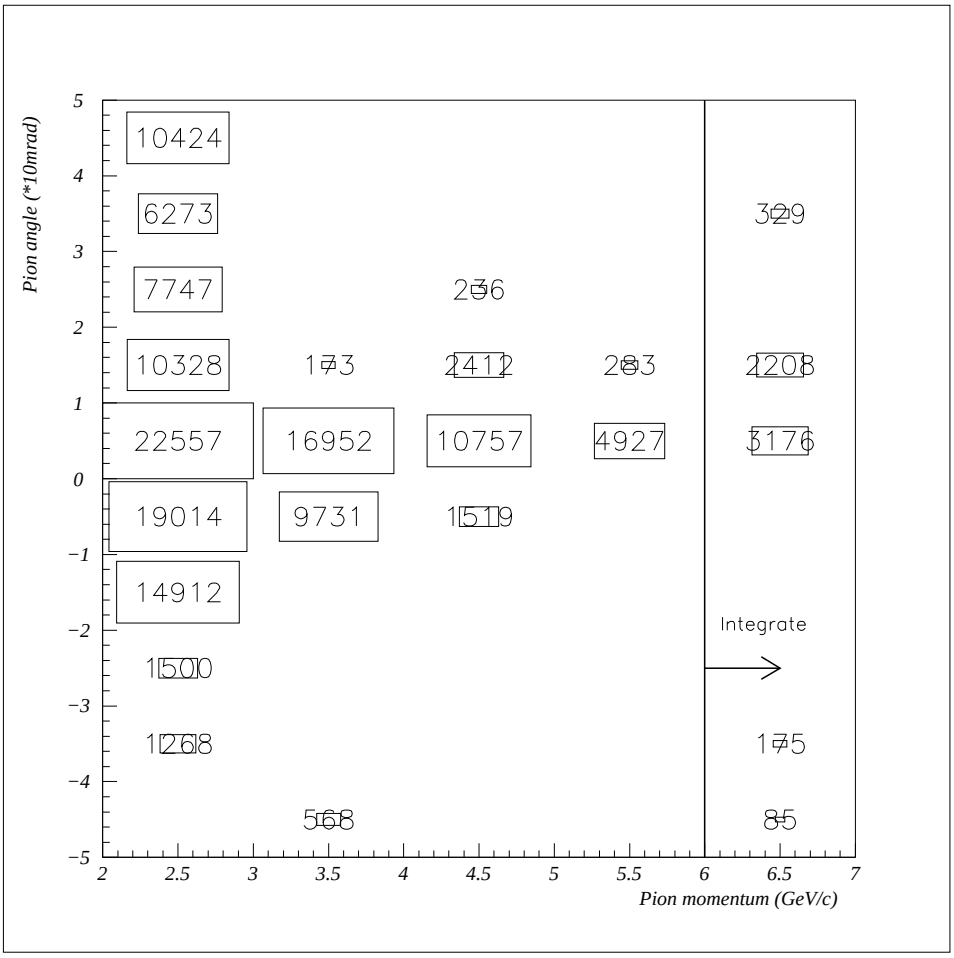

Figure 2.7: The secondary pion momentum distribution as measured by the pion monitor. The horizontal axis is pion momentum in units of GeV and the vertical axis is angle relative to the beam direction. Because the PMTs form only a vertical strip and not a full array only the vertical component of the angle is measured. Positive angles indicate downward moving particles, and negative numbers indicate upward moving particles. Since only the lower half of the beam is viewed by the pion monitor, these correspond to particles moving away from or toward the beam center. The information in this figure is determined by simultaneously fitting the data shown in Figure 2.6.

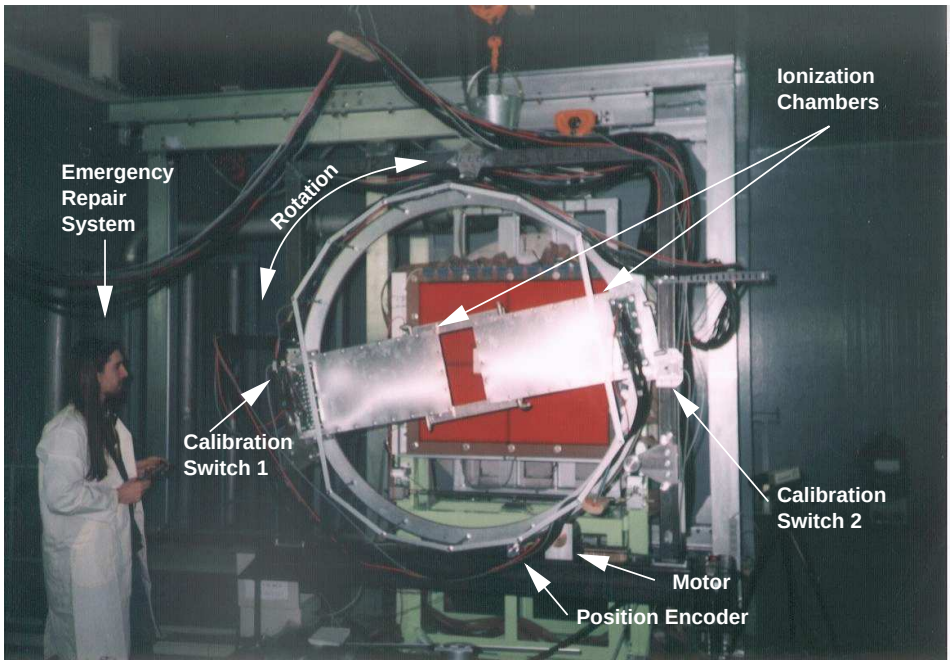

Figure 2.8: The Ionocopter

shortly after exposure to the proton beam. Instead of relying on the encoder signal, the position was inferred by counting steps made by the stepper motor and confirmed by the two position calibration switches. However, without a position encoder it is possible to lose track of the position of the device and dangerously stretch its cables or run off the end of its track. To remedy this, a home-made position encoder was created by attaching the internals of a standard PC joystick to a free floating pendulum attached to the device. The leads from the joystick were connected to 100 meters of twisted pair ethernet wiring and then to the data acquisition computer's game port, where it was read with a custom device driver. Although not quite as accurate as the optical position encoder, the emergency position encoder has proved to be quite radiation hard.

Two examples of measurements from this detector are shown in Figure 2.9. To collect the data for a complete measurement, the detector is positioned at a given angle and the PS dumps a single spill. The detector is then advanced a fraction of a degree and the process is repeated. Because the pads are much larger than the angle through which they move between spills, spill to spill variations in beam intensity are averaged out. When the entire circle has been mapped out in this way, the intensity at each individual point is plotted.

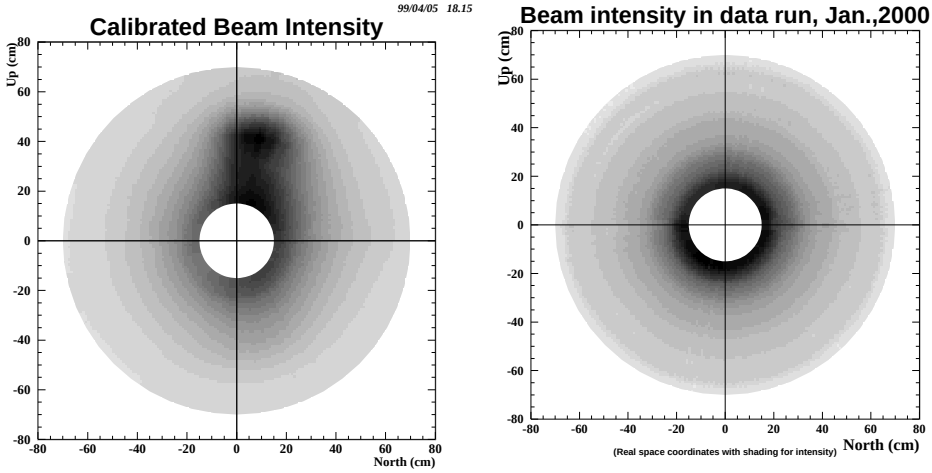

Figure 2.9: Ionocopter beam flux measurements before and after final beam tuning. The figure on the left shows an asymmetry observed during the commissioning of the K2K beam in March of 1999. Later measurements (right figure) show good axial symmetry.

Irregularities in the shape of the beam were observed during the tuning run in March of 1999, but since that time the beam has been cylindrically symmetric within detector resolution.

2.1.5 The Decay Pipe and Beam Stop

Pions produced by collisions of 12 GeV protons on aluminum tend to have a mean energy of about 3.5 GeV. The mean distance a particle will travel before decaying is $\beta\tau E/mc$, where c is the speed of light, β is the speed of the particle in units of c, τ the particle's mean life time at rest, E the particle's energy, and m is its mass. The charged pion has a mass of about 140 MeV/c^2 and a lifetime of 2.6×10^{-8} s, which tells us that we should expect pions to travel about 200 m on average. This is good news, because 200 meters is all the space available on the KEK site which will still allow room for the construction of the beam stop and near detectors. The pipe expands from two to three meters in width as you travel downstream and is filled with helium gas to reduce interaction of the pions with air molecules.

Although it may seem desirable to have a longer decay length, this is not necessarily the case. A longer pipe would allow more pions to decay and produce more neutrinos, but it would also increase contamination from electron

type neutrinos. Each pion decay also produces a muon. The muon can decay and produce a muon antineutrino and an electron type neutrino. The lifetime of the muon is about 100 times longer than that of the pion, so the number of muon decays will be relatively few, but to keep contamination at or below the 1% level, the pipe must be kept short.

Following the pipe is the beam stop. This starts with a $6 \times 6 \times 3.5$ meter steel block, followed by another 2 meters of steel containing a central 3 meter wide concrete plug centered on the beam axis. This combination can absorb nearly all hadronic particles (mostly primary protons and pions which did not decay). A significant portion of high energy muons will be able to penetrate the steel and concrete, so beyond this region are 30 meters of earth which will absorb most of the muons.

2.1.6 The Muon Monitor

Further information about the neutrino beam can be gleaned by measuring the muons produced in the pion decays. The arrangement of the muon monitor is shown in Figure 2.10.

The muon monitor consists of two components. The first is an set of ionization chambers with a total horizontal resolution of 36 channels and a vertical resolution of 32 channels. Each channel is 5 cm wide strip and the entire array covers a 2 m $\times$ 2 m area.

The second component consists of 17 solid silicon detectors arranged in an asterisk pattern. Because the ionization chambers record only the beam profile, there is some ambiguity about the actual two dimensional muon distribution. The silicon pads only sparsely cover the same area covered by the ionization chambers, but each pad allows the measurement of the muon flux at a single localized area. This is useful for reconstructing the two dimensional muon flux distribution.

The muon monitor is embedded just downstream of the steel portion of the beam stop. At this point, all of the protons will have been absorbed, but there is still a significant muon flux.

Unlike the pion monitor and ionocopter, the muon monitor is not destructive to the neutrino beam properties. This far down the beamline, the neutrinos have already been created and they won't be disturbed by the presence of the muon monitor. Therefore, the muon monitor can run continuously and record beam profiles in X and Y for every spill of the accelerator.

Obviously, for the K2K experiment to work, the neutrino beam must be carefully aimed at the far detector. The information from the muon monitor

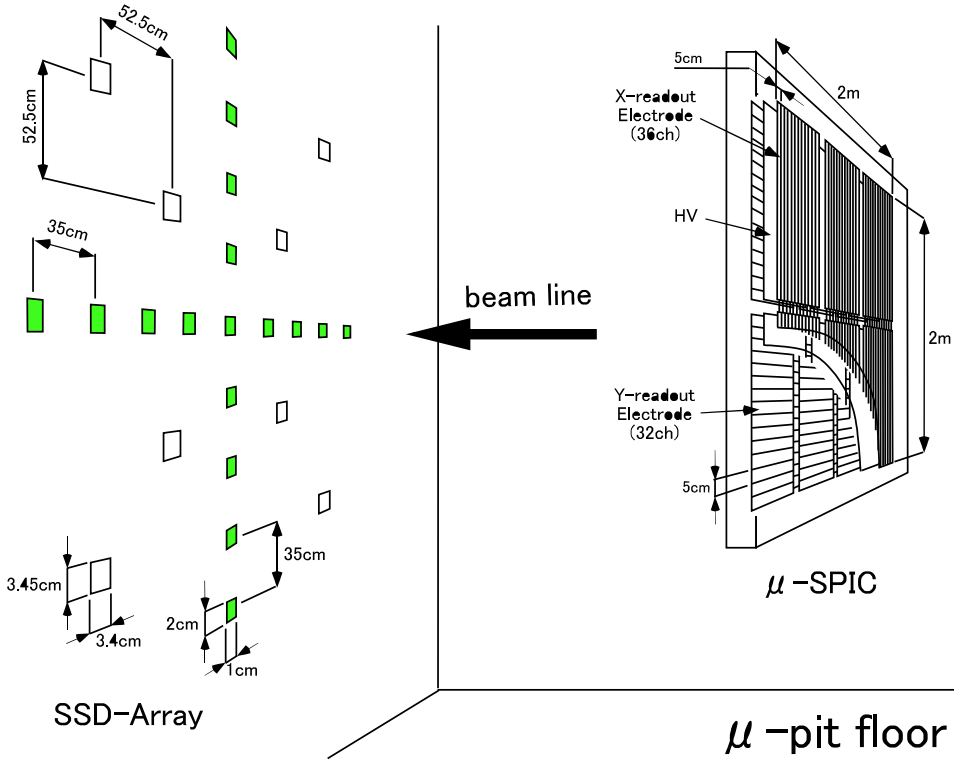

Figure 2.10: The muon monitor measure muon flux distributions downstream of the decay pipe. It consists of a 4 m^2 ionization chamber which measures the horizontal and vertical profiles of the muon distribution and 25 silicon detector pads which measure muon flux at localized points.

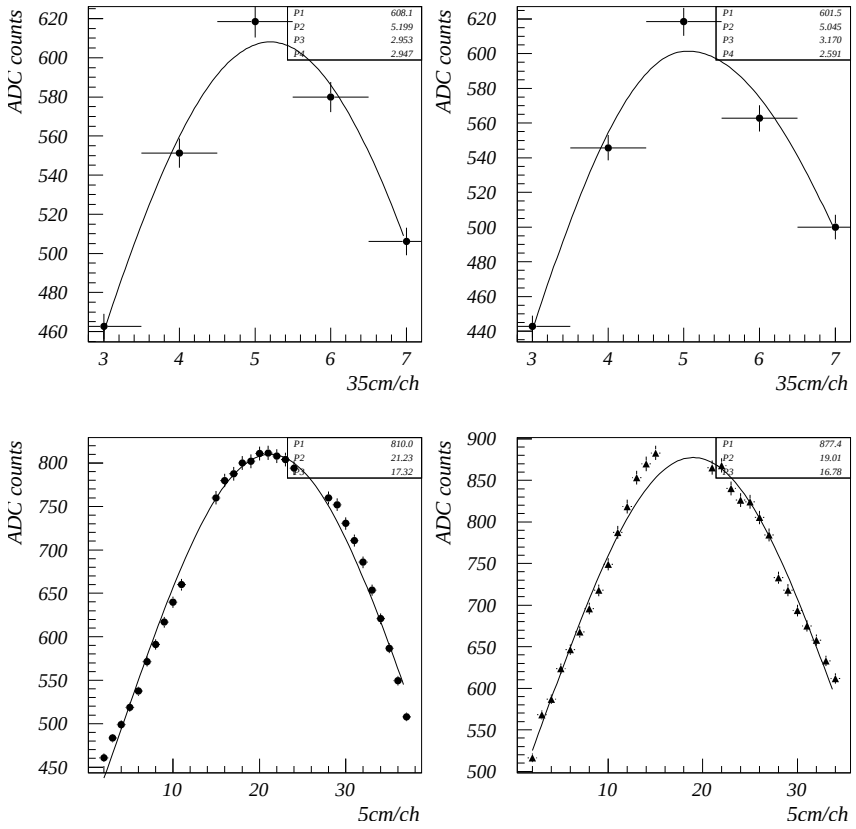

Figure 2.11: Sample muon monitor data for both the X (left figures) and Y (right figures) projections. Data from the silicon pad detectors (top figures) have been fit to asymmetric Gaussians, while data from the ionization chambers (bottom figures) have been fit to symmetric Gaussians. This technique can be used to track the beam center spill by spill.

provides us with an accurate ability to track properties of beam flux, centering, and spread. More about beam aiming will be discussed in section 2.5.

2.2 The Far Detector

At this point we'll skip forward in the path of a K2K neutrino and talk about the far detector first. The K2K experiment utilizes the Super Kamioka Nucleon Decay / Neutrino Detection Experiment, or Super–Kamiokande, as a far detector. This detector was designed and built prior to the K2K experiment for the purpose of studying naturally occurring neutrinos (and nucleon decay), however it is an ideal detector for our purposes.

2.2.1 Location

The Super–Kamiokande detector is located at 36°25′33″ N, 137°18′37″ E and 371.8 m above sea level. This is about 250 km west of Tokyo near the town of Kamioka in Gifu prefecture on Japan's Honshu island. Super–Kamiokande is in the Japanese Alps about 30 km south of the city of Toyama. The detector is embedded in Mt. Ikenoyama in an active zinc mine owned and operated by the Kamioka Mining and Smelting Company. The main laboratory building and computer center, the *kenkyutou*, is nearby in the small town of Mozumi.

2.2.2 Overview

Figure 2.12 shows an artist's conception of the Super–Kamiokande detector. The detector is located about 2 km along a straight horizontal tunnel as shown in the inset. Mt. Ikenoyama provides a minimum of 1000 m (2700 m water equivalent) of rock overburden over the Super–Kamiokande detector. A side tunnel houses the water filtration and another holds the control room where shift members monitor the detector. Both the detector cavity and the control room are kept at a positive air pressure by fresh air of low radon content being piped in from outside the mine. In addition, all exposed mine rock near the detector and control room is covered in a polyurethane like material, called mine guard, to reduce the amount of emitted radon as well as dust and debris.

More detail of the actual detector and cavity can be seen in Fig. 2.13[2].

[2]Thanks to K. Martens for this figure. Brett Viren believes there isn't really a giant fish at the bottom of the detector, but no one has been down there for some time.

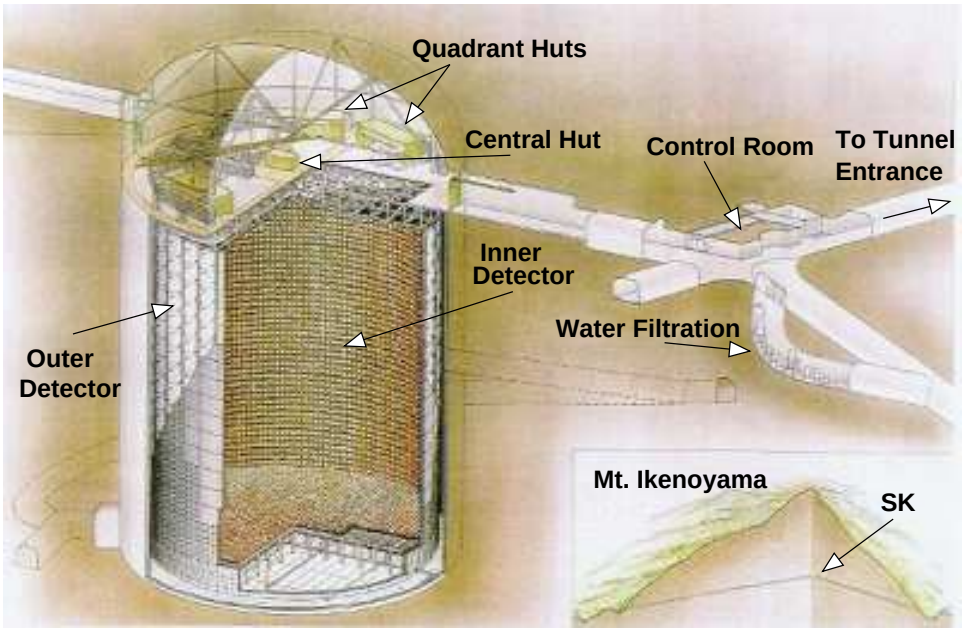

Figure 2.12: Super–Kamiokande location within Mt. Ikenoyama

This cross section shows the cavity and dome as well as the inner detector (ID), outer detector (OD) and the dead space between the two.

Like the pion monitor, the primary physical phenomenon behind the detection principle of the Super–Kamiokande detector is Čerenkov radiation. However Super–Kamiokande is not a ring imaging detector. The Čerenkov light travels directly to the the phototube covered walls as shown in Fig. 2.14. Unlike in a ring imaging detector, the ring projected onto the PMT array has a thickness proportional to the length of the track.

The number of photons emitted per unit length and per unit wavelength by the passage of a particle with charge $\pm e$ is,

$$\frac{d^2N}{dxd\lambda} = \frac{2\pi\alpha}{\lambda}\left(1 - \frac{1}{\beta^2 n^2(\lambda)}\right) = \frac{2\pi\alpha}{\lambda}\sin^2\theta_c, \tag{2.2}$$

where α is the fine structure constant.

For the water in Super–Kamiokande the index of refraction is $n \approx 1.35$, which is fairly constant over the range of wavelengths where the PMTs are sensitive. This results in a Čerenkov angle of $\theta_c = 42°$ and a photon production rate of about $dN/dx \approx 575$ per cm. In simulations the photon production rates and angles are more accurately predicted by integrating over the Čerenkov spectrum as well as the photo-detector's efficiency.

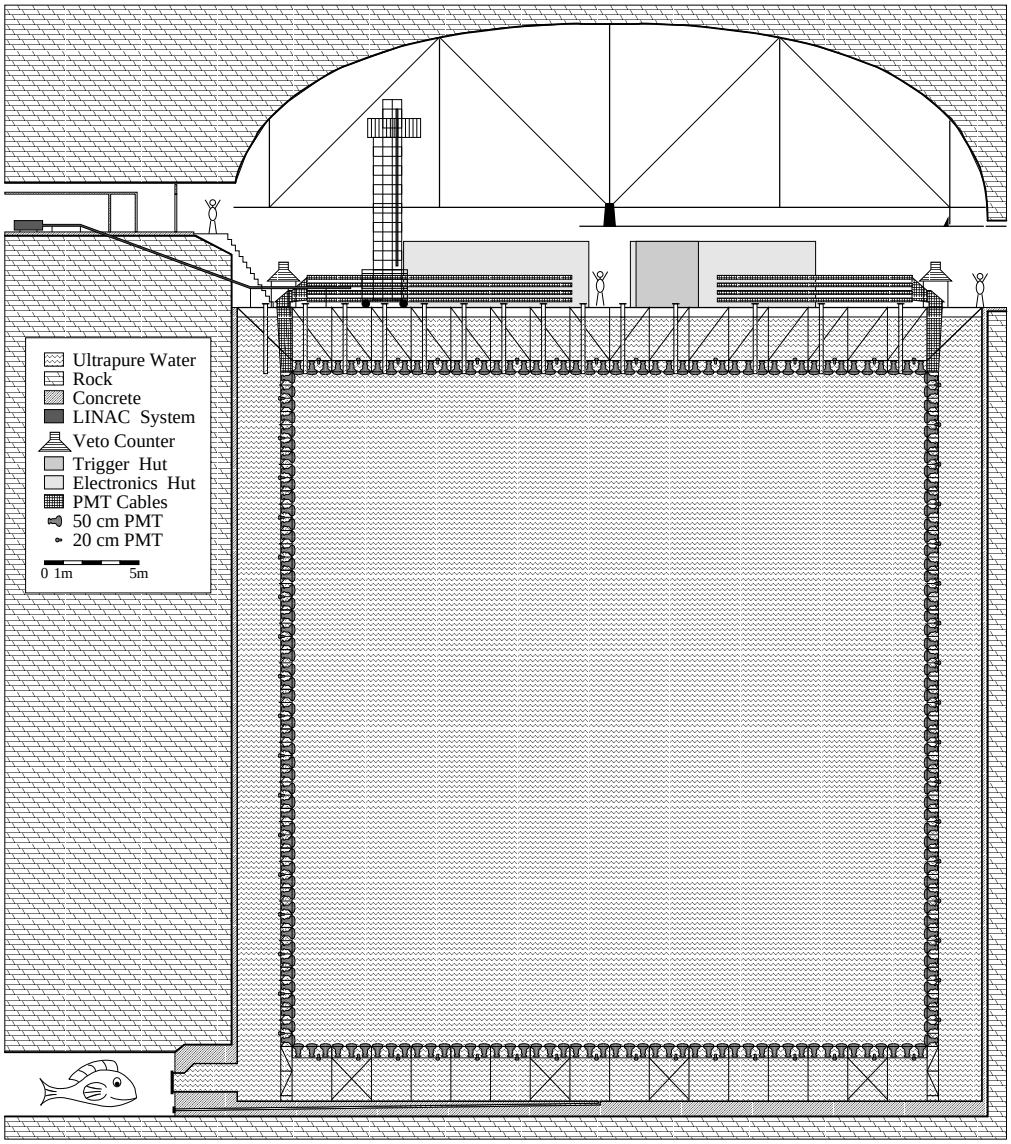

Figure 2.13: Cartoon of Super–Kamiokande detector and cavity.

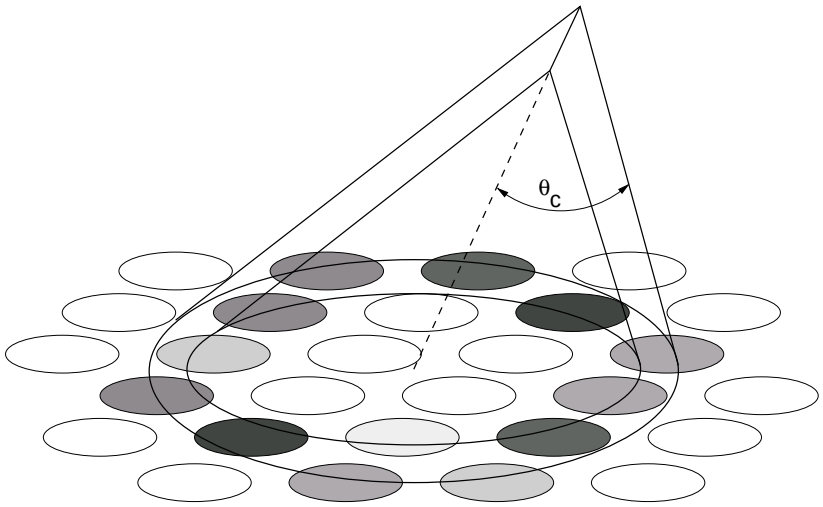

Figure 2.14: Cartoon of Čerenkov cone produced by relativistic charged particle in water and resulting ring on detector wall. The circles represent photodetectors and their shading represents the amount of light collected in each.

By placing light sensors in the path of a Čerenkov cone and measuring the number of photons and the time at which they struck the sensors it is possible to reconstruct the position, direction and type of the original charged particle. Also, by counting the total number of photons collected it is possible to estimate the amount of energy deposited by the particle.

2.2.3 Event Classes

Super–Kamiokande was designed to detect a variety of different types of events. These event classes are described below roughly in order from the lowest deposited energies of a few MeV to the highest of tens of GeV.

At the low energy end there are solar neutrino events and their primary backgrounds, radon and spallation. These events are all far below the energies of the neutrinos produced at KEK. In the low energy region there are also electrons from muon decays. Their energies range up to the theoretical limit of 52.8 MeV which can appear to be as much as 60 MeV due to energy resolution.

At higher energy deposition there are atmospheric neutrino induced events. Atmospheric neutrinos will primarily interact either by the charged current (CC) or neutral current (NC) weak interactions with the nuclei in the hydrogen and oxygen of the water. Interactions with the electrons of the water molecules are also possible but occur much more rarely. CC interactions produce a single

visible lepton and, if the momentum transfer is enough, one or more visible pions. Observable NC interactions produce one or more visible pions or a proton above Čerenkov threshold. In both cases, the pions may be absorbed or scattered on their way out of the nucleus. Neutral pions almost always decay to two photons which initiate electromagnetic showers. If the decay is very asymmetric, one of these showers may be too dim to discern. Most of the atmospheric neutrino induced events are fully contained (FC) within the inner volume of the detector. If the neutrino is of high enough energy, the outgoing lepton can exit the detector. These events are called partially contained (PC) and are almost always (98%) charged current ν_μ events. The K2K neutrinos will look and behave much like typical atmospheric neutrinos, but we can easily separate the two samples based on timing and direction.

The high end of observed energies has contributions from stopping and through going muons (see below for definitions). These muons can be from either cosmic ray muons or from muon neutrinos which interact in the rock around the detector. The cosmic ray muon flux decreases to zero as the originating direction of the muon goes below the horizon. Any upward going entering muons are considered to be from neutrino interactions in the rock. The longest through going muon tracks deposit about 10 GeV of energy. More energy will be deposited if a muon undergoes bremsstrahlung.

Finally, there may be nucleon decay events which will be limited in energy to be below about 1 GeV. Figure. 2.15 shows a cartoon of these and the other higher energy event classes.

2.2.4 Inner Detector

Description

The inner detector (ID) is the primary volume for detecting events in Super–Kamiokande. The ID is a cylindrical volume 33.8 m diameter and 36.2 m high and contains 32.5 metric ktons of water. 40% of the walls are covered by photocathode from the 11146 20" diameter PMTs (see below) the rest by a opaque black plastic used to help optically isolate the inner detector.

ID PMTs

A schematic of an inner detector PMT is shown in Fig. 2.16. A PMT works by turning a photon into a measurable electric pulse. It does this by first converting the photon to an electron (a so called *photo electron* or PE) through the photo-electric effect when the photon hits a deposited layer of

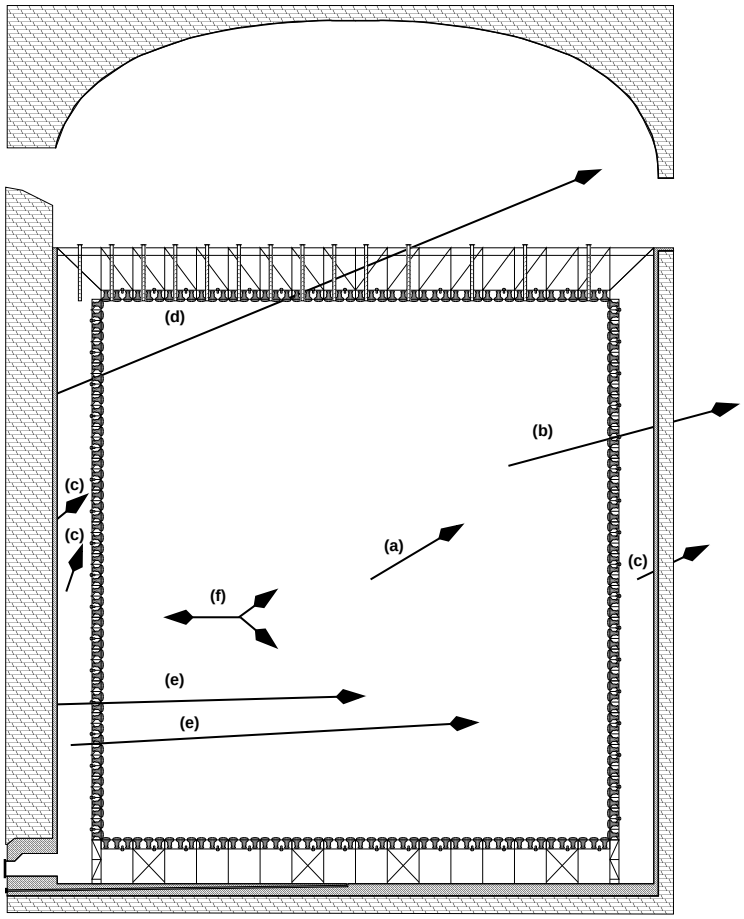

Figure 2.15: Classification of Super–Kamiokande event types: (a) contained single ring, (b) partially contained OD Crossing, (c) OD Contained, (d) through-going μ, (e) OD Crossing (entering), and (f) multi-ring contained.

bialkali (Sb-K-Cs) which is on the inner surface of the PMT glass. This layer is called the *photocathode*. The conversion is successful about 22% of the time (the average PMT quantum efficiency at a wavelength of $\lambda = 390$ nm). Because the photocathode is so near a large volume of water it is kept at ground potential. The photo electron is then accelerated to about 800 V and strikes the first dynode. Upon hitting the first dynode many electrons are liberated and accelerated through another 300 V to the second dynode. Each of these electrons continue showering as they hit 9 more subsequent dynodes each at about 100 V higher potential than the previous. After reaching the anode the shower has passed through about 2000 V and increased to about 10^7 electrons for each initial photo electron. For a single photo electron, the typical transit time from photo cathode to anode is about 100 ns with a spread of about 2.5 ns. This PMT is made by Hamamatsu, initially for Kamiokande with later design improvements [31] for Super–Kamiokande.

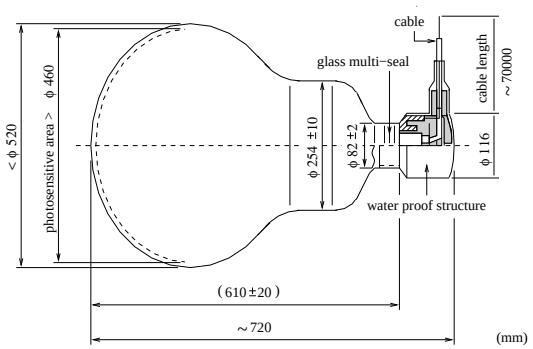

Figure 2.16: Inner Detector PMT

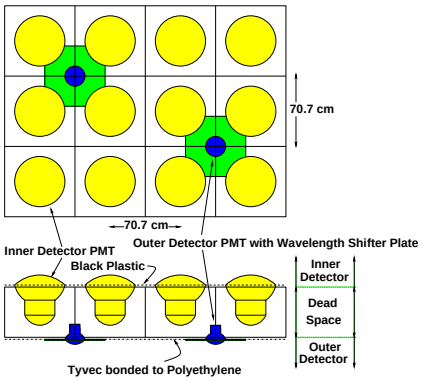

Figure 2.17: ID/OD PMT Placement.

The PMTs are mounted to the stainless steel support structure between the inner and outer detectors by stainless steel bands. Only the photo sensitive face protrudes through the sheet of opaque black plastic and into the volume of the inner detector. The relative location of the inner PMTs is shown in Fig. 2.17. The high voltage (HV) and signal is carried through a 70 m cable between the PMT and the HV supplies and Data Acquisition (DAQ) systems.

2.2.5 Outer Detector

Description

The outer detector (OD), (or anti-detector), was primarily designed as a veto against incoming cosmic ray muons. It is a cylindrical shell which varies in thickness between 2.0 m at the wall and 2.2 m at the top and bottom. It completely surrounds the inner detector with 14.7 metric ktons of water. Mounted on the inner wall and facing outward are 1885 PMTs with wavelength shifter plates (WSP). The outer wall is covered with a white reflective paper like material called Tyvec. The inner wall is covered by Tyvec bonded to opaque black low density polyethylene. The Tyvec increases Čerenkov light collection and the polyethylene increases the optical separation between the OD and the rest of the detector.

OD PMTs and WSPs

The photo multiplier tubes [32] and wavelength shifter plates used in Super–Kamiokande's OD are recycled from the IMB experiment [33]. These 8" diameter PMTs are also made by Hamamatsu however they have different characteristics than the ID PMTs. Besides being smaller, their transit time spread is 11 ns FWHM at one PE and 5 ns FWHM at 10 PE. These PMTs are also deployed more sparsely in the OD than those in the ID. For every 12 ID PMT, there are only 2 OD PMTs (see Fig. 2.17). This combined with the smaller size of each OD PMT gives only about 1% photocathode coverage. To improve the light collection, as in IMB, the PMTs have been fitted with wavelength shifting plates. These 60 cm square, 1.3 cm thick acrylic plates contain 50 mg/l flour bis-MSB and make contact with the edge of the PMTs at a close fitting hole in the center. The outer edges of the plates are lined with reflective aluminum coated mylar tape. When Čerenkov light hits the plate, it is absorbed and re-emitted at a wavelength more suited to detection by the PMT. The re-emitted photon is frequently trapped inside the plate by internal reflection. These photons will bounce around inside the plate until they hit the inner edge, which contacts the PMT surface. These plates increase the light detection efficiency by 60% over bare PMTs, but also increase the single PE transit time spread to 15 ns FWHM.

2.3 The Near Detector

The purpose of the near detector is to measure the neutrinos produced by the K2K beam directly. Although it is possible to make a reasonable estimate of the neutrino flux based solely on Monte Carlo simulations of the beam, it is more accurate to measure the neutrinos themselves. A large part of this is due to uncertainties in the neutrino cross sections. Even if the true flux were known precisely, the interaction rate measured is a function of the product of the flux and the cross section. By measuring the interaction rate at both ends, most of the effects of the cross section drop out in the comparison, and all we really need to know is the flux ratio.

It was neither practical nor desirable to build an identical replica of Super–Kamiokande to use as the front detector. For reasons which will be explained, a new full-size Super–Kamiokande would not perform very well as a near detector system. Instead, an aggregate detector consisting of four main parts was constructed. See Figure 2.18 for an overview of the K2K near detector system.

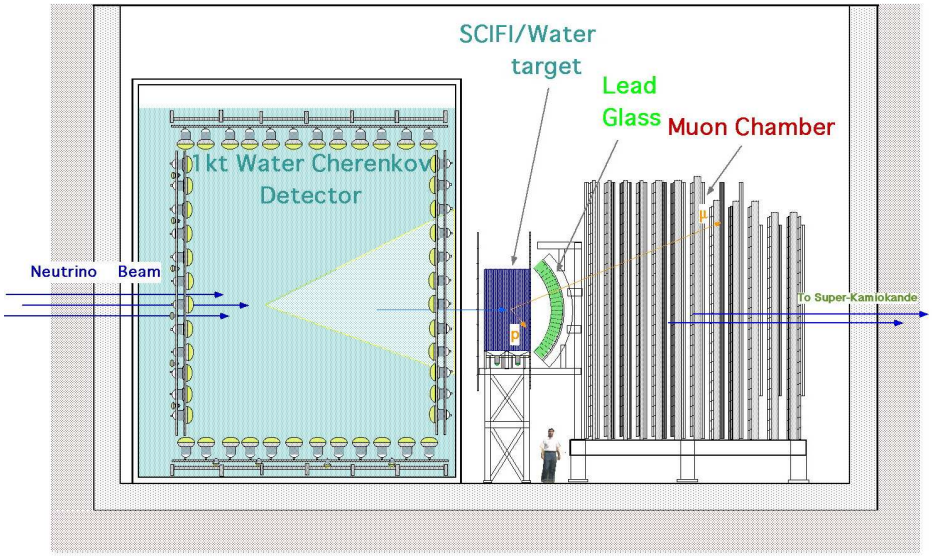

Figure 2.18: The K2K Near Detector

2.3.1 The Kiloton Detector

The kiloton detector was designed to be as much like the Super–Kamiokande detector as possible, only smaller, so it can closely match its detection characteristics and systematic uncertainties. It's a cylindrical water Čerenkov detector with 40% photocathode coverage provided by the same 20" PMT's used in Super–Kamiokande. The detector is divided into inner and outer regions by an optically opaque wall and the outer region is observed by 8" PMT's similar to those used at Super–Kamiokande.

The main difference between the kiloton detector an Super–Kamiokande is size. The kiloton detector is only 10 meters in height and 11 m in diameter, compared with 36 m $\times$ 34 m for Super–Kamiokande. Additionally, the wall which separates the inner and outer detectors is offset from the tank center, and outer detector coverage is not complete. Only the tank bottom and most upstream third of the wall contain OD PMT's. Since it is known that nearly all entering particles will be from neutrino interactions in the surrounding rock, it was only necessary to instrument these areas. Most entering cosmic rays or other non-beam related events will occur outside the spill gate and will never enter the K2K data stream. It is not necessary to have an outer detector to tag events which exit the detector downstream. In this case, the particle must pass very close to (or through) a phototube, and the amount of light deposited on this tube will be beyond the tube's ability to measure, resulting in a saturated tube. The presence of saturated tubes is a good indicator of a partially contained or exiting event.

The kiloton tank was previously used in KEK-PS E261, a predecessor to the Super–Kamiokande detector to study the accuracy of particle identification methods used in previous water Čerenkov detectors. The systematic errors of using a detector of this size were already partially understood.

There are two main deficiencies associated with the kiloton. First, because of its small size, it is not possible to measure the high energy tail of the neutrino spectrum. A muon loses about 200 MeV/m when traveling through water, so if a neutrino event produces a 2 GeV muon inside the tank, it will travel more than 10 m and inevitably exit the detector making a full reconstruction impossible.

The second problem is that the uncertainty associated with the fiducial volume is greatly increased. Because the fiducial volume uncertainty varies with the fiducial volume surface area, or r^2, but the event rate varies with the total volume, or r^3, the effect of fiducial volume uncertainties will be much larger in smaller detectors. The effect of the fiducial volume uncertainty is therefore much more significant in the kiloton than Super–Kamiokande.

For these two reasons, the additional detector components, collectively referred to as the "Fine Grained Detector", were built. By placing the fine grained detector downstream of the kiloton, we can record tracks of particles that exit the kiloton and measure the high energy tail of the neutrino spectrum. The fine precision of the scintillating fiber tracker (SFT) also allows us to reduce the effect of the fiducial volume uncertainty when studying neutrino events which occur within the SFT.

2.3.2 The Scintillating Fiber Tracker

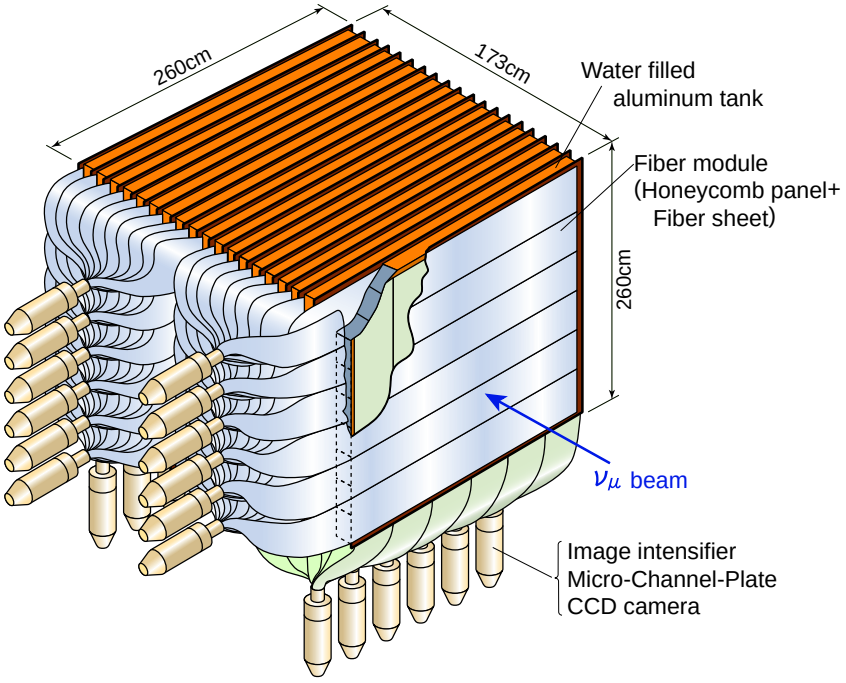

Figure 2.19: The Scintillating Fiber Tracker

The scintillating fiber tracker sits just downstream of the kiloton tank. It consists of alternating planes of scintillating fibers and water target layers. Each fiber layer consists of three components: horizontally oriented fibers, a rigid paper honeycomb panel, and vertically oriented fibers. Fibers are arranged in 40 cm wide sheets each containing two layers of 571 fibers. Six of these sheets are glued to each surface of the honeycomb panel to cover a 2.4×2.4 meter area. The fibers themselves are Kuraray SCSF-78M scintillating fibers. This fiber has a polystyrene core which gives a peak scintillation light

of about 450 nm (blue). The core is wrapped with two layers of cladding. The inner layer is polymethylmethacrylate and the outer is a fluorinated polymer. The purpose of these claddings is to increase the total internal reflection of the scintillation light.

Each water target layer consists of 15 aluminum boxes. Each box is 2.4 meters long, 16 cm high, and 6 cm thick. The SFT consists of 19 water target layers sandwiched by 20 fiber panels. Corresponding points on neighboring planes are separated by 9 cm.

Fiber data are read out by 24 Hamamatsu Image Intensifier Tubes (IITs) which are viewed by CCD cameras. The fibers extend approximately 1 meter beyond the 2.4 meter fiducial length. The excess lengths from 11420 fibers are bundled together and attached to one IIT. Fibers are read from one end only. The opposite end is covered with a reflective aluminum coating.

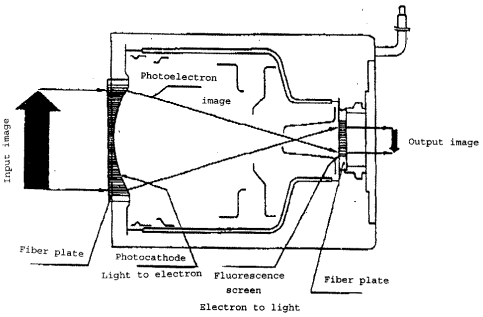

Figure 2.20: The first stage image intensifier (Hamamatsu V5502PX).

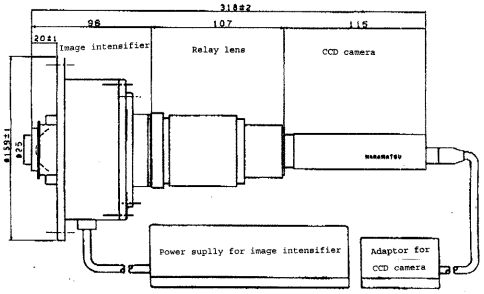

Figure 2.21: The second-stage system consisting of an image intensifier, a relay lens, and a CCD camera (Hamamatsu V1366GX/CCD).

An image intensifier tube works much like a photomultiplier tube, however each anode is covered by a phosphorus screen which converts the photoelectron back in to photons which can then be picked up by an ordinary camera. Because it is essential to preserve the geometric arrangement of the photoelectrons to preserve the image, there are no dynodes. The acceleration is done in one step. If further amplification is necessary, IIT's can be chained in multiple stages. In this case, we use a two stage IIT.

Each CCD camera has a viewable region of 768 $\times$ 495 pixels. Although the CCD region is rectangular, the IIT is circular by design, so the corners of the CCD are not used. Each fiber is approximately 4 pixels in diameter, but the spot made by the image intensifier is significantly larger than this. Because of the large size of the spot, and random variability of its location, it

is usually not possible to determine precisely which fiber was hit, resulting in a large degree of cross-talk. Figure 2.22 shows a portion of a typical image.

Each fiber sheet is separated from neighboring sheets by a plastic spacer so that cross-talk between fibers is usually limited to neighboring fibers on the same sheet, which minimizes its effect. However, the image frequently does extend into the regions occupied by other sheets. Software is used to decide which fibers are actually hit by analyzing the size, shape, and position of the spots. The fiber bundle design is shown in Figure 2.23. The fibers from a column of ten sheets are combined into a block, so that sheets in the same position on neighboring planes become neighbors in the bundle. This means that if the software fails to reject trans-plane cross-talk, a fake hit will appear on the following or previous plane. Occasionally this may lead to false tracks produced parallel to the real track.

Like the kiloton detector, the SFT contains a water target so that uncertainties in the neutrino cross sections will cancel out. Even though the SFT is much smaller than the kiloton, it's ≈ 1 mm position resolution means that it can define its fiducial volume much more accurately than the kiloton detector, which is important for determining the neutrino flux. However, the small size does mean that the SFT has no hope of measuring a neutrino spectrum by itself. It relies on further downstream components for momentum measurement of escaping particles.

2.3.3 The Veto Counters

To help tag particles entering from the upstream, the SFT is surrounded, upstream and down, by walls of scintillator paddles recycled from the VENUS experiment[35]. The counters cover a 4.2×4.2 m area and provide excellent timing resolution for particles exiting the SFT, which has only slightly better intrinsic timing resolution than a photographic emulsion. This is useful for the rejection of cosmic ray tracks.

Each scintillator is a slab of 466cm (length) $\times$ 10.8cm (height) $\times$ 4.2cm (thickness). Each wall contains forty scintillators running horizontally. The scintillators are coupled to Hamamatsu H1949-01s photomultiplier tubes via light guides. The upstream light guides connect two scintillator paddles to one PMT, while the downstream guides connect paddles individually. The scintillators have light guides on both ends, and the horizontal coordinates of a hit can be determined using the time difference of the hits on each end. The horizontal position can be reconstructed to within about 5 centimeters downstream, and slightly more upstream.

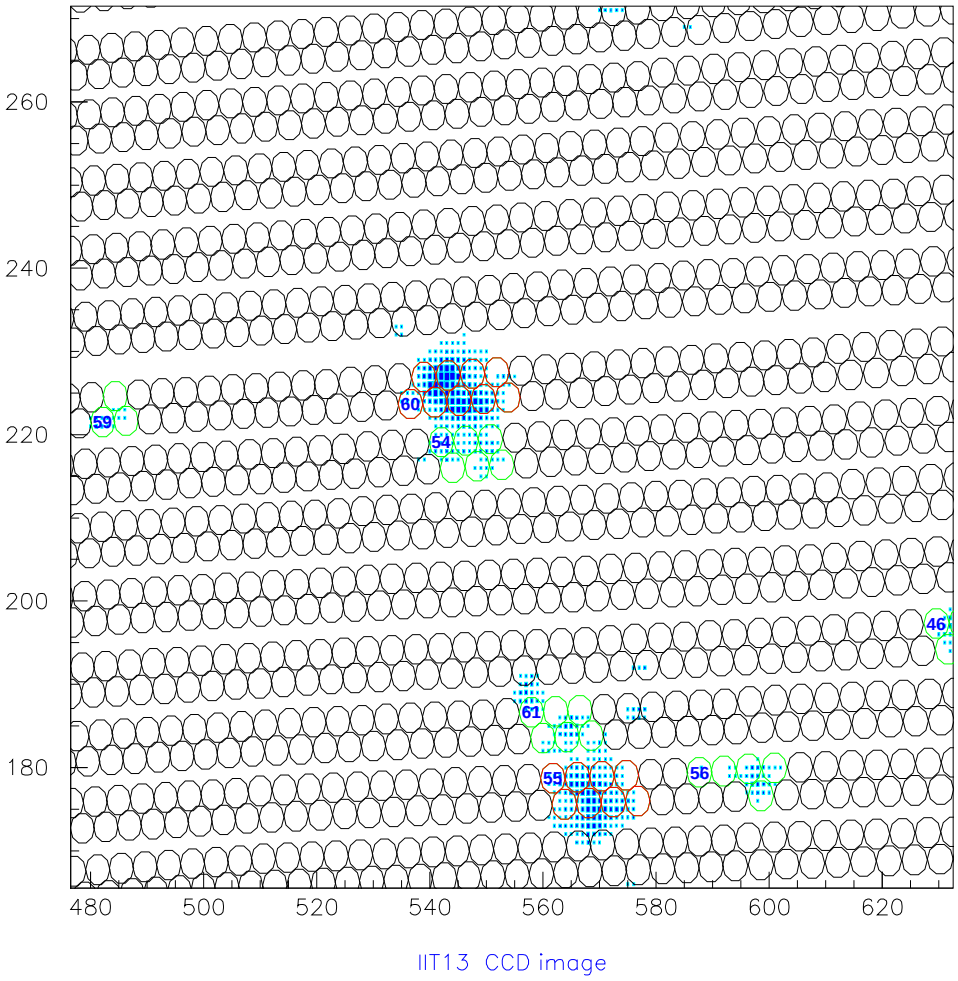

Figure 2.22: A portion of a typical IIT image. The axes are in units of pixels. Circles indicate known positions of fibers in the bundle. Fibers encircling enough hit pixels to be marked as hit are grouped into clusters of neighboring fibers and numbered. Fiber clusters colored in red are associated with a track while those in green are not. The image spot caused by a hit can be much larger than the fibers themselves. In this image, fiber clusters 55 and 60 cause cross-talk hits 61 and 54.

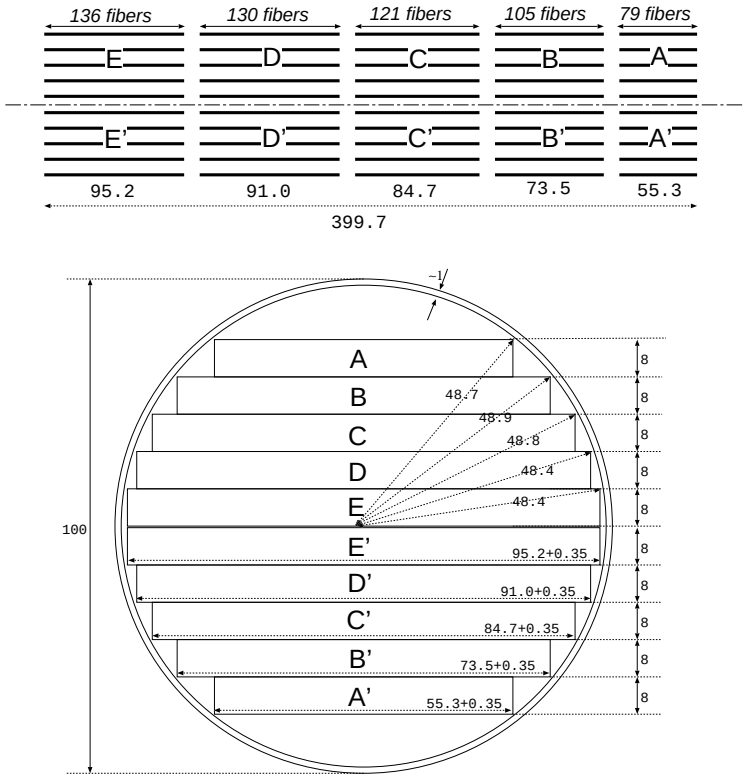

Figure 2.23: The SFT fiber bundle design. Each fiber sheet is broken into five uneven strips. Five strips from successive planes are glued into blocks. Ten of such blocks are then glued into a roughly circular bundle.

2.3.4 The Lead Glass Detector

The primary purpose of the lead glass detector is to measure electron showers escaping from the SFT. This is useful for studying the ν_e contamination of the beam as source of background for $\nu_\mu \rightarrow \nu_e$ neutrino oscillations.

Although oscillations in this mode in the parameter space to which K2K would be sensitive have now been ruled out by CHOOZ[26], at the time of K2K design and construction this was not known.

The lead glass blocks and PMTs for this detector were recycled from the TRISTAN[34] experiment. The array consists of 600 lead glass blocks arranged in a 5×2 array of 5×12 block modules. When hit by an electromagnetic shower, this detector can resolve the energy deposition to within $\sigma/E = 8\%/\sqrt{E}$.

The lead glass detector has fulfilled its usefulness and will be removed after the run ending in July of 2001.

2.3.5 The Muon Range Detector

The final near detector component is the Muon Range Detector (MRD), which is also known as the Muon Ranger. The MRD is a series of planes of drift chambers interleaved with iron plates. The drift chambers are recycled components of the VENUS experiment.

Unlike the kiloton detector, the MRD can successfully measure muon energies in excess of 3 GeV. High energy muons which escape the kiloton or SFT have a high probability of hitting the MRD's massive 8×8 meter wall. Muon energy can be determined simply by counting the number of layers through which the muon penetrates and correcting for the angle of incidence and thickness of each layer.

In addition to catching muons from upstream, the heavy iron plates are also an excellent target for neutrino interactions. Although using the MRD to predict the event rate at Super–Kamiokande suffers from the systematic uncertainty due to the difference in cross section of iron and water, this information is useful as a cross check. The large number of events also provide additional information about the shape of the neutrino beam more directly than the information from the muon monitor.

Because it is desirable to be able to measure both low and high energy events with good sensitivity, the iron layers are not all the same thickness. The first four slabs are 10 cm thick while the remaining eight plates are 20 cm thick. This gives us a total iron length of two meters with a maximum measurable energy deposition of about 2.7 GeV for tracks parallel to the beam

axis and more for tracks at wider angles.

2.4 The GPS Timing System

It's critical to have accurate time synchronization between KEK and Super–Kamiokande. This is important because K2K uses the arrival time of neutrinos to distinguish beam related neutrino events from ordinary atmospheric neutrino events. The timing signals from the Global Positioning System allow us to synchronize clocks at the two ends of the beamline with a resolution of 100 ns. This is narrower than our spill gate so additional accuracy would not help us tag events related to our beam. 10 ns resolution would allow studies of the bunch structure at Super–Kamiokande, but this level of analysis is not necessary.

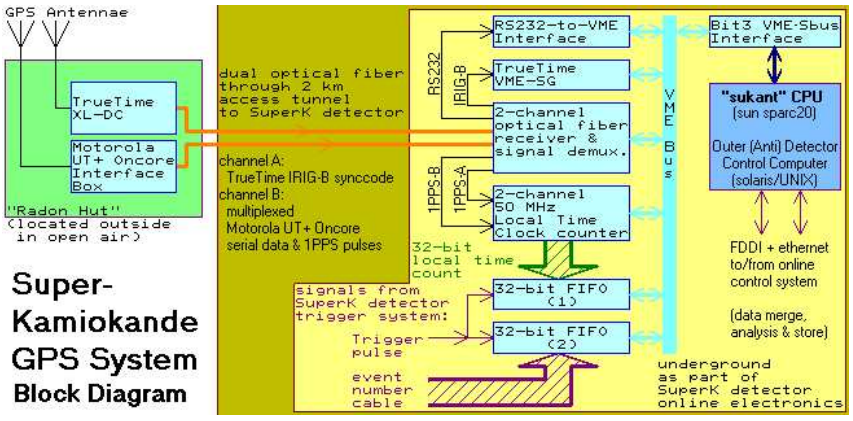

Figure 2.24: Block diagram of Super–Kamiokande's GPS. TrueTime and Bit3 are brand names.

Figure 2.24 shows a schematic diagram of the GPS system at the Super–Kamiokande site. This is a redundant system employing two different GPS receivers from different manufacturers. Due to the extremely poor radio reception typically found under mountains, the GPS receivers are located outside the mine, about two km from the actual detector. The GPS time signal is sent along an optical fiber to the data acquisition systems. After arriving at the detector, the signal must be offset by the delay associated with the fiber.

A similar system is in place at KEK. This system is a little simpler, since it's not necessary to place the antennas so far from the DAQ.

In each system, the GPS time is not accessed directly. When Super–Kamiokande triggers or when the KEK PS spills, a signal is sent and the time is read

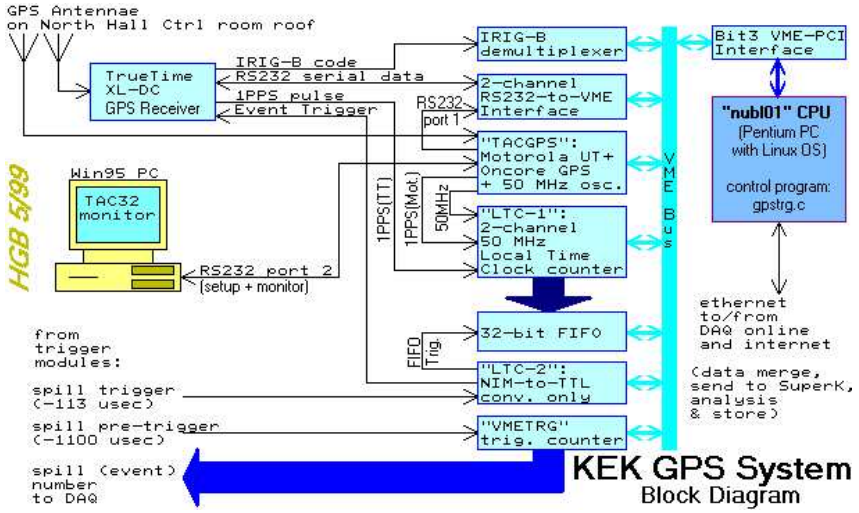

Figure 2.25: Block Diagram of KEK's GPS

from a 50MHz local time clock (LTC). The local time clock is continuously calibrated by the a 1Hz pulse from the GPS receivers.

2.5 Neutrino Beam Aiming and Stability

Many people are impressed with the feat of hitting a target, even a 40 meter wide target, from a distance of 250 km, but this isn't as difficult as it sounds. Thinking of hitting Super–Kamiokande with the K2K beam as hitting a target with a rifle is not an appropriate analogy. It's closer to compare it with hitting a target with a flashlight beam. As the target gets further away, the flashlight spot gets bigger (but dimmer). The accuracy with which the beam must be aimed doesn't depend on the distance to the target at all. To determine the level of accuracy required for beam aiming, all we need to know is the "spot size" of the beam at 250 kilometers.

Figure 2.26 shows the expected neutrino beam flux at 0, 1, 2, and 3 km (0, 4, 8, and 12 milliradians) off the beam center 250 km from KEK. Even at these large displacements, there's very little change in the flux. Most of the differences occur in the higher energy tail, which is more finely focused due to the larger Lorentz boost. Missing Super–Kamiokande by as much as a kilometer (or 4 mrad) will have no measurable effect on our data given the expected statistics.

In addition to being used for timing, the global positioning system was

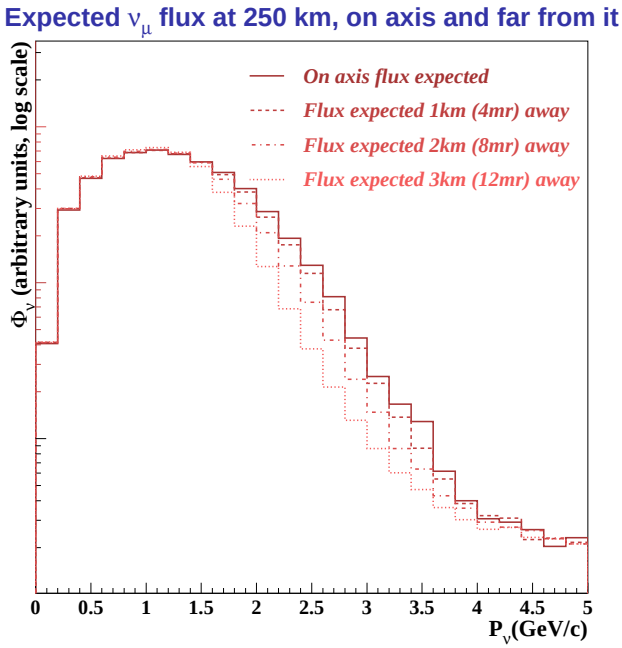

Figure 2.26: Expected neutrino flux on and very far off beam axis. The log scale is used to exaggerate the small differences in the expected neutrino flux found at angles much wider than the K2K pointing accuracy.

used to survey the K2K beamline prior to construction. The survey accuracy was ~ 0.01 mrad, and the beamline was constructed with a pointing accuracy of ~ 0.1 mrad. The primary source of inaccuracy in beam direction remains small fluctuations in the electromagnetic fields near the target. Figure 2.27 shows the centroid of neutrino event positions measured in the MRD. The centroid is within 1.0 mrad of the direction to Super–Kamiokande for almost the entire run of the experiment. Uncertainties in the event rate at Super–Kamiokande are almost negligible.

Figure 2.27 also shows the neutrino event rate normalized by the number of protons on target. This is very flat and shows a consistent beam performance over time. Since the predicted number of events in Super–Kamiokande will be normalized by the event rate in the front detector, correlations with the number of protons on target are not very important, but such a good correlation helps build confidence that there are no major unknown systematic effects.

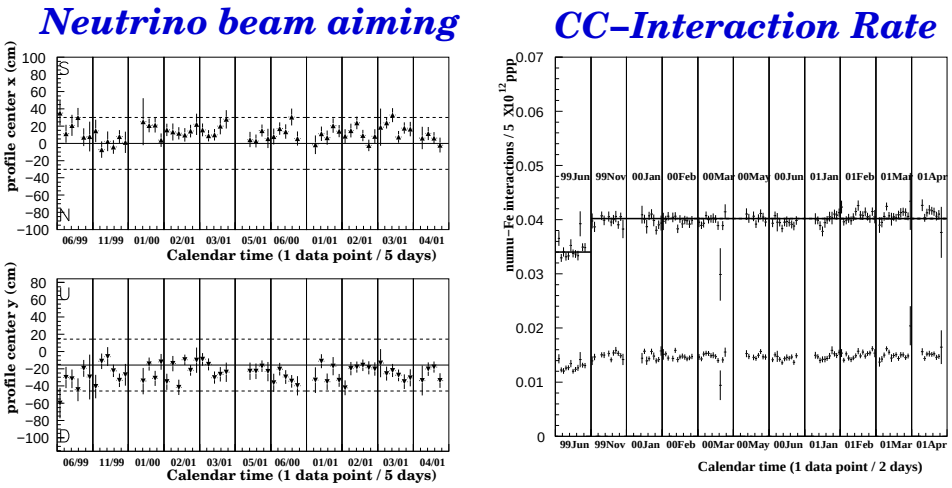

Figure 2.27: Beam stability as measured by the muon range detector. The left figures show the centroid of reconstructed vertices for each five day period. Dashed lines indicate ±1 mrad. The figure on the right shows the event rate averaged over each two day period and normalized by the number of protons on target. The upper data series is the event rate in the first 9 iron layers, and the lower data series includes only the first three layers of iron. The event rate in June of 1999 is expected to be lower than later runs since the horn magnets were operating at only 80% normal current during that time.

2.6 Computing Hardware & Software

To match K2K's motley detector systems, the hardware and software used for data acquisition and event reconstruction is a heterogeneous mishmash of computers of various architectures and operating systems.

Machines provided by the Institute for Cosmic Ray Research are predominantly Sun/Fujitsu systems based on UltraSparc processors running Solaris. These machines are used for the two water Čerenkov detectors. Some additional water Čerenkov offline computing is also done on the Compaq Alpha machines running True64 Unix located at ICRR's Kashiwa campus.

KEK provides a large parallel processing system based on Hitachi processors running HI-UX which is currently being phased out in favor of an IBM machine running AIX. This machine is used for data storage and management.

Data acquisition for the fine grained detector is handled by a Hewlett Packard machine running HP-RT, a real-time version of HP-UX. Most other machines used for online control and offline processing of fine grained related data are x86 compatible systems running some form of GNU/Linux, be it from

Red Hat, Debian, Slackware or Turbo Linux.

There are also two PC's running Microsoft Windows which serve as a monitors for the kiloton water purification system and backup GPS timing system. Neither machine is critical for the operation of the experiment.

Chapter 3

Near Detector Data Analysis and Results

The purpose of the near detector is to provide us with the information necessary to improve our prediction for the neutrino flux as a function of energy at Super–Kamiokande. In this chapter we will consider the measurement of the neutrino spectrum and event rate in the near detector.

Each of the three major near detector components, the kiloton detector, the scintillating fiber tracker, and the muon ranger, is capable of independently measuring the neutrino interaction spectrum and event rate, although each has its limitations. The muon ranger's primary deficiency is that it is not a water target detector, so it is not possible to completely cancel the effects of the neutrino interaction cross section when compared with Super–Kamiokande. The kiloton detector is the most like Super–Kamiokande, but its limited size makes the measurement of very high energy particles impossible. In addition, uncertainties in the kiloton fiducial volume limit the accuracy with which the far event rate can be predicted. By contrast, the SFT's fine tracking precision allows for a greater certainty of the fiducial volume, but its extremely small size coupled with its inability to self-trigger means that it also cannot form a complete spectrum measurement by itself. Despite all of these individual deficiencies, we can combine information from all of these detectors to derive a sufficiently complete and accurate spectral measurement.

Measuring the neutrino spectrum is difficult because we cannot observe the neutrino itself, only the results of some interaction it has. If the energy of all of the interaction products can themselves be observed, then the energy of the neutrino could be calculated using conservation of energy, however, this almost never the case in our detectors. If the neutrino scatters off of a nucleon, then this nucleon is usually below Čerenkov threshold in the kiloton or not of high enough energy to cross enough planes to form a track in the SFT or MRD. In general, we can't ever count on observing all reaction products.

But if this reaction is quasi-elastic scattering, where a neutrino exchanges

a W with a nucleon and there are no further reaction products, then the energy of the neutrino can be calculated as:

$$E_\nu = \frac{ME_\mu - m^2/2}{M - E_\mu + p_\mu \cos(\theta)} \tag{3.1}$$

Here, M is the mass of a nucleon, and m the mass of a muon, and θ is the scattering angle of the muon relative to the initial neutrino direction, which can be assumed to be parallel to the beam axis. This approach works by reducing the problem to a simple two body scattering problem and employing conservation of momentum to calculate the energy of the neutrino without using the kinetic information of the unobserved nucleon. However, it completely breaks down if there are multiple particles involved, such as additional pions. Of course, Equation 3.1 is only approximately correct since it assumes that the proton is at rest in the lab frame. The proton's Fermi momentum will blur this relation by about 100 MeV.

To measure the neutrino spectrum in each of the near detector components, we will try to select as pure a sample as possible of charged current quasi elastic scattering events, then employ Equation 3.1 and subtract the remaining non-quasielastic background using Monte Carlo estimates.

In practice the final derived neutrino spectra from the near detector are not as important as they would initially seem. We'll see in Chapter 4 that significant changes in the spectrum are expected as the beam travels to Super–Kamiokande. The beam Monte Carlo is still needed to determine the shape of the spectrum at the far detector.

The near detector measurements are most useful as tuning input to the beam Monte Carlo, both to improve the accuracy of the prediction as well as to determine systematic errors. Systematic errors can be calculated by varying beam Monte Carlo inputs as much as possible while still retaining agreement with near detector measurements. For these uses, it is possible to use the more raw forms of the near detector measurements, such as neutrino interaction rate, vertex distributions, and ejected muon angular distributions, rather than fully reconstructing a near detector neutrino spectrum.

Much of this Monte Carlo tuning and systematic error study still remains to be done, and work is continuing in this area. The full near detector neutrino spectrum reconstruction is presented here primarily for instructive purposes.

3.1 The Kiloton Detector Data Analysis and Results

3.1.1 Event Selection and Reconstruction

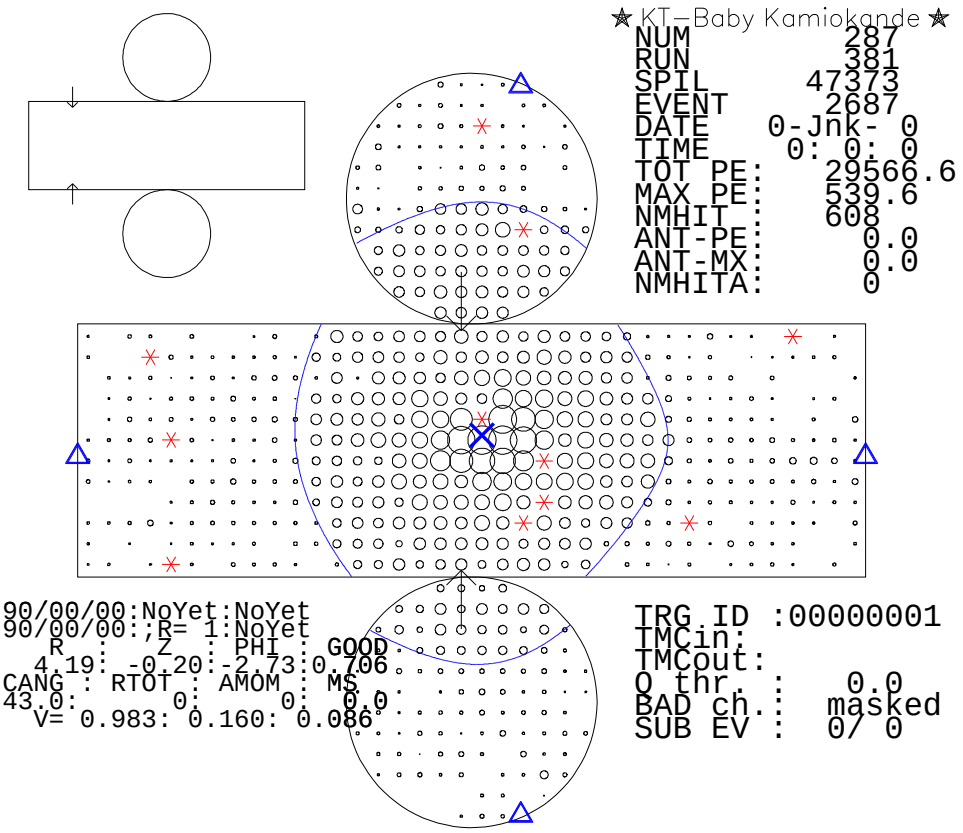

Figure 3.1: An event display showing a typical neutrino event in the one kiloton detector. The filled ring with saturated tubes in the center is indicative of an exiting muon.

Figure 3.1 shows an event display for a typical neutrino event in the one kiloton detector. Events in the kiloton look very much like events in Super–Kamiokande (Figure 5.3) but with far fewer phototubes.

Theoretically, the kiloton data reduction should be as close to Super–Kamiokande's as possible, but it's not practical to use an identical set of selection criteria. This section will describe differences between the kiloton and Super–

Kamiokande event selection procedures. A full discussion of the Super–Kamiokande event selection is in Chapter 5.

Not only is the kiloton detector not under a mountain, meaning that the cosmic ray muon flux is much higher, but the proximity to the neutrino source means that the neutrino flux is also much higher. The neutrino and background event rates are so high that it is necessary to take care to handle the case of multiple events occurring in the same spill.

To deal with this, the kiloton detector is equipped with a transient digitizer. For the duration of a spill, this device records the total charge being reported by all PMTs at any given moment in time. Any event occurring inside the kiloton should produce a peak in the transient digitizer graph. Because the event fitters are not well understood in the case of multiple simultaneous interactions, we require the number of peaks to be one for events to be included into the sample used to predict the flux and spectrum at Super–Kamiokande.

Another problem with proximity of the kiloton to the neutrino beamline is that the flux is not uniform as a function of position in the detector. The solid angle subtended by the kiloton is much larger than that of Super–Kamiokande. The neutrino flux is most intense near the center and falls off radially outward. For this reason, the shape of the fiducial volume used at Super–Kamiokande, vertical coaxial cylinders, is not appropriate for all measurements, since this geometry is not symmetric with respect to the beam. The kiloton fiducial volume is defined as a horizontal cylinder aligned along the beam axis.

Naively, one would expect that using only those neutrino events which appear to occur in the very center of the kiloton detector would more closely match the neutrino events in Super–Kamiokande, but this is not the case. Figure 3.2 illustrates how neutrinos that interact in the very center of the kiloton detector may not have been pointed at Super–Kamiokande. What determines whether a particular neutrino will hit Super–Kamiokande is its direction, not its position. Although these are correlated, this correlation is not complete. Because neutrinos are produced by pion decays, the neutrino direction will be bent away from the proton beam axis by some angle. The path of some neutrinos which travel through the center of the kiloton may never intersect Super–Kamiokande, while other neutrinos which are offset from the beam axis may be pointed directly at Super–Kamiokande. The only solution to this problem is to measure neutrinos over an extended area inside the kiloton detector and compare this to Monte Carlo predictions.

Other than the differing fiducial volume and need for the transient digitizer, event selection and reconstruction is essentially the same as it is for Super–Kamiokande. The complexity of using GPS for the timing signal is not needed, since the beam timing signal can be wired directly into the data acquisition

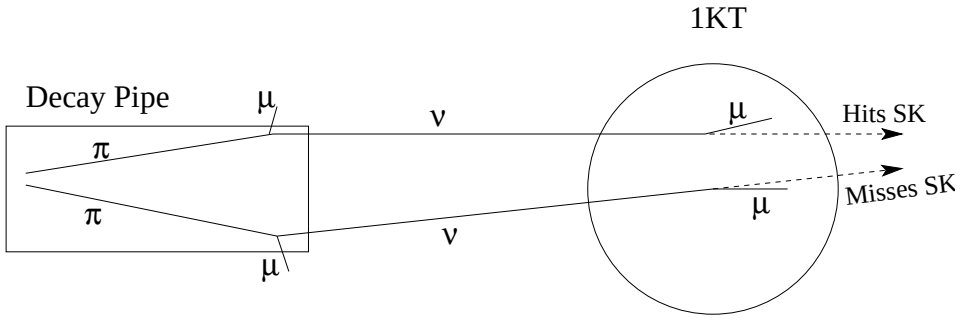

Figure 3.2: Schematic diagram showing complications in extrapolating the flux to Super–Kamiokande. (Not to scale.) Neutrinos which interact on the periphery of the kiloton detector may have been pointed directly at Super–Kamiokande while others in the very heart of the detector may be headed elsewhere.

system due to the proximity of the detector to the accelerator.

3.1.2 The Kiloton Neutrino Spectrum

To reconstruct the neutrino energy spectrum using the kiloton detector data, we select single ring muon-like events which are fully contained.

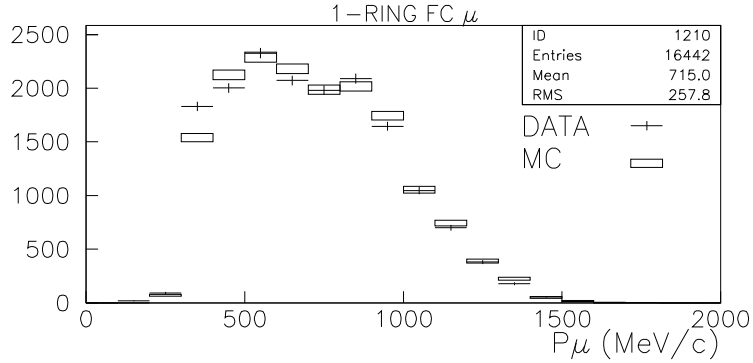

Figure 3.3: 1KT Fully Contained Muon Momentum Spectrum

Figures 3.3 and 3.4 show the observed momentum spectrum and angular distributions for fully contained muons in the kiloton detector for both data and Monte Carlo. Using these values we can calculate the neutrino energy for each event by assuming quasi-elasticity and applying Equation 3.1. The resulting energy spectrum is shown in Figure 3.5.

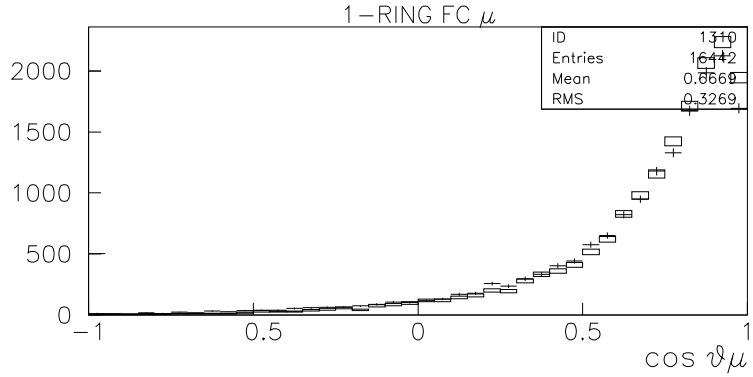

Figure 3.4: 1KT Fully Contained Muon Angular Distribution

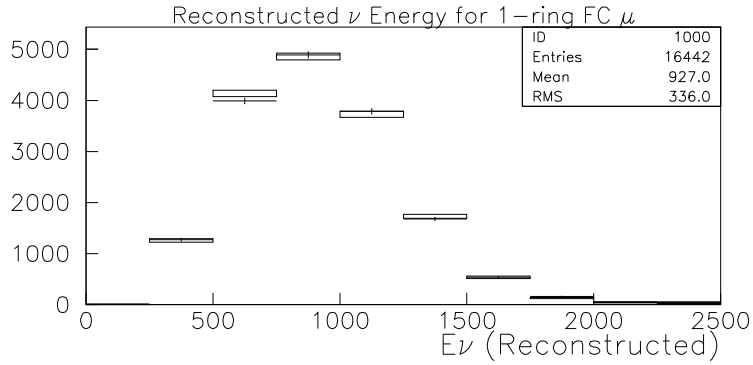

Figure 3.5: 1KT Fully Contained Reconstructed Neutrino Spectrum

This reconstructed spectrum is systematically softer than the true MC neutrino spectrum because it contains non-quasi-elastic events, which will always reconstruct below their true energy using this method. To correct for this, we'll use the Monte Carlo. The bottom part of Figure 3.6 shows the Monte Carlo reconstructed neutrino spectrum with the shaded region representing the non-QE component. If we believe the shape of the Monte Carlo prediction for these inelastic events, then we can normalize the total number of MC events to the total number of data events and calculate the non-QE component of the data spectrum. This is shown in the top part of Figure 3.6. We can then subtract this prediction to get the QE spectrum shown in Figure 3.7.

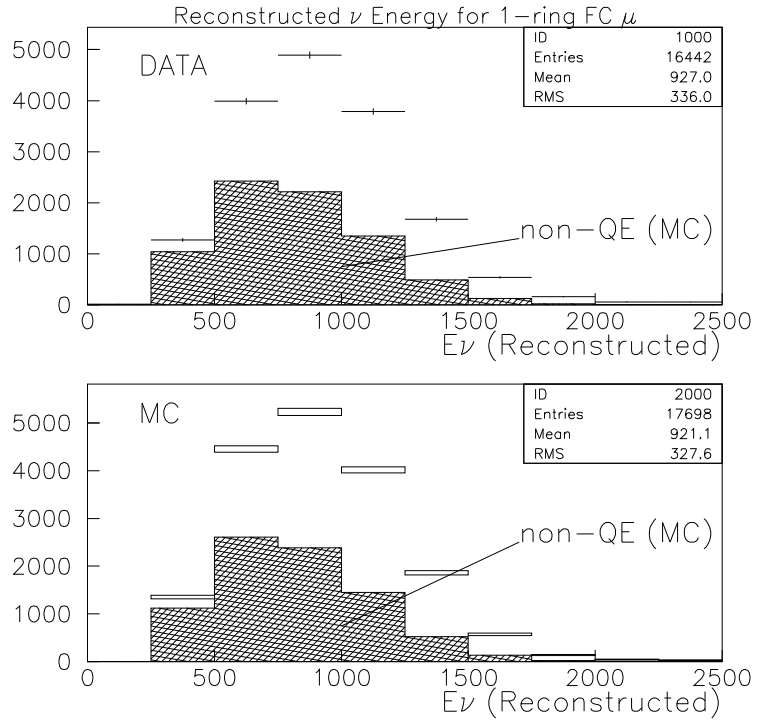

Figure 3.6: 1KT Fully Contained Non-QuasiElastic Background

This spectrum still doesn't account for the effects of detector resolution. Figure 3.8 shows the difference between MC true and reconstructed neutrino energies for quasi-elastic events. The lower part of this figure shows the migration map between energy bins. This information can be taken to form a matrix which can be inverted and applied to the data to find a neutrino spectrum which would look like our measured spectrum after smearing by detector resolution. Such a spectrum is shown in Figure 3.9.

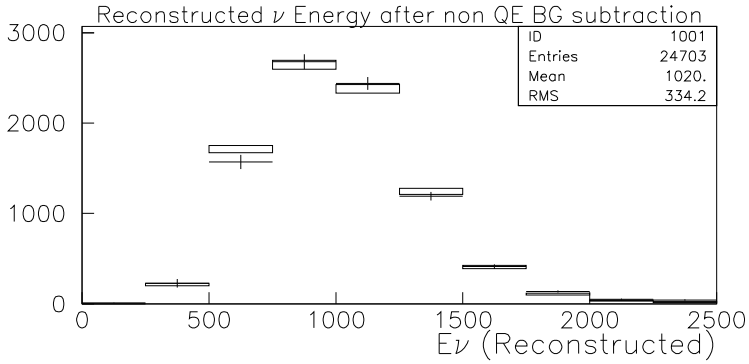

Figure 3.7: 1KT Fully Contained Background Subtracted CCQE Neutrino Spectrum

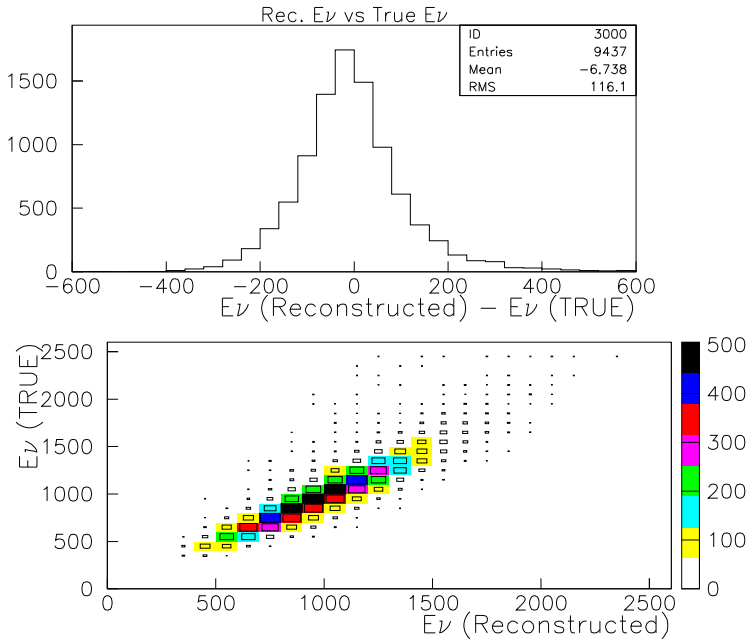

Figure 3.8: 1KT Fully Contained Background Subtracted Energy Resolution

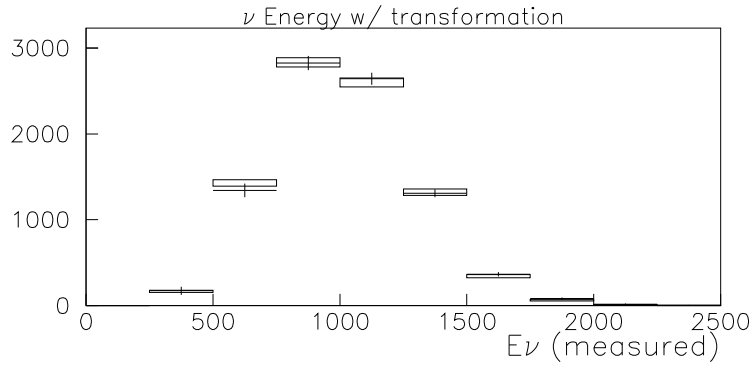

Figure 3.9: 1KT Fully Contained Background Subtracted Resolution Corrected Neutrino Energy Spectrum

Finally it is necessary to correct for acceptance. Using the 1KT detector alone requires that an event be fully contained in order to be measured, but high energy events are more likely to exit the detector than low energy events, so we would not be getting an accurate spectrum if we ignored acceptance effects. At energies below 500 MeV the acceptance is also reduced due to the detector threshold. Figure 3.10 shows the fraction of Monte Carlo events which reconstructed as a fully contained neutrino event.

To calculate the final neutrino spectrum, we simply divide Figure 3.9 by Figure 3.10 to get the result in Figure 3.11. Here we see good agreement between data and Monte Carlo, but the large error bars at high energy are a result of the low efficiency of the kiloton for the measurement of high energy events. The spectrum assumes that the Monte Carlo can predict the shape and fraction of the non-quasielastic neutrino events. Uncertainties in the quasielastic fraction are known to be on the order of 30% and this represents a significant systematic error on the spectrum. We'll see more on this in the next section.

3.2 The Scintillating Fiber Tracker Data Analysis and Results

3.2.1 SFT Event Selection

Identifying tracks in the Scintillating Fiber Tracker is quite simple compared with a typical collider experiment. In any given event there are rarely more than three tracks, and since there is no magnetic field, the tracks are

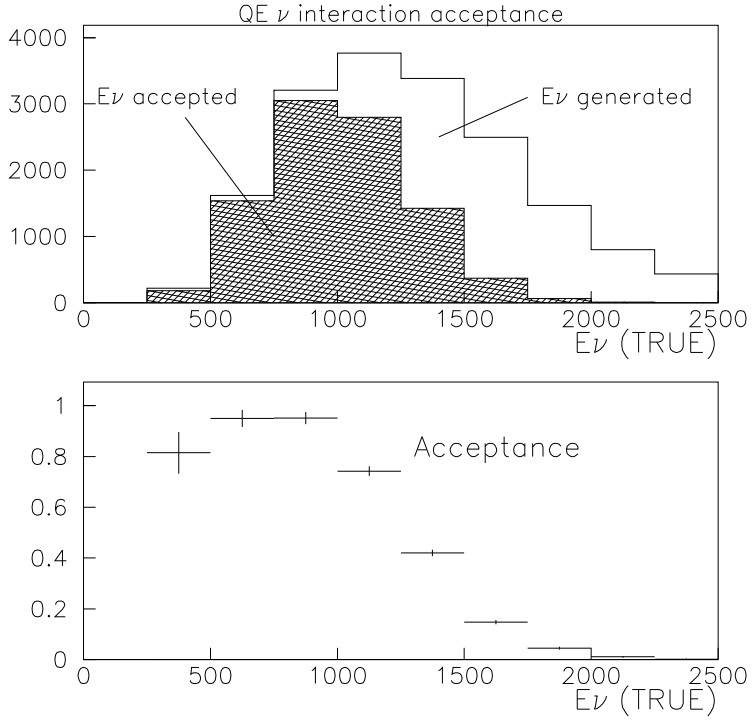

Figure 3.10: 1KT Fully Contained Acceptance

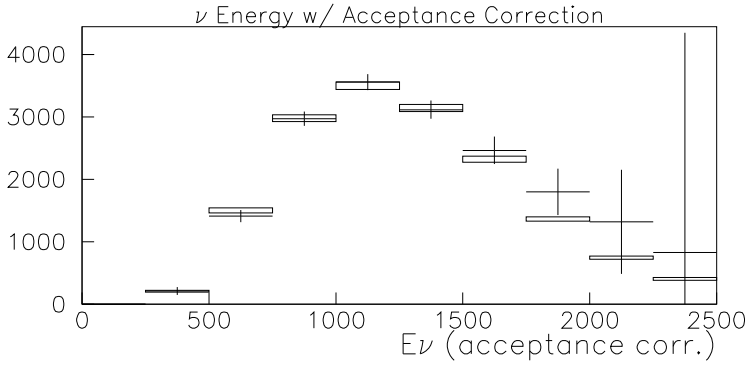

Figure 3.11: 1KT Fully Contained Background, Resolution, and Acceptance Corrected Neutrino Spectrum

straight. Finding tracks is a simple matter of identifying three or more hits which appear to be collinear. Track projections in the X and Y planes are identified independently, but can be matched by searching for tracks that have similar start and end Z positions.

The SFT can record two useful categories of events: neutrino events which originate within the SFT itself, and events in which particles created by neutrinos interacting in the kiloton exit that detector and strike the SFT.

The Scintillating Fiber Tracker cannot trigger itself. In order for the scifi data to be recorded and saved by the data acquisition system, one of the other fine grained detector components must have some activity, therefore we do not have the capability to study contained SFT events. All events must be entering from upstream or exiting the SFT downstream.

In order to identify an event originating inside the SFT, we require the following: The starting point of the track must be contained within the SFT fiducial volume, which is defined as the rectangular box 5 cm inward from the outermost fibers. The track must project onto a downstream veto hit within 50 cm in the X direction and 15 cm in the Y direction and must not project onto an upstream veto hit. The track must also match either a track or a hit in the first layer of the muon range detector. The time recorded by the MRD must also be consistent with the time recorded by the veto counter.

Entering events require that the track does match an upstream veto hit and that the start point is not within the fiducial volume. These events are not required to match to hits further downstream.

3.2.2 SFT Neutrino Spectrum

One large advantage of the SFT over the kiloton is its ability to sometimes see the proton track from a charged current quasielastic scatter. In the kiloton, a particle must be traveling above Čerenkov threshold in order to be observed. With an index of refraction of 1.35, a particle needs a γ of ≈ 1.49 to be observable. For a proton, this means a kinetic energy of around 500 MeV. Since a proton is much heavier than a muon, we expect the muon to carry away most of the energy in such a scatter. Therefore, in order to produce a 500 MeV proton, we will need a neutrino energy of several GeV. Although our beam contains such neutrinos, they're on the tail of our spectrum and won't be able to help us tag quasielastic events for the bulk of our spectrum.

Because the SFT relies on scintillation light, and not Čerenkov light, it has no such problems observing protons which would be below Čerenkov threshold. To be visible in the SFT, a proton only needs to have enough energy to cross three planes in both projections. This means that protons with a kinetic

energy of only around 150 MeV are visible in the SFT, and this is something which we can expect to see in significant quantities with our beam.

In the sample of events where the SFT observes two tracks, there's a mixture of charged current quasielastic scattering events where we see both the muon and the proton, charged current single pion events where we see the pion and muon but don't see the nucleon because it isn't charged, as well as some neutral current multi-pion events where we see two pions, and neutral current single pion events where we see a pion and a proton. Other reactions involving kaon production or other more exotic particles are too rare to be worth mentioning.

For quasielastic events, not only can we calculate the neutrino energy given just the muon direction and energy, we can also predict the direction of the scattered proton. We can define $\Delta\theta$ as the opening angle between the observed and predicted proton tracks. If this is near zero, it's likely to be a quasielastic event, otherwise, not. Figure 3.12 shows the $\Delta\theta$ for the two track data in the SFT compared with predictions for quasielastic and non-quasielastic events. In this plot, the relative normalization of the QE and non-QE events has been allowed to float and what is shown here is the best fit to the data. The $\Delta\theta$ distribution does not allow us to tag events as QE or non-QE on an event by event basis, but it does allow us to measure the quasielastic fraction, which is all we need to know for the background subtraction.

Employing the same basic analysis techniques as in the kiloton, with the exception of using the fit quasielastic fraction rather than assuming the default Monte Carlo value, we can calculate spectra for the one and two track samples as well as a combined spectrum, shown in Figure 3.13.

As with the kiloton, we see reasonably good agreement with the Monte Carlo prediction. Because this analysis uses information from the MRD in addition to the SFT, there are less problems with low acceptance at high energy.

3.3 The Lead Glass Detector Data Analysis and Results

The primary purpose of the lead glass detector is to study the ν_e contamination of the beam. When electron neutrinos interact in the SFT, they will produce an electromagnetic shower. Because the number of particles involved in a shower is so large, it is not possible to reconstruct individual tracks. However, showering particles which exit the SFT will strike the lead glass detector and stop. By measuring the quantity of light produced in the lead glass cells,

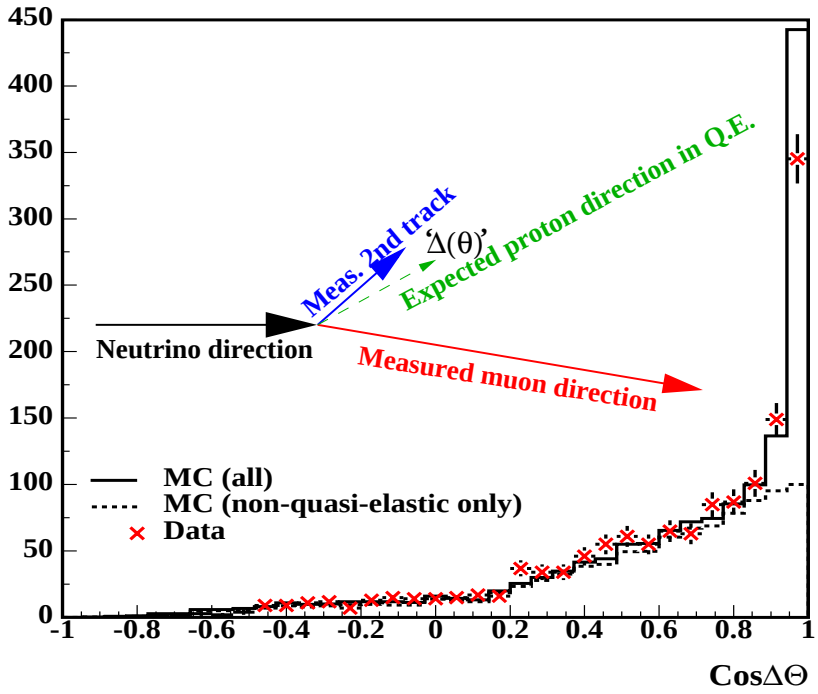

Figure 3.12: The distribution of differences between observed and expected directions of the second track, assuming quasielastic scattering.

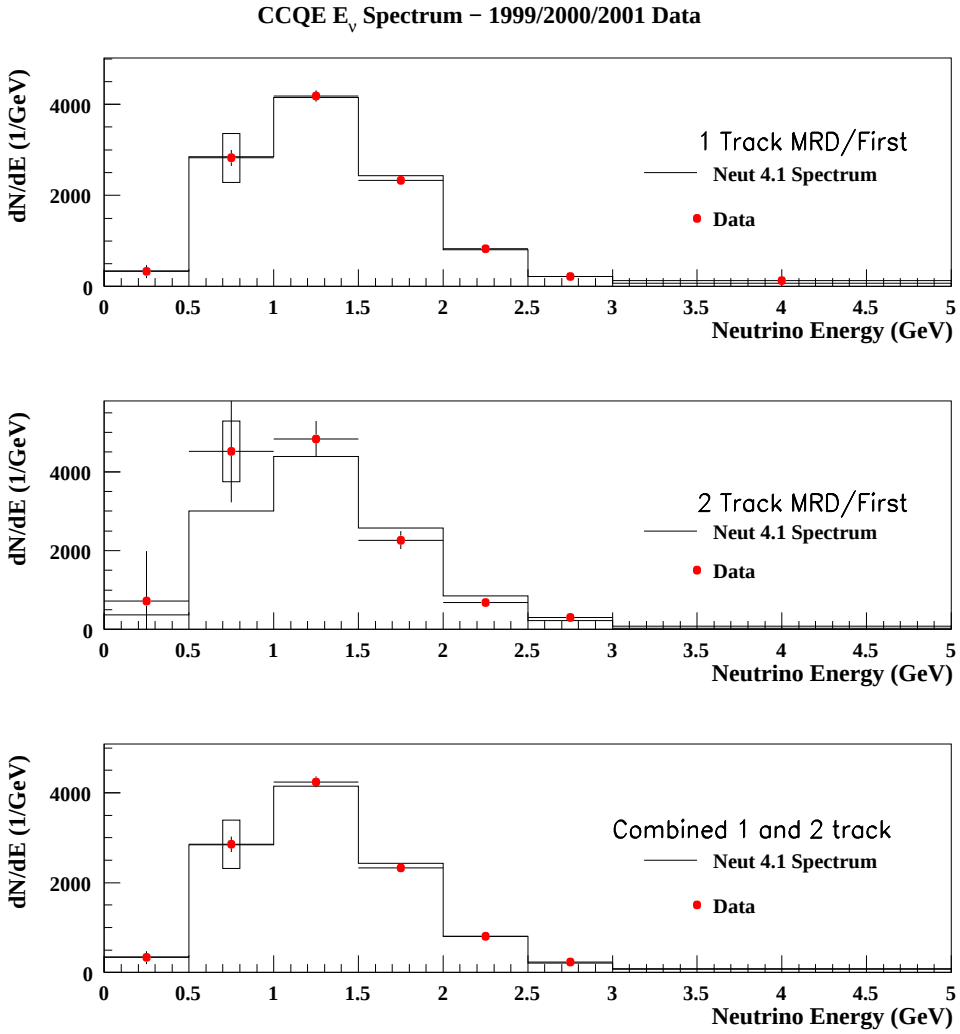

Figure 3.13: Scintillating fiber tracker final measured neutrino spectra.

it's possible to estimate the energy of the neutrino and construct a ν_e energy spectrum. This is of great importance for investigating $\nu_\mu \rightarrow \nu_e$ oscillations, but since the design of the K2K experiment, results from CHOOZ[26] have ruled out $\nu_\mu \rightarrow \nu_e$ oscillations with parameters in the K2K sensitive region. Nevertheless, it is important to understand our beam properties and the lead glass detector assists us in accomplishing that but detailed studies of ν_e events are beyond the scope of this thesis.

Electron neutrino candidate events can be selected by looking for events which deposit large amounts of energy in the lead glass array and downstream veto counter, but produce no track in the muon ranger. 20 MeV are required in the veto counter and 1 GeV in the lead glass. Figure 3.14 shows these cuts.

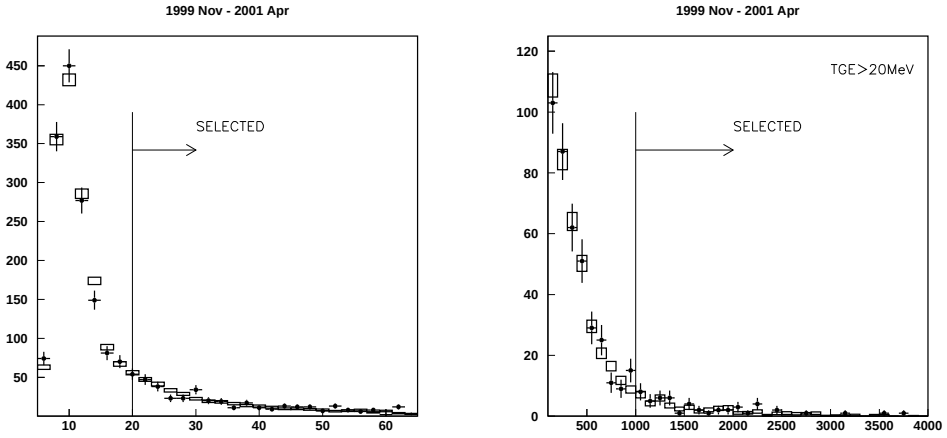

Figure 3.14: Lead glass event selection. An event is selected as a ν_e candidate if there is more than 20 MeV of energy deposition in the downstream veto counter and at least 1 GeV of energy deposition in the lead glass.

Between November of 1999 and April of 2001 51 electron neutrino candidate events were recorded with an expected background of 23.8 events. This gives the ratio of ν_e/ν_μ to be $1.6 \pm 0.43^{+0.76}_{-0.64}\%$.

Following the run ending in July of 2001, the decision was made to remove the lead glass detector. The electron neutrino contamination level has been measured and shown to be small and stable with time. This measurement is no longer limited by statistics. Because particles leaving the SFT must pass through the lead glass detector before being measured in the muon ranger, the lead glass array will block out the low energy portion of the muon spectrum which does not have sufficient energy to pass through the lead glass. For

this reason, continued presence of the lead glass detector would be counter-productive.

3.4 The Muon Range Detector Data Analysis and Results

3.4.1 MRD Event Selection

Event selection for the Muon Range Detector is similar to that of the SFT. Events in the MRD will consist of a small number of mostly straight tracks. Because the material separating layers of the MRD is iron rather than water, the energy deposition per layer in the MRD will be much higher than it is in the SFT (a minimum ionizing particle loses 13.7 MeV/cm in iron compared with 2.4 MeV/cm in water), so the energy scale available for study in the MRD is also much higher.

Event selection for the MRD is independent of all of the other detector components. The timing resolution of the MRD is not as good as the veto counter or kiloton detector, but it is sufficient to tag events as being in the beam spill window. As is the case in all drift chambers, the timing of a hit is convolved with its position. To deconvolve this, it would be possible in many cases to use the veto counter timing to provide the "T_0" for an event, but this is not done. Instead we choose a T_0 which minimizes the residual for the track fit. This allows us to perform track fits from MRD data alone and also allows us to fit tracks which do not intersect the veto counter, such as those originating within the lead glass or MRD itself.

To identify neutrino events originating in the MRD, we define a 73 ton fiducial volume consisting of the portions of the first three iron planes within three meters of the beam center. Tracks which appear to originate within this volume (i.e., no hits near the track in the most upstream drift chamber plane) are counted as neutrino events. A track is defined as collinear hits in both projections crossing at least two layers of iron.

3.4.2 MRD Neutrino Spectrum

Again, in the MRD we follow the same procedure as described for the kiloton. Figure 3.15 shows the neutrino energy for all events in the MRD fiducial volume with the predicted non-quasielastic background. After correcting for acceptance and resolution the final MRD spectrum is shown in Figure 3.16.

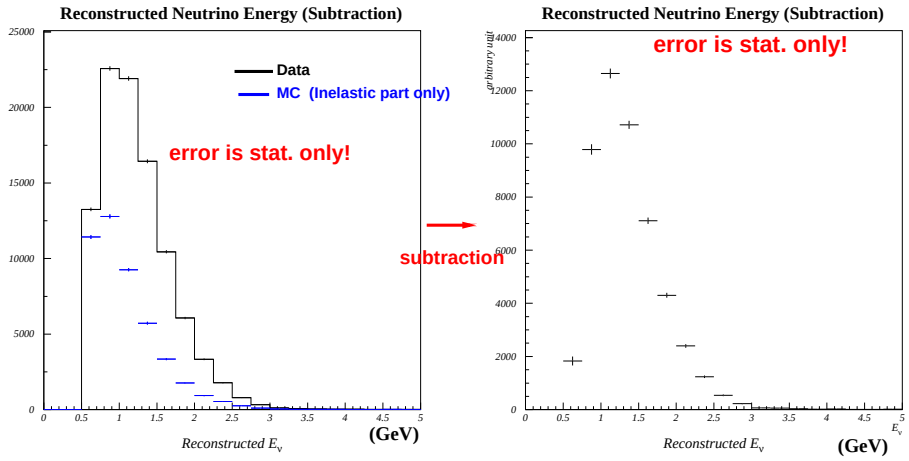

Figure 3.15: Muon Range Detector Observed Neutrino Spectrum

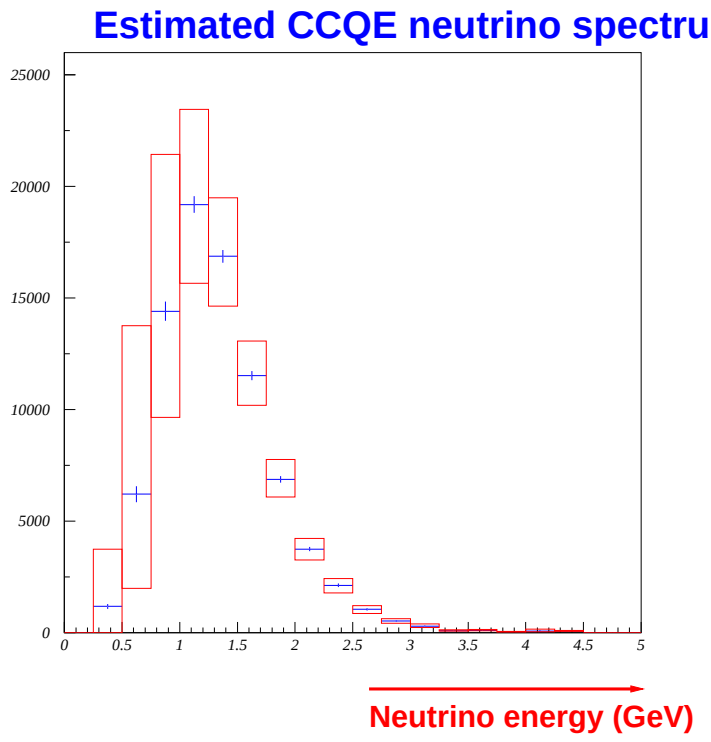

Figure 3.16: Final muon range detector neutrino spectrum after all corrections with systematic error boxes.

3.5 The Unified Analysis of the Near Detector System

In order for any one of the near detector components to measure the energy of a charged lepton, the particle must start and stop within that detector. As previously mentioned, the kiloton detector is not large enough to measure the high energy component of our neutrino spectrum. Such events will invariably produce muons which will escape the the detector, but they may stop in one of the other near detector components. If this happens, we can measure the energy loss in each sub-detector and reconstruct the total energy for the event. Such an event is shown in Figure 3.17.

To fully capture the high energy tail of the neutrino spectrum, we need to use the full near detector in unison. In this section, we will repeat the technique presented in Section 3.1.2, but this time we will not require that events be fully contained within the kiloton detector. Partially contained events which match with tracks in the fine grained detector will also be included.

3.5.1 Barriers to a Unified Analysis

Historically, the K2K experiment evolved largely as the collaboration of two separate camps, one group consisting of those people previously affiliated with Super–Kamiokande and the other of those people previously affiliated with KEK. The Super–Kamiokande group designed and built the kiloton detector, associated data acquisition systems, and software for data reduction, analysis, and simulation. The KEK group did the same for the FGD. Although physically close, these two systems were as separate as possible, and serious attempts at a unified analysis did not begin until late in the summer of 1999, well after data taking began.

All software related to the kiloton detector was stored on the "ichikilo" branch of the Super–Kamiokande CVS software repository in Kamioka. The code closely tracked Super–Kamiokande software, but contained the necessary revisions required for the kiloton detector. This software was written almost exclusively in Fortran for Solaris. Meanwhile, FGD software was written from scratch and stored and maintained in a separate repository at KEK. It was written in a mixture of Fortran, C, and C++, but tested almost exclusively on Linux systems. It was almost as if there were two separate experiments taking place on the same site.

Much of the time I spent working on this analysis was consumed by marrying these two sets of software with the computational equivalents of duct tape

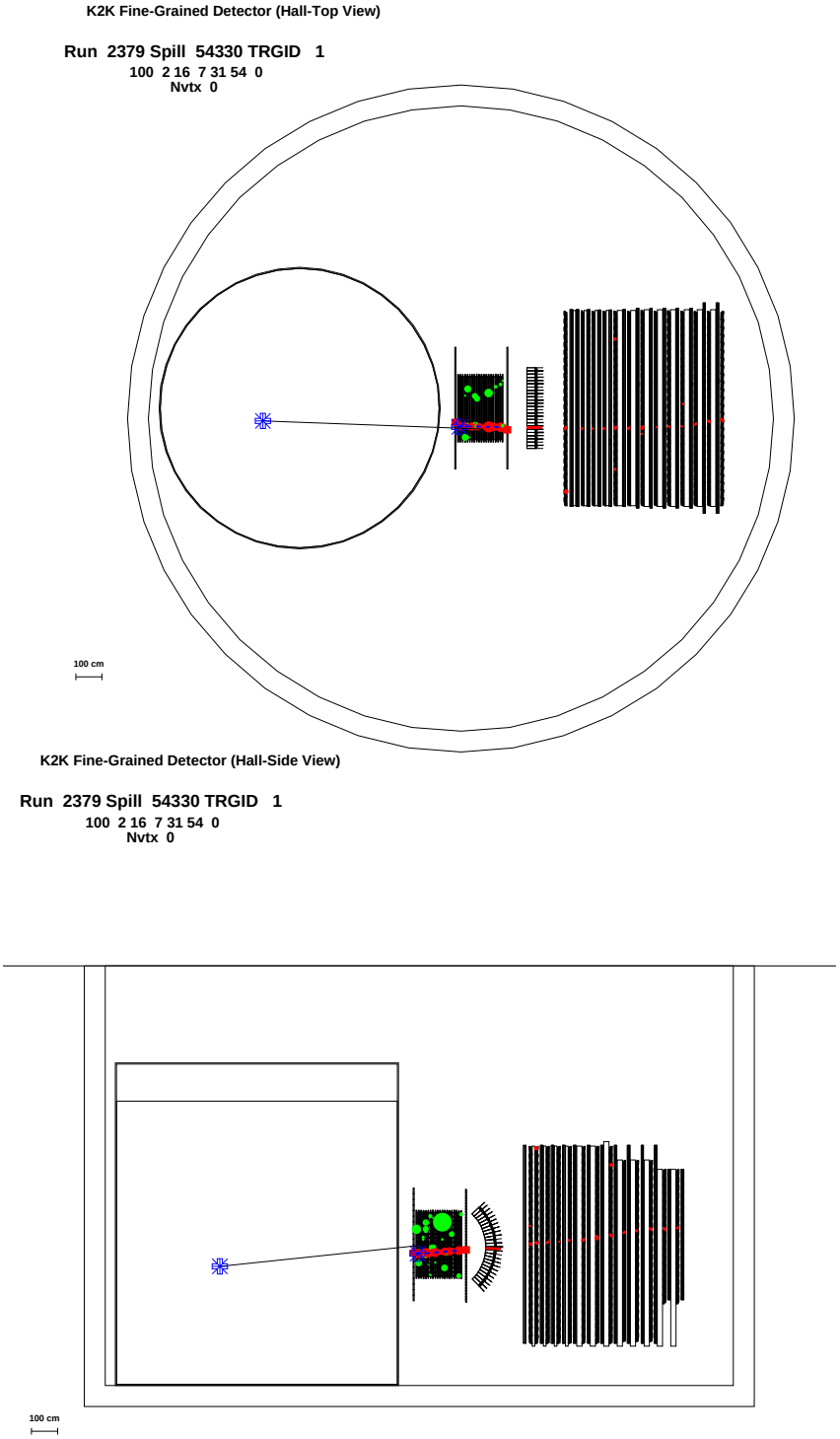

Figure 3.17: Top (upper figure) and side (lower figure) views of a single high energy event neutrino event occurring in the kiloton detector. The muon energy is too large to be contained in the kiloton, but the track is easily detected in the downstream FGD components.

and chewing gum. To start, both sets of software were cleaned of operating system or compiler specific assumptions and made to compile and run on both Solaris and Linux with either Sun or Gnu compilers.

To isolate a sample of events for study, it was initially necessary to build a database of known good spills in the kiloton data stream based on the presence of an identified single ring muon-like event originating from the fiducial volume. The FGD data was then processed to select events matching the same spill number and approximate event time.[1]

The FGD event display and data analysis software was modified to read its input from two files in parallel (one for KT data, and one for FGD data) and a crude kiloton vertex and track display mode was added (Figure 3.17). Both the the KT and FGD data formats are based on the Zebra Bank System[36]. Although this made some aspects of integration easier, it meant that both libraries were trying to access the same global data structures, often in incompatible ways. Modifications were needed to both sets of event reading libraries to get them to coexist peacefully.

In the spring of 2000 the data streams were merged and unified raw data files containing information from both the KT and FGD began to be produced by the new joint data acquisition system. Although this simplified the matching of data from different detectors, it made this analysis more complicated in other ways. The standard data analysis to identify neutrino events and perform fits is still separate to this day. To select events for the unified analysis, it became necessary to re-run the FGD data analysis on the output of the KT data reduction. Also, since older data has not been merged into the new form, both methods of reading data (from one file or two) need to be supported.

Although these tricks produced an apparent unified data source, more work was required to generate a unified Monte Carlo simulation. It was immediately apparent that merging the kiloton simulation with the FGD simulation was impractical. Instead, the kiloton simulation was altered to record all particles passing through a plane downstream of the detector. I then modified the FGD Monte Carlo simulation to read the output of the kiloton simulation and produce an output file containing both the kiloton simulation data and the simulation of the FGD response to both the particles coming from the kiloton as well as other particles expected to be present (cosmic rays, beam related radiation, and other beam neutrinos).

This two-stage Monte Carlo simulation does not cover certain classes of

[1] The K2K spill number is only 15 bits wide, so it loops around about every 20 hours. The run number and spill number alone are not sufficient to uniquely identify an event.

events, namely any event in which particles move upstream from the FGD area to the kiloton. At this time it is assumed that these are small in number and not important.

Once the logistical issues involved with producing the unified data and Monte Carlo sets and the tools to read them are out of the way, the rest of the analysis becomes almost trivial.

3.5.2 Unified Near Detector Event Selection

To match tracks in the kiloton detector with tracks in the fine grained detector, we need to consider the pointing accuracy of the kiloton. Figure 3.18 shows the distribution of angles formed by true Monte Carlo tracks and their fit directions. The kiloton has an angular resolution of about 70 milliradians, but a nonnegligible tail out to 300 milliradians. Since background levels are low, we can design our cuts to include this tail without fear of contamination. Projecting from the center of the tank, this translates to an spatial accuracy of about 2 meters at the front face of the SFT, 3 meters at the downstream veto counters in front of the lead glass, and 4 meters at the front face of the muon ranger.

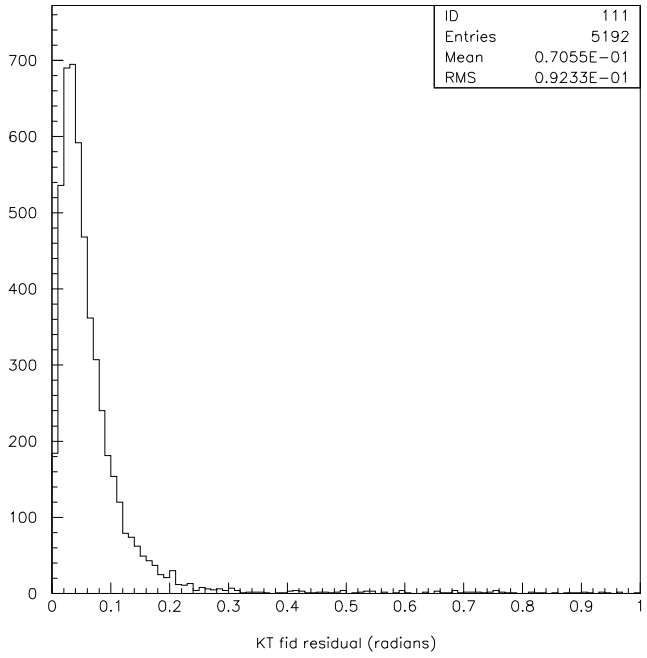

Figure 3.18: 1KT Angular Fitting Resolution

If a hit in the veto or track start in the SFT or MRD falls within these ranges, then we may associate the track with the kiloton event. For SFT or MRD tracks, we also require that the angle of the track match the predicted kiloton angle within 20° for the SFT and 30° for the MRD. This corresponds to the 300 milliradian kiloton resolution convolved with the resolutions for the SFT and MRD, with some additional allowance for multiple scattering on the way to the MRD.

If the kiloton track matches a scintillating fiber track, then the SFT track is projected on to the MRD track instead of using the kiloton track. In this case, the SFT cuts of 2 meters and 20° are applied to the MRD track as well. Figure 3.19 shows how the data distributes relative to these cuts.

In addition to these cuts, it is also required that the SFT and MRD tracks start at the front face of each detector, that the SFT track extrapolate backward to a matching veto hit, and that veto hits agree with the kiloton transient digitizer peak time within 65 ns.

The cleanliness of this sample can be judged by how often a match is made for events which are not tagged as exiting by the presence of a saturated tube in the kiloton detector. For data collected in the year 2000, these criteria match 2953 kiloton and FGD events, and all but 23 have saturated tubes. Given that we should expect most accidental matches to occur with fully contained events (because they are more numerous) we can conclude that the loose cuts we have applied do not allow excessive quantities of background into the sample.

3.5.3 The Unified Near Detector Neutrino Spectrum

Once these cuts are applied and the partially contained kiloton tracks are matched with tracks in the FGD, the muon energy can be calculated by summing the ionization energy loss in each of the near detector components and a corresponding neutrino energy can be calculated. Figure 3.20 shows the energy loss in the FGD for both data and Monte Carlo predictions.

The analysis then proceeds in a similar fashion to the fully contained spectral measurement up to the point of detector resolution deconvolution. Figures 3.21 through 3.24 show the process of deriving the background subtracted neutrino spectrum.

At this point the analysis must break from the methods employed to analyze the fully contained events. Figure 3.25 shows the energy migration map for these events. The bin size is the same as in the fully contained analysis (Figure 3.8), but the axes have been lengthened to 5 GeV to include the higher energy neutrinos. Unfortunately, attempts to invert the matrix formed by this histogram will not produce meaningful results. There is not significant sta-

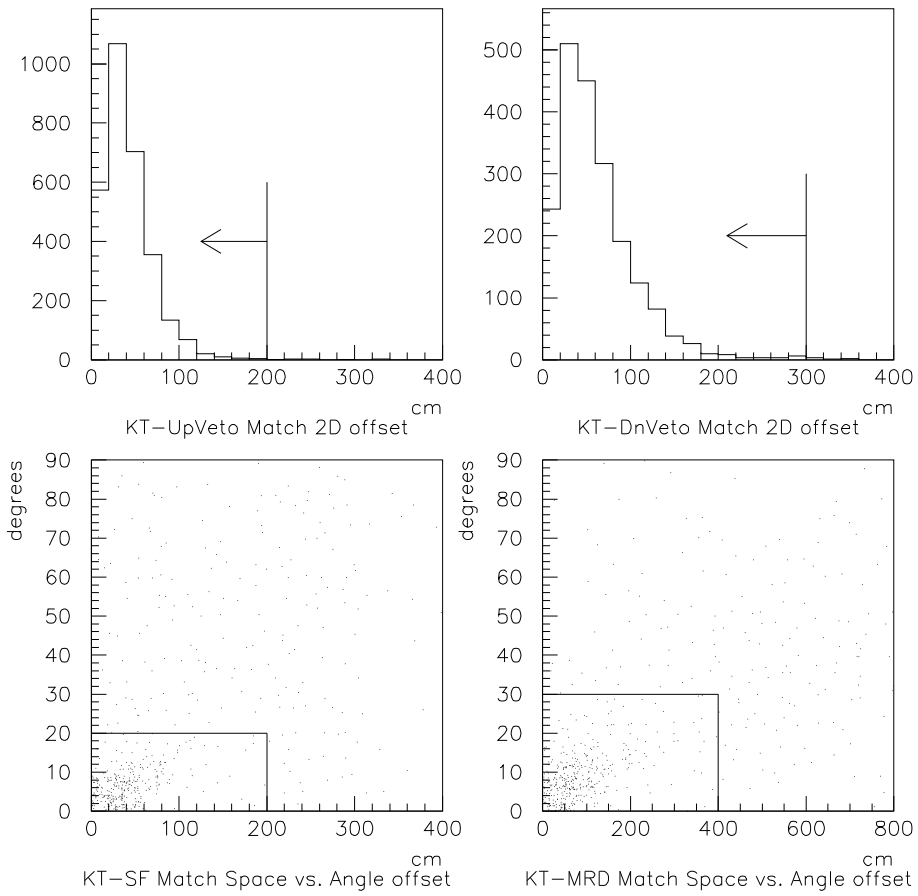

Figure 3.19: Geometric cuts used to select events for the unified kiloton-fine grained analysis. Veto counter hits are selected within 2 meters (upstream) or 3 meters (downstream). SFT tracks are selected if they match the kiloton track within 2 meters and 20°. For events with no SFT track, MRD tracks are selected within 4 meters and 30°. These cuts are loose because background levels are low.

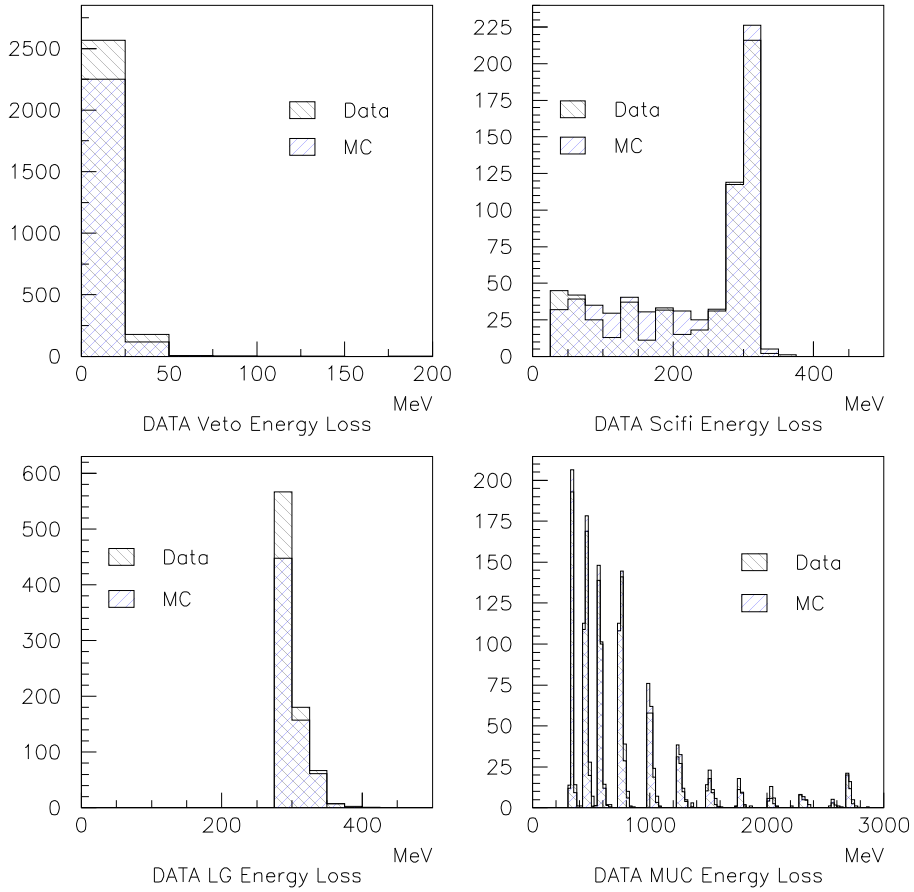

Figure 3.20: Ionization energy loss in FGD components from muons originating in the kiloton. The general shape of data and Monte Carlo agree, but there are more matched events per spill in the data. The muon chamber energy deposition is quantized since only the number of layers is recorded, but the spikes are widened slightly by particles traveling at different angles. The final spike around 2800 MeV contains more events than the previous spike because it includes all particles with energies above 3 GeV, which pass through the entire MRD.

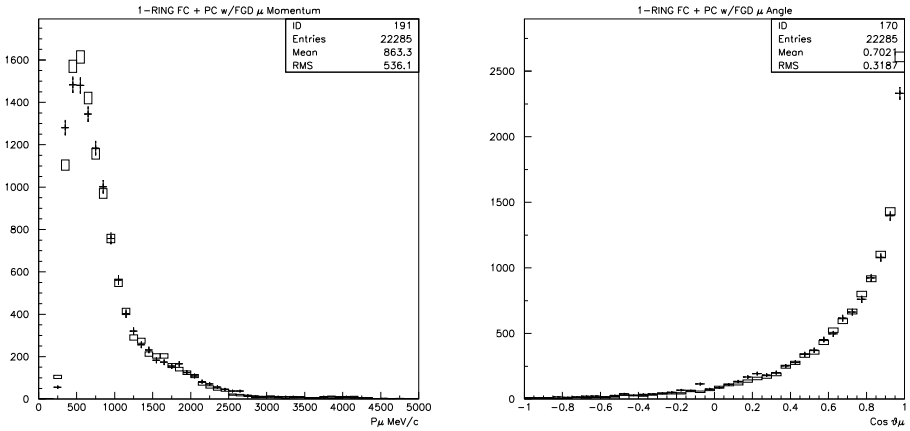

Figure 3.21: 1KT fully contained and partially contained with FGD matching track muon momentum and angle distributions

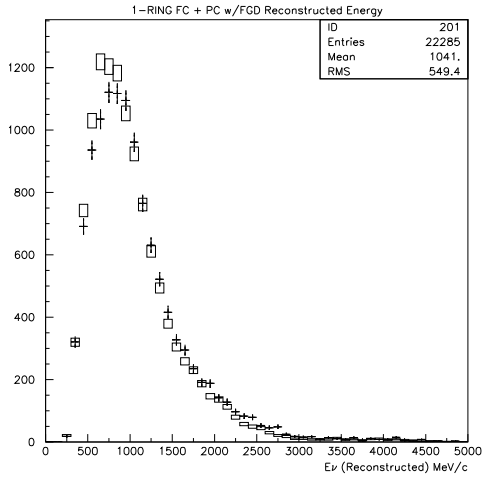

Figure 3.22: 1KT FC + PC w/FGD track reconstructed neutrino energy

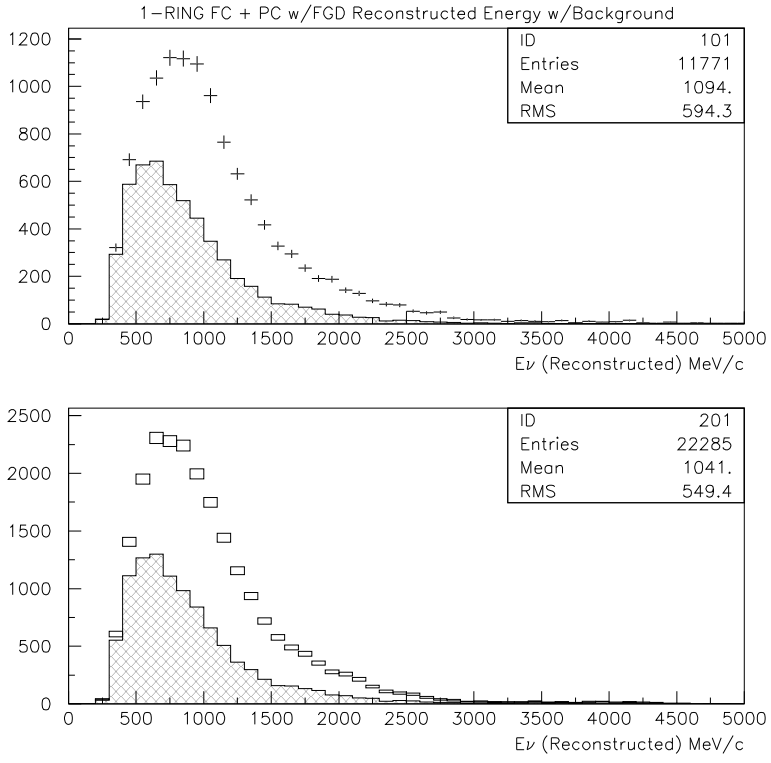

Figure 3.23: 1KT FC + PC w/FGD track reconstructed neutrino energy with estimated non-quasielastic background

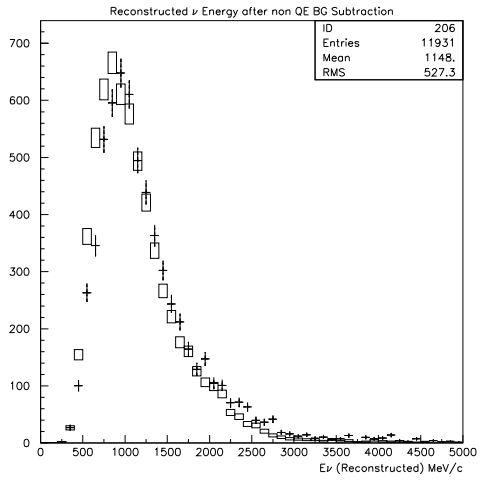

Figure 3.24: 1KT FC + PC w/FGD track reconstructed neutrino energy with non-quasielastic background subtracted

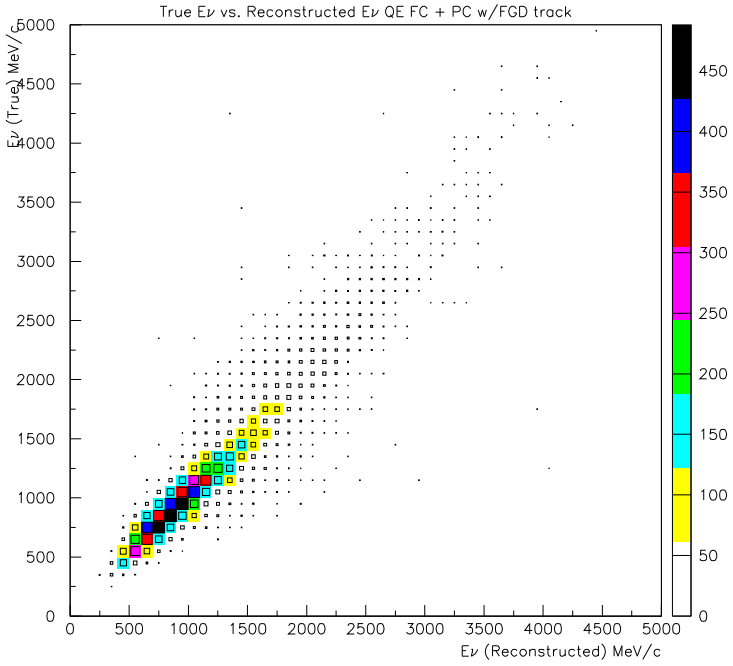

Figure 3.25: 1KT FC + PC w/FGD QE MC energy migration map

tistical power in the high energy portion of the Monte Carlo to perform this deconvolution.

Even if more Monte Carlo events were generated to fill out the high energy portions of the matrix, there are too few events in the data to distinguish between a smoothly falling high energy tail, and one with large spikes which would be washed out by resolution and statistical variation.

It is precisely because of this kind of problem that it is better to use the raw detector measurements to tune the beam Monte Carlo rather than attempting to draw significant meaning from spectra measured in the front detector.

A more simplistic method for removing detector resolution effects is to use a one dimensional Monte Carlo efficiency function. The Monte Carlo efficiency is defined as the number of events which reconstruct in a given energy bin, divided by the number of events generated in that bin. This efficiency can be inverted, as shown in Figure 3.26, and applied to the data as a correction factor. This isn't as effective doing the full matrix deconvolution, but it is more likely to lead to sensible answers when statistics are low. Once the resolution correction is done, the acceptance correction can be done using the same method as in the fully contained analysis.

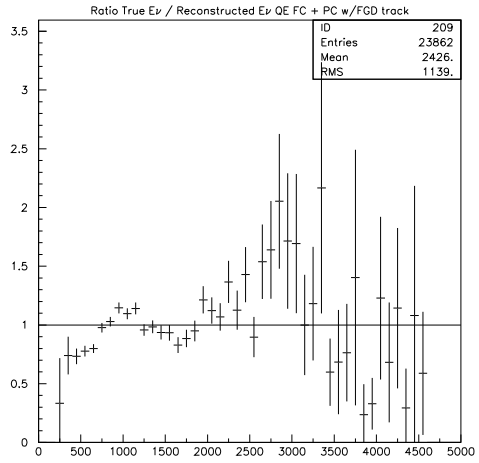

Figure 3.26: 1KT FC + PC w/FGD QE MC true spectrum / measured spectrum

The final result of this analysis is shown in Figure 3.30. As in the fully contained case, the dominant systematic error is the quasi-elastic fraction. This quantity was allowed to vary by 30%, producing the large systematic

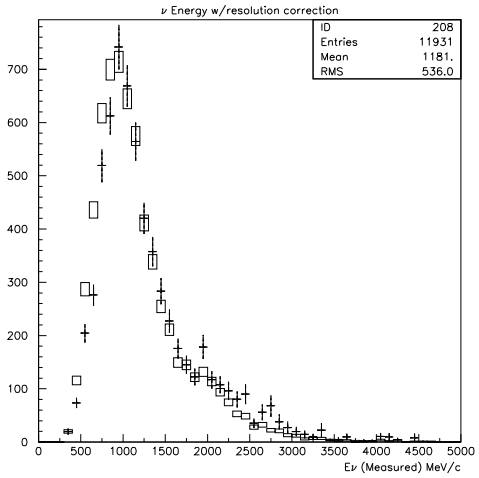

Figure 3.27: 1KT FC + PC w/FGD resolution corrected neutrino energy

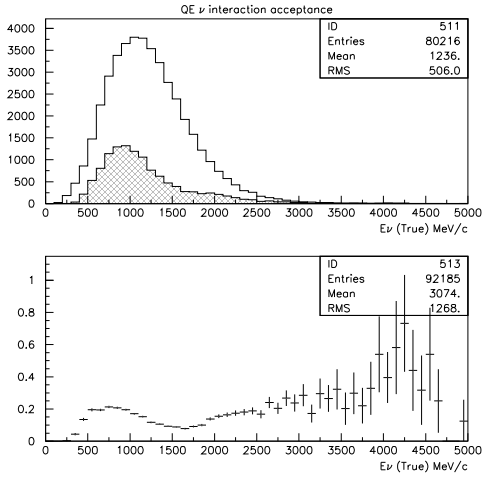

Figure 3.28: 1KT FC + PC w/FGD acceptance

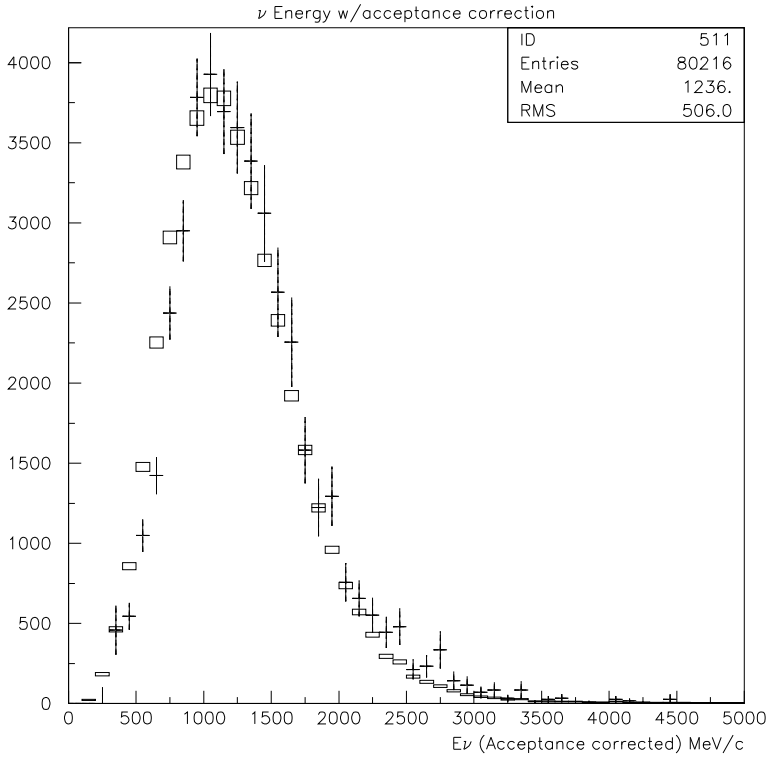

Figure 3.29: 1KT FC + PC w/FGD acceptance corrected neutrino spectrum

error boxes shown here.

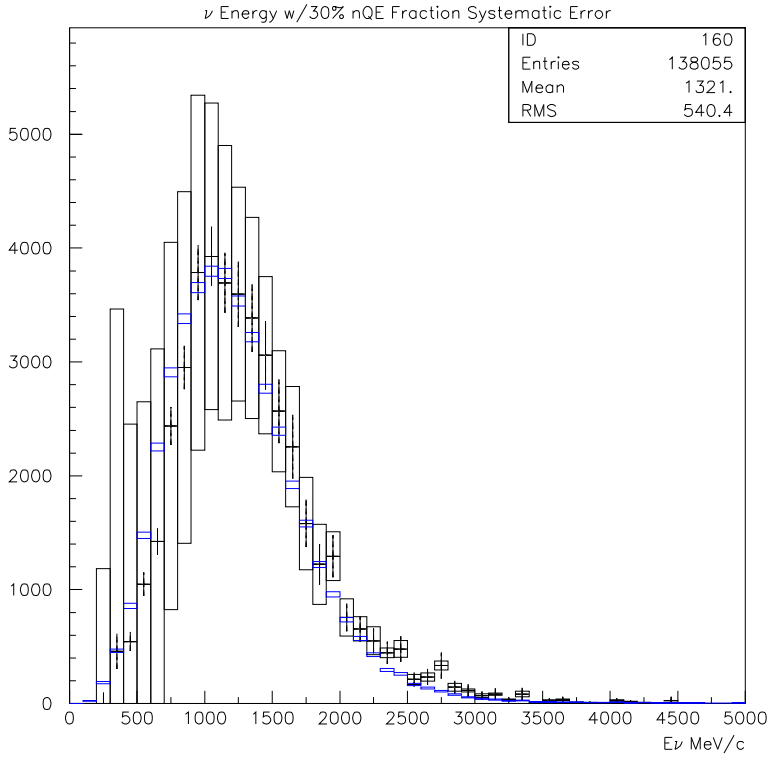

Figure 3.30: 1KT FC + PC w/FGD systematic error due to nQE ratio

3.5.4 Importance of Unified Near Detector Studies

To understand the neutrino spectrum of the K2K beam at the percent level, it's essential to study the high energy tail. Neutrinos at the highest of these energies are produced by fundamentally different processes, most commonly the production and decay of kaons rather than pions. Kaon production cross sections are not very well known and studies such as this can actually improve these measurements.

Already, this study has shown that the input spectrum to the near detector simulations used prior to the summer of 2001 (Figure 3.31) had a significant deficiency in the high energy tail. The original spectrum had an artificial cutoff at 5GeV, which resulted in the absence of the final spike seen in the

muon ranger energy deposition in Figure 3.20. Only once this cut-off was removed did data and Monte Carlo agree.

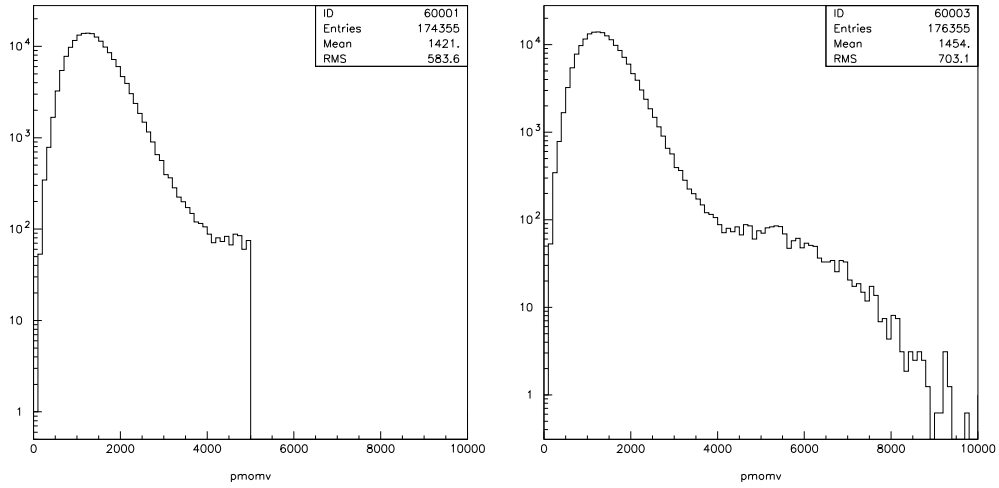

Figure 3.31: Beam MC neutrino spectra at the front detectors. Initial MC simulations were based on a spectrum (left) which contained an artificial cut-off at a neutrino energy of 5GeV. This lead to a significant discrepancy in the number of high energy muon events observed passing from the kiloton detector through the entire FGD. When the full spectrum was used (right) the discrepancy was resolved.

Chapter 4

Extrapolating to Super–Kamiokande

The most difficult and critical calculation to be made for the K2K experiment is, without question, the prediction of the neutrino flux at Super–Kamiokande. The whole experiment rests on this calculation. The signal for neutrino oscillations is the deviation of the measured neutrino flux from the expected neutrino flux in the absence of oscillation. Without the ability to form an accurate prediction, the K2K experiment has no sensitivity.

4.1 Beam Monte Carlo

The primary tool for making this prediction is a Monte Carlo simulation of the beam. This is a standard GEANT based simulation of the beam, target, magnetic horns, and decay pipe. The size and shape of the proton pulse is taken as input from beam profile monitors just upstream of the target.

The interaction of protons with the aluminum target is based on a custom implementation of a parameterization developed by Sanford and Wang[38] using existing measurements of production cross sections. The shape of the charged pion production is modeled after data recorded by Derrick[37] at the ANL Zero Gradient Synchrotron, although the normalization has been increased by about 20%. Charged kaon production is taken from a KEK report by Yamamoto. Neutral pion and kaon production is derived from charged pion and kaon production. All of these measurements were for protons on beryllium targets, so the extrapolation to an aluminum target was based on the work of Busza, *et al.* For particles with energies below 10 GeV, GEANT was allowed to use its default internal models.

This simulation gives us reasonably good estimates of neutrino flux at various points along the beam-line. We can compare beam Monte Carlo predictions for pion and muon fluxes to data measured by the beam monitors.

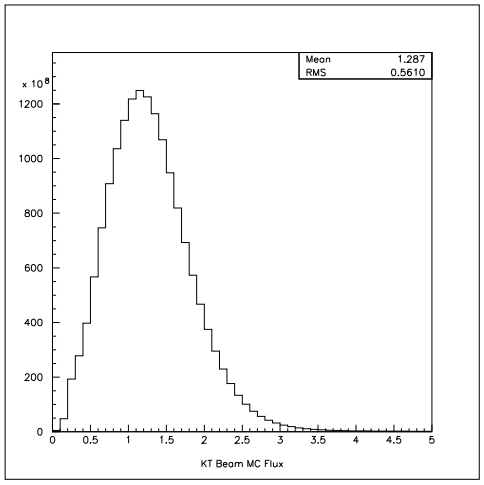

Figure 4.1: Beam MC Prediction for ν_μ Flux at the Kiloton

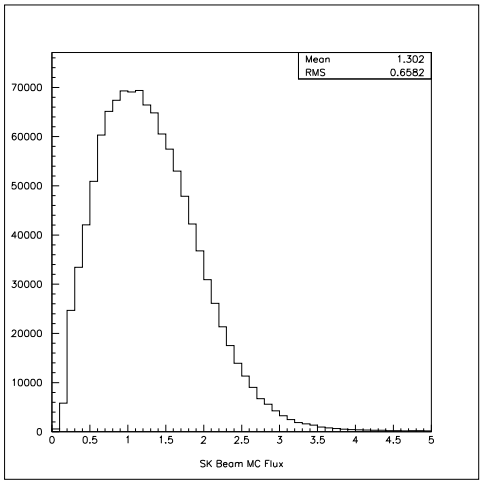

Figure 4.2: Beam MC Prediction for ν_μ Flux at SK

It is possible to use this information directly to predict the event rate at Super–Kamiokande without any information from the front detector but we don't do this. For one, the beam Monte Carlo produces a prediction of neutrino flux, not neutrino event rate. The neutrino event rate is dependent on the neutrino interaction cross section. In other words, what we actually measure, the neutrino event rate, is the product of neutrino flux and neutrino cross section, and neutrino cross sections are not well known quantities. This would introduce a systematic error which would be on the order of 20% or more, which is similar to the size of event rate reduction we expect to see for certain areas of the parameter space. Other uncertainties in nuclear modeling of the proton-aluminum interaction introduce comparably large systematic errors on pion and kaon production rates, angles, etc. However we can tune the beam Monte Carlo to agree with the front detector measurements. This tuning process can actually set new limits on the nuclear modeling parameters and neutrino interaction cross sections, providing interesting spin-off physics results from the K2K experiment.

One look at Figure 4.3 is all that is needed to see why such care is needed for the flux extrapolation. The flux ratio itself shows energy dependent variations of more than a factor of two across the spectrum. If we were to ignore this spectral variation in flux, we could easily fool ourselves into thinking we have observed neutrino oscillations even if we had not.

There are several different effects going on which cause this "flux oscillation", but it really all comes down to the geometry of the beamline and

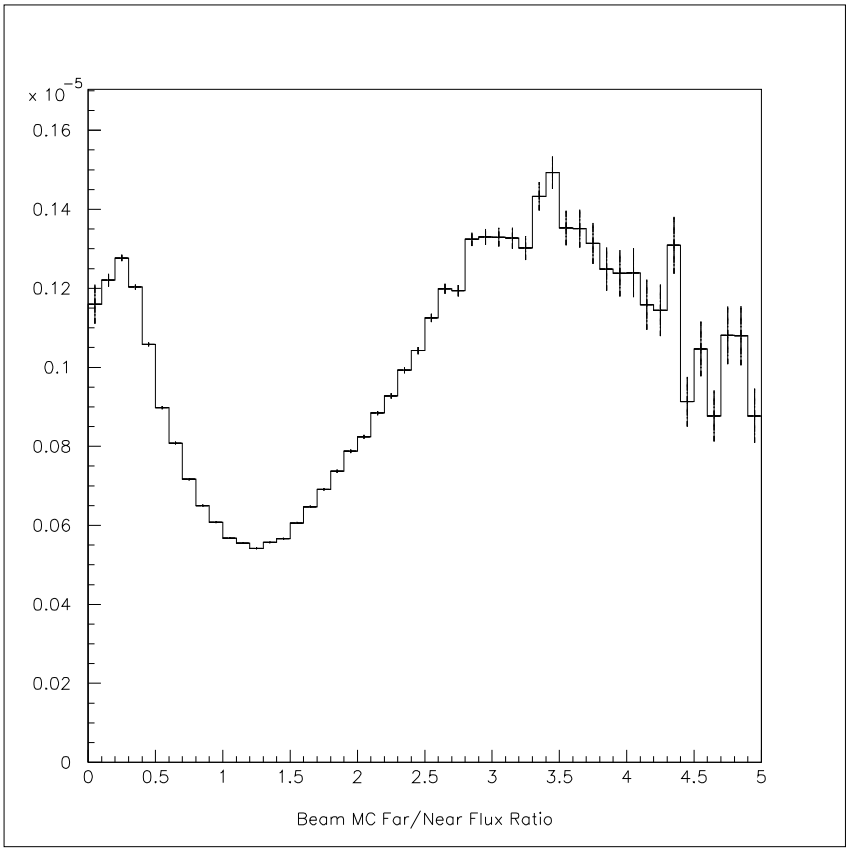

Figure 4.3: Beam MC Prediction Far/Near ν_μ Flux Ratio

detectors. We rely on the Lorentz boost from the pion momentum to point the neutrinos in the forward direction, but lower energy neutrinos mostly come from lower energy pions. Therefore the Lorentz boost will be less significant, and these pions will have a much wider spread. As we look at higher and higher energy pions, they become more finely columnated as the effect of the Lorentz boost becomes stronger, increasing the far/near ratio.

However, at the lowest energies there is a competing effect which goes the other way. The ratio of the solid angles subtended by the two detectors is a function of position. As you move from the target toward the near detector, the angle subtended by the near detector grows significantly, while the angle subtended by Super–Kamiokande changes very little. Because time dilation causes the higher energy pions to decay later, they will, on average, be closer to the near detector when they decay than lower energy pions. This effect decreases the far/near ratio as you go to higher energies.

The mean decay length for a particle can be given by $\gamma\beta c\tau$, or $E\beta\tau/mc$, while the distance from the target to the end of the beam dump is about 220 meters. The effect of the decay time will begin to diminish around $E = Lmc/\beta\tau$ or about 4 GeV for pions. Below this energy, most of the pions will decay before reaching the beamstop, which means there won't be many pions available to decay near the beamstop, so the neutrino production rate in this vicinity will be diminished. Above this energy, there will be significant numbers of pions throughout the beam pipe, so the neutrino production rate will be fairly constant. We know from simple kinematics that the maximum energy neutrino that occur from the decay of a 4 GeV pion will be $4\text{GeV} \times (1 - m_\mu^2/m_\pi^2) \approx 1.7\text{GeV}$. The mean energy of such neutrinos is closer to 1.3 GeV, which is about where we see the ratio level off and the effect of the Lorentz boost begin to dominate.

4.2 The Expected Neutrino Spectrum at Super–Kamiokande

The first step in any analysis is to calculate the expected observable neutrino spectrum at Super–Kamiokande, which is the neutrino flux convolved with the interaction cross sections. For the case of no oscillations we take the spectrum from the beam Monte Carlo tuned by the front detector. We then determine how oscillations would effect that spectrum.

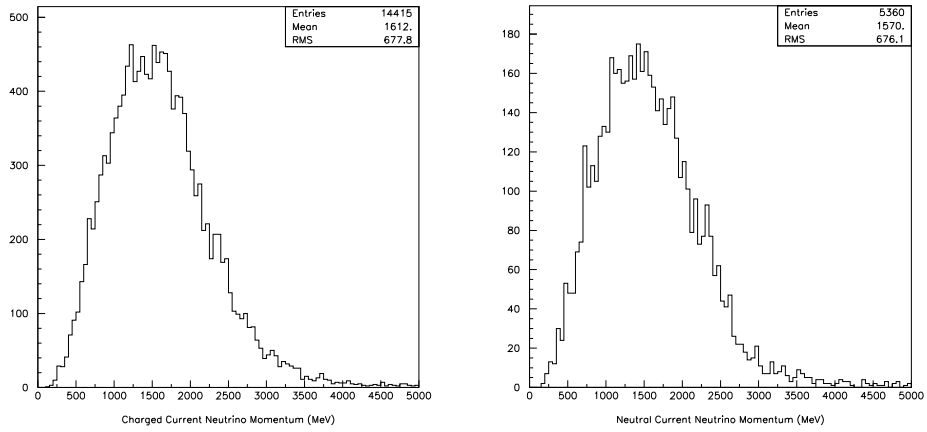

Figure 4.4: Beam MC predicted Neutrino Interactions (Flux × Cross Section) for Charged Current (left) and Neutral Current (right) interactions

We need to consider neutral current and charged current interactions sep-

arately. Excepting the possibility of a sterile neutrino, neutral current interactions will be unaffected by neutrino oscillations, while charged current interactions will be diminished. Figure 4.4 shows the expected neutral and charged current distributions separately for our beam. For each set of oscillation parameters we consider, we'll weight the events in the charged current distribution by Equation 1.1. Events in the neutral current distribution will be given full weight.

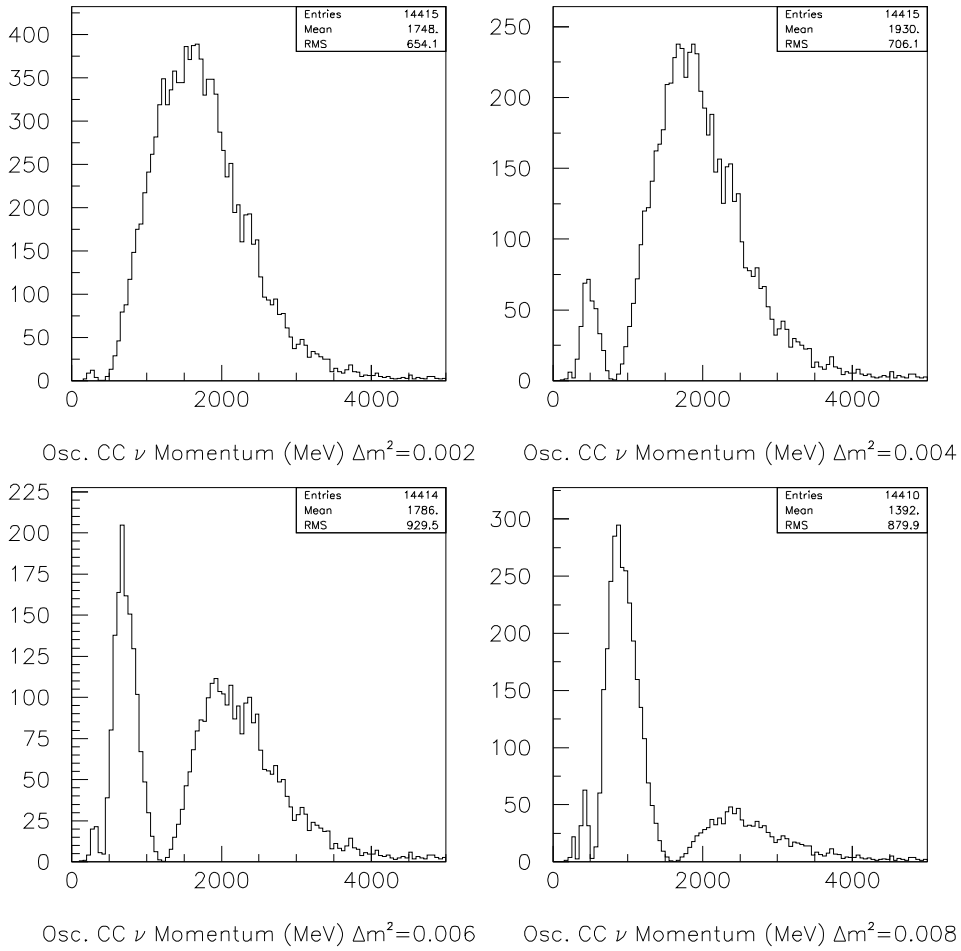

Figure 4.5: The effects of oscillation on charged current neutrino interactions are unmistakable. No cuts or detector effects have been applied in this plot.

Figure 4.5 shows the effects of oscillation on the spectrum of charged current neutrino interactions for maximal mixing at various values of Δm^2. At very small values of Δm^2 there is almost no effect, just a small decrease at

very low energies. As Δm^2 increases, there's a clear chunk taken out of the spectrum where $1.27 \times L/E \times \Delta m^2$ is $\pi/2$ and the oscillation probability is 1.0. As Δm^2 increases, this characteristic energy increases and it becomes possible to see higher order nodes at $3\pi/2$ and $5\pi/2$.

Of course, we have no hope of measuring such a clean spectrum. In reality, charged current events cannot be fully isolated from neutral events and we have no way of accurately determining the neutrino energy for events which are not simple quasi-elastic scattering because we can rarely record the energy carried away by the nucleons involved in the interaction. Instead, as with the near detector, we enhance the charged current quasi elastic fraction by selecting events which produce a single μ-like ring, and then assume the neutrino direction and compute the energy using Equation 3.1. Figure 4.6 shows the distributions we would be likely to observe under these conditions.

Although the oscillation effects are not as sharp as in Figure 4.5, they are still distinctive enough to provide an observable signal.

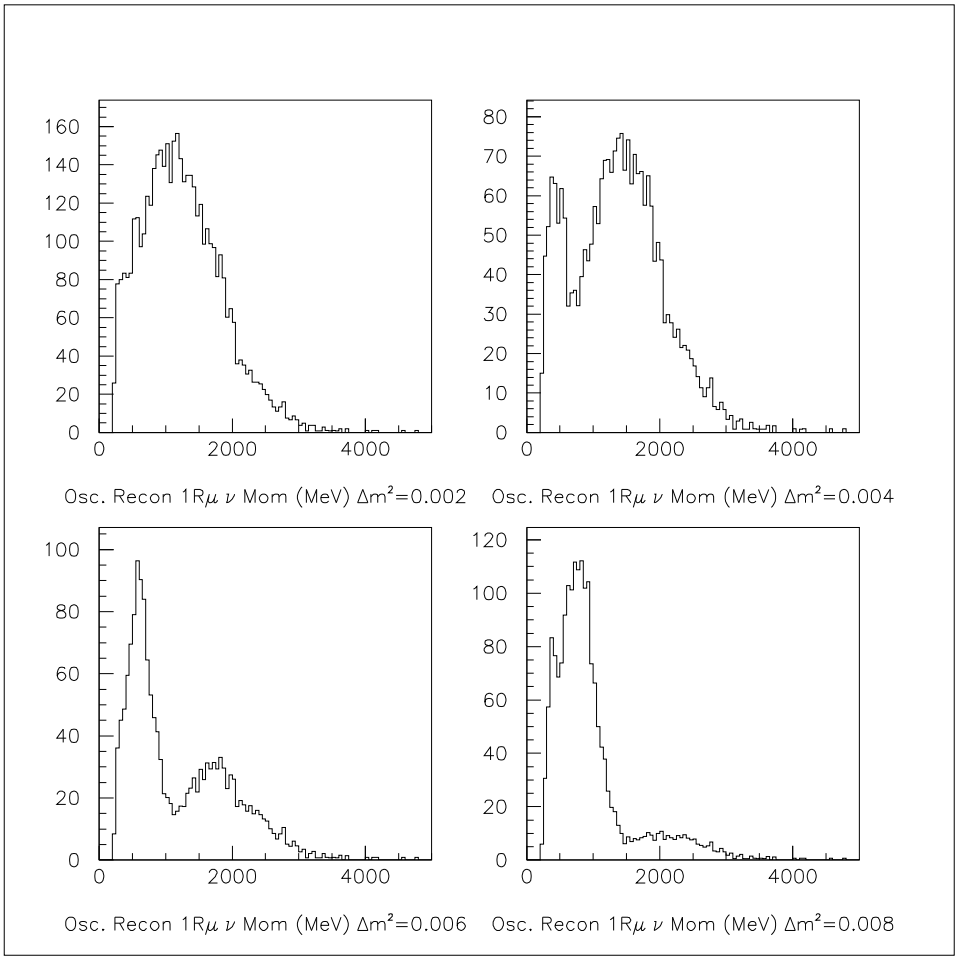

Figure 4.6: The observable effects of oscillation are not as pronounced as in the previous plot. NC contamination and energy resolution effects blur the oscillation signal.

Chapter 5

Super–Kamiokande Events

5.1 Super–Kamiokande Event Selection

Although the neutrinos produced at KEK are not fundamentally different than normal atmospheric neutrinos, the reduction process used to select these events is.

Super–Kamiokande is continuously bombarded by high energy cosmic ray muons that manage to punch through the entire mountain, as well as events known as "flashers", where two dynodes in a PMT create a spark which produces enough light to trigger the detector. These events are filtered out of the atmospheric event sample by a sophisticated series of fitters which attempt to understand and classify each event. A thorough description of the atmospheric neutrino event selection is provided by Kenji Ishihara's doctoral thesis[40].

Unlike atmospheric neutrinos, K2K's neutrinos occur at predictable times. By recording the time at which protons strike the target at KEK and adding the time of flight to Super–Kamiokande, it is possible to predict the arrival time of the neutrinos with very high accuracy. Any event occurring outside of this time window is obviously not related to the beam.

Because this timing cut eliminates nearly all background events, and because our signal events are so few in number compared with atmospheric neutrino events, the tight cuts applied by the Super–Kamiokande atmospheric reduction are not appropriate. We can loosen the cuts significantly to retain more signal without significant increase in the background.

We define the quantity ΔT for each event as:

$$\Delta T = T_{KEK} - T_{SK} - T_{TOF}$$

where T_{KEK} is the start time of the closest spill at KEK, T_{SK} is the time at which the event is observed at Super–Kamiokande and T_{TOF} is the expected

time of flight for a neutrino to travel from KEK to Super–Kamiokande. Ideally, all beam related events will have a ΔT between 0 and 1.1 μs, corresponding to the duration of the spill.

As mentioned in Section 2.2.3, it's possible to divide high energy neutrino events into two groups: those that occur entirely within the inner detector, and those that do not. We refer to these event classes as fully contained and outer detector events[1]. The reduction of these two event classes will be discussed separately.

5.1.1 Fully Contained Events

Figure 5.1 shows the event reduction process. The horizontal axis shows ΔT for each event. The top line is all events with a high energy trigger within 500 μs of a spill and more than 100 μs from the previous event. The purpose of the 100 μs dead time is to eliminate events caused by the decay electron from a stopping muon.

Below that are events with between 200 and 50000 photoelectrons (corresponding to the expected range of energy deposition from K2K neutrinos), where no single tube registers more than 0.5% of the photoelectrons for the event. Events with more than 50000 photoelectrons can only be caused by very high energy through going cosmic ray muons, and events with less than 200 are too low in energy to be associated with the K2K beam. The 0.5% photoelectron cut is designed to remove flashers.

And finally, at the bottom, are events which have a vertex which fit inside the fiducial volume of the inner detector and have little or no activity in the outer detector. The Super–Kamiokande fiducial volume is defined as the cylinder inside the inner volume containing all points more than 2 meters from the nearest detector wall. There is a clear peak at zero, with only one outlier.

Changing scales by two orders of magnitude, it's possible to see how accurately this timing difference can be measured and the complete absence of a background level. The beam spill gate is 1.1 μs long, and the accuracy of the GPS timing is 0.1 μs. We use a 1.5 μs timing window cut corresponding to the spill gate convolved with twice the GPS accuracy.

Expected background levels are extremely low. In a typical day, there will be 20 atmospheric neutrino events in Super–Kamiokande. The KEK ps spill

[1] Within the Super–Kamiokande literature the term "partially contained" is used to denote events that extend out of the inner detector into the outer detector. "OD events" are a superset of these, including events which originate in the outer detector or events with no significant inner detector activity at all.

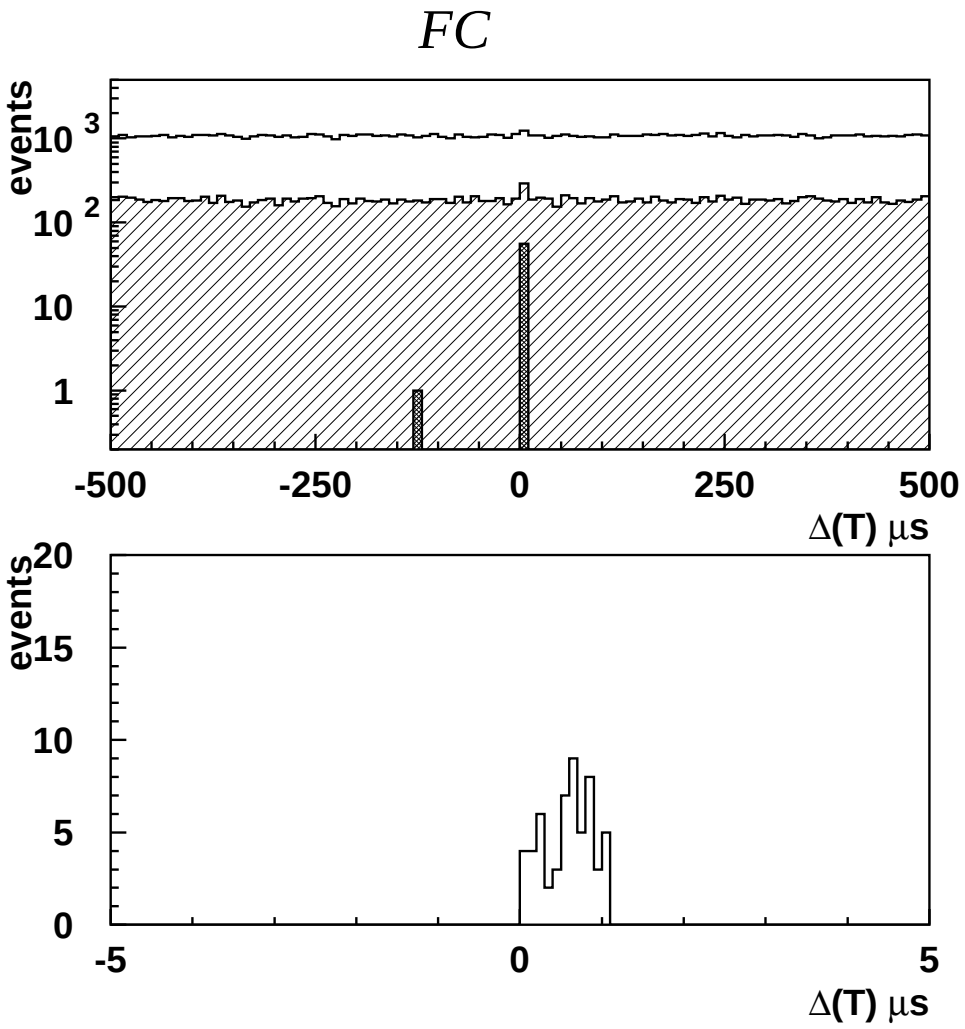

Figure 5.1: K2K event reduction at SK. The upper portion of this figure shows: (1) High energy trigger events after a +/-500 μs timing window cut and decay electron cut, (2) the same events after requiring the total number of inner detector photo-electrons to be $\geq$ 200 and <50000 and requiring that no single tube contain more than 0.5% of the photo-electrons for the event, and (3) after requiring there to be fewer than 10 hit tubes in the outer detector and the fit vertex position to be at least 200 cm from the nearest wall. The lower portion of this figure shows those events passing all cuts within 5 μs of a spill.

period is 2.2 s, so the fraction of time which we are vulnerable to background is $1.5\mu s/2.2s = 6.8 \times 10^{-7}$. If K2K runs for six months per year for five years, the total expected background from atmospheric neutrinos will still be only 0.012 events. Unfortunately, atmospheric neutrinos are not the only source of background. The purpose of the maximum 50000 p.e. cut is to reject the much more frequent through going muons that penetrate the detector.

5.1.2 Outer Detector Events

Outer detector events aren't as clean to handle as fully contained events. Because at most one of the starting or the ending point of the track is known, it's not possible to measure the energy of the neutrino. Furthermore, it's not possible to place a fiducial volume cut on these events, so rejecting cosmic ray muons becomes much more difficult.

The systematic errors associated with outer detector events are not at all well understood. For this reason these events are not currently used in the oscillation analyses. This section describes an incomplete study of the outer detector events observed through June of 2000 only.

To select these events, we use four cuts in addition to the timing window cut. First, we require at least 10 hits in the OD. This eliminates low energy triggers and is the basic definition of an OD event. Next, we eliminate events which have 50 or more OD hits within a 500ns time window. Cosmic ray muons tend to produce more light that beam neutrinos. Then we examine the clustering of the hit tubes. If the tubes form more than one cluster, they're probably the entrance and exit points of a cosmic ray muon. We require less than two clusters. Finally we require less than 30000 p.e. in the inner detector.

If the outer detector Monte Carlo is to be trusted, these cuts eliminate 96% of background events while retaining 89% of the signal. Despite these cuts, the background rate is non-negligible. Figure 5.2 shows the timing distribution for events passing the cuts. As with the inner detector events, we apply a 1.5 μs timing window cut.

About 8000 background events per day pass the geometry cuts, so we should expect about 5 background events over the course of the 5 year running time.

5.2 The Events

Figures 5.3 and 5.4 show the event displays of typical fully contained single ring muon-like and electron-like events in Super–Kamiokande. Muon-like

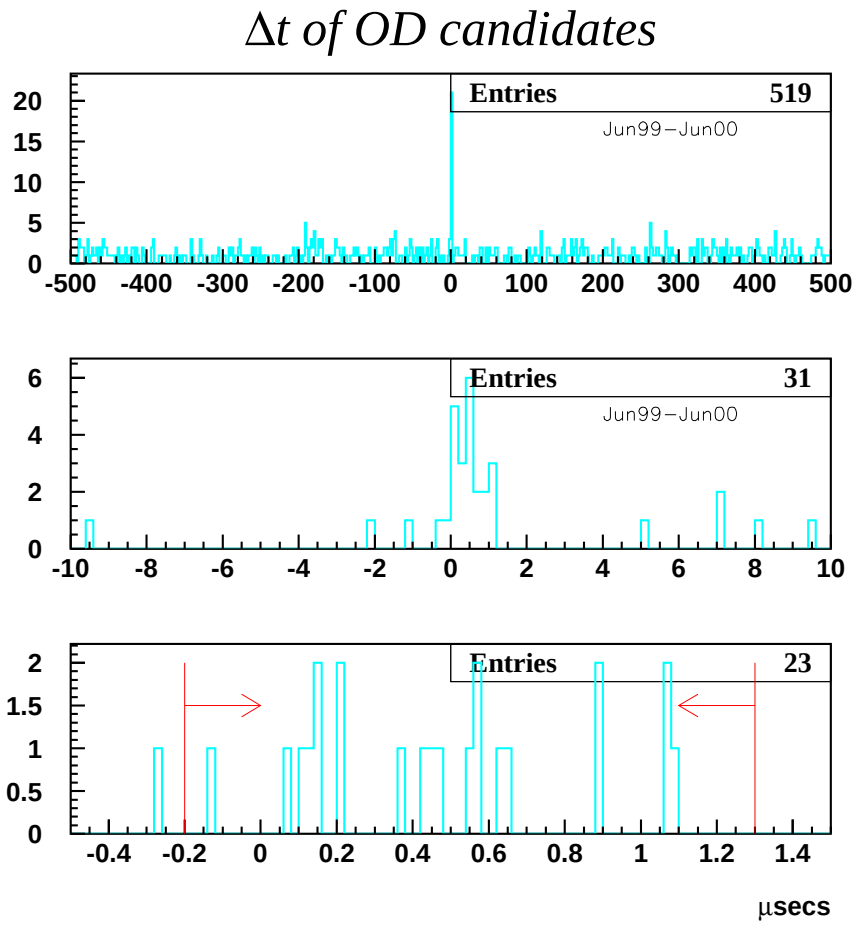

Figure 5.2: K2K Outer Detector event ΔT distribution. Here, the same data is plotted on three different scales to show the relationship between data and background. Although the OD events are not background free, there is still a very clear signal.

Category	Observed	Expected (No Osc.)
Fully Contained Fiducial Volume	56	$80.6^{+7.3}_{-8.0}$
FC FV Single Ring	32	48.4 ± 6.7
FC FV SR Muon-like	30	44.0 ± 6.8
FC FV SR Electron-like	2	4.4 ± 1.7
FC FV Multi-Ring	24	32.2 ± 5.3

Table 5.1: Super–Kamiokande event summary

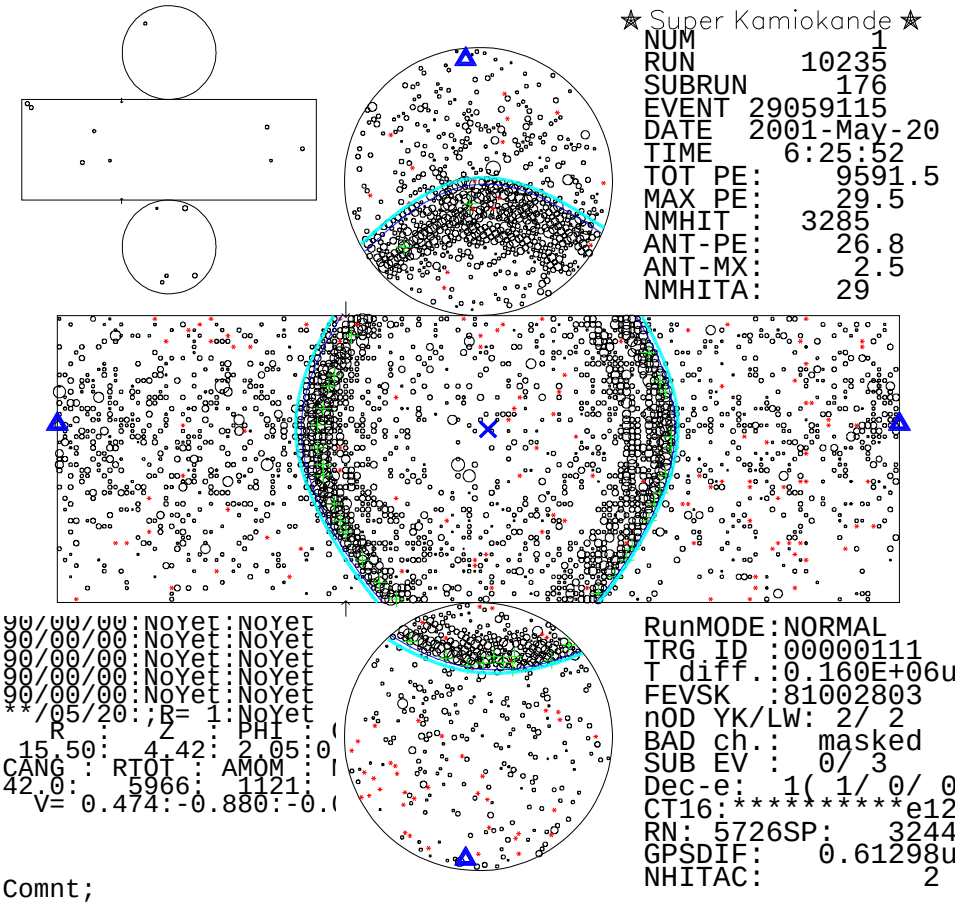

Figure 5.3: A typical one ring muon-like K2K neutrino event in Super–Kamiokande.

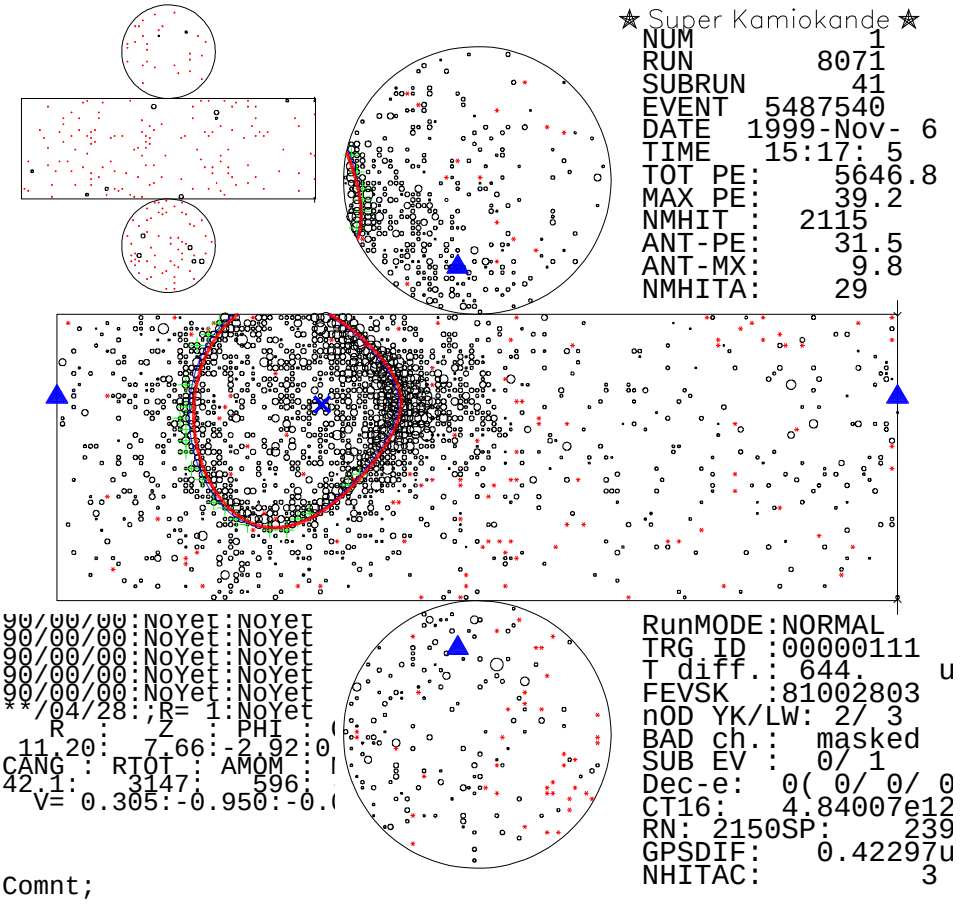

Figure 5.4: A typical one ring electron-like K2K neutrino event in Super–Kamiokande. Because an electron creates an electromagnetic shower as it moves through the detector, the Čerenkov ring is much fuzzier than those found in a muon-like events.

events are characterized by crisp, well defined edges, while electron-like events are fuzzy and blurred. This is because a muon ring is the result of the Čerenkov radiation from a single particle, while an electron ring is the superposition of rings formed by several hundred electrons created in an electromagnetic shower. Furthermore, since each electron is much lighter than a muon, it's more easily scattered by other particles in the target medium. Table 5.1 shows the distribution of all fully contained fiducial volume K2K event candidates observed in Super–Kamiokande to date. The number of events observed is fewer than that expected in the absence of oscillation in every event category.

Figure 5.5 shows the basic vertex and direction distributions for the fully contained events. The vertices cluster slightly toward the direction of KEK, as is to be expected. The acceptance for a fully contained event is higher further upstream in the detector.

Figure 5.6 shows the event timing distribution in units of protons on target since the start of the experiment. For the fully contained fiducial volume data, the Kolmogorov Smirnov test for linearity estimates that 43.1% of all such experiments would have less linear distributions than what we have observed.

The reconstructed neutrino energy of the 30 single ring muon-like events in the fiducial volume are shown in Figure 5.7.

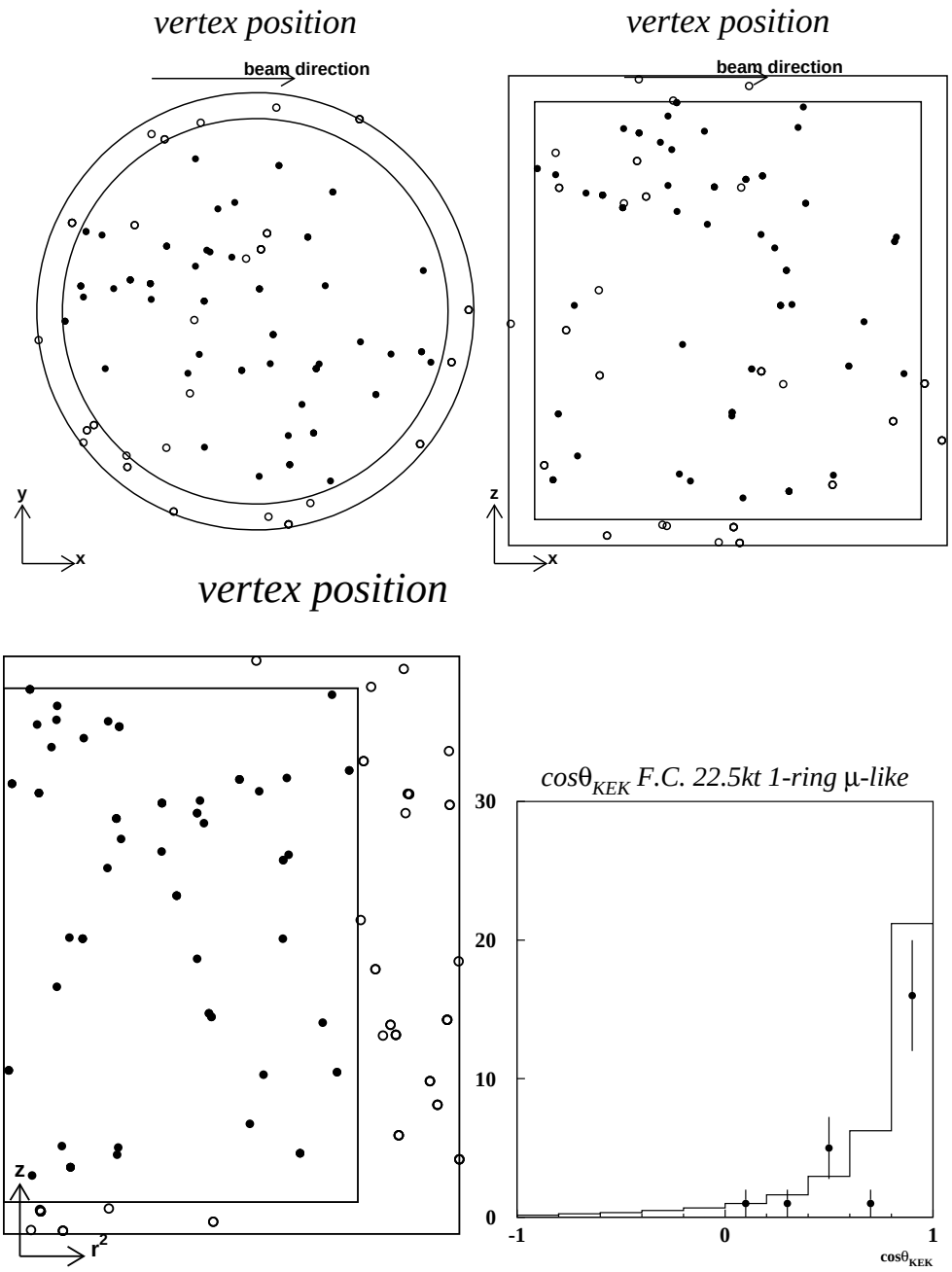

Figure 5.5: Vertex position and direction distributions for fully contained Super–Kamiokande events. Filled circles represent fiducial volume events, while open circles represent fully contained events with vertices which fit outside the fiducial volume. The plot in the lower right shows the distribution of the cosine of the opening angle between the muon direction and the expected neutrino direction for neutrinos coming from the KEK beam. The line histogram is the expectation for unoscillated Monte Carlo.

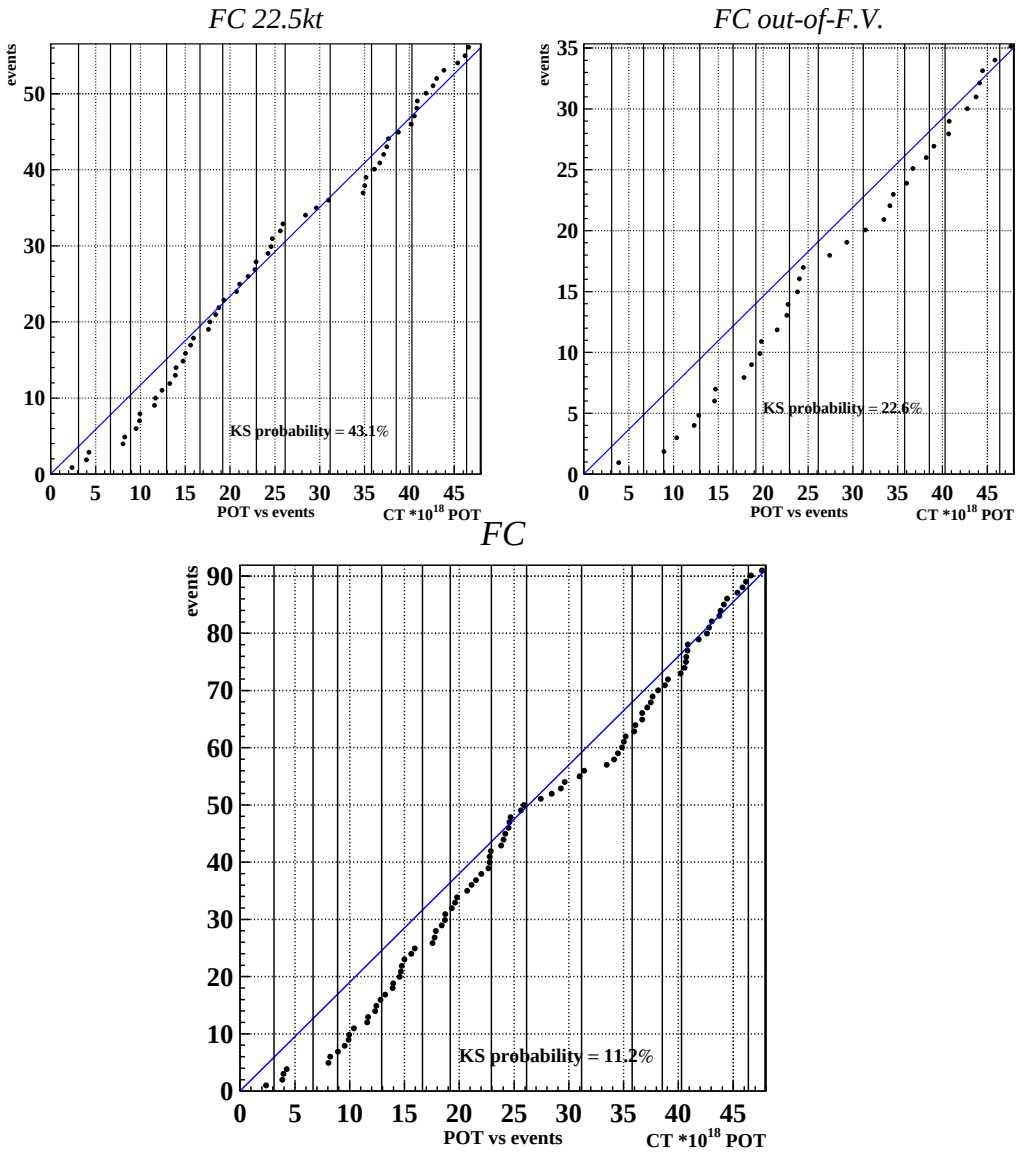

Figure 5.6: Super–Kamiokande event arrival time as a function of protons on target. Distributions are shown for events in the fiducial volume (top left) out of the fiducial volume (top right) and combined (bottom). In each plot, the data has been compared to the average event rate for that sample using a Kolmogorov Smirnov test, with results of 43.1%, 22.6%, and 11.2% respectively.

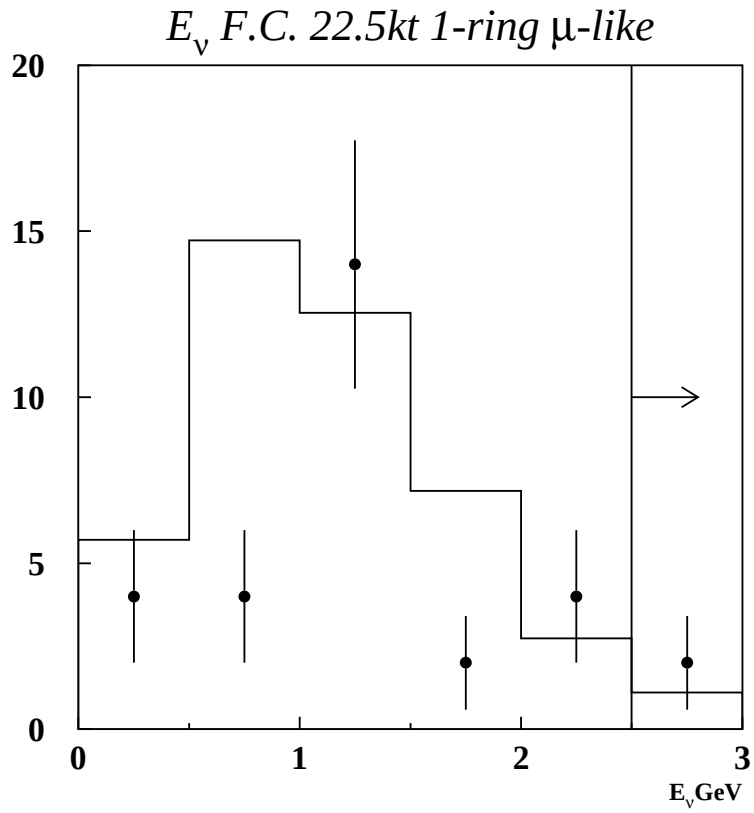

Figure 5.7: Super–Kamiokande event estimated neutrino energy assuming quasielasticty for all observed fully contained fiducial volume single ring muon-like events.

Chapter 6

Oscillation Parameters

We have seen that the nature of two-flavor neutrino oscillations is governed by two fundamental parameters, Δm^2, the difference of the squares of the masses of the mass eigenstates, and θ, the mixing angle between these states.

In this chapter we will discuss procedures to interpret our observed number of events into "allowed" or "excluded" regions in the Δm^2 vs. $\sin^2 2\theta$ parameter space. We use various methods to compute the probability, given our statistical and systematic errors, that our observed data is consistent with our expected observation for each point in this parameter space. This will allow us to draw contours around regions of likely values and place limits on the allowed regions of these parameters.

The difference between allowed and excluded regions is often misunderstood. Whenever one draws an allowed region, there is an implicit assumption that the underlying theory is correct, *i.e.* that there is a point in the parameter space which is the true point. An exclusion region makes no such assumption. Because of this, an excluded region is not necessarily the inverse of an allowed region. It is not inconsistent for a single point to be both allowed and excluded, but all points which are not excluded must be allowed and any point which is not allowed must be excluded. It is possible to exclude the entire parameter space, but there must always be an allowed region.

In our case, the underlying theory is the neutrino oscillation framework. It's important to note that by taking either θ or Δm^2 to zero, the oscillation probability goes to zero. This means that the case of non-oscillation is covered within the framework of the oscillation equations, so drawing an allowed region in the Δm^2 vs. $\sin^2 2\theta$ parameter space does not require an assumption that neutrinos actually oscillate.

6.1 Calculating the Confidence Limits

We will consider two independent methods for extracting the oscillation parameters from our data. The first approach uses only the total number of events expected compared with observation. This method works well with just a handful of events. The second approach utilizes the energy dependence of neutrino oscillations and the shape of the reconstructed neutrino energy spectrum to more tightly constrain the allowed parameter region, but requires higher statistics to be effective. We will then combine these approaches to eke as much information out of our data as possible.

One important difference between these approaches is that by using just the number of observed events, it is not possible to find a "best fit point" in a two dimensional parameter space. Instead, the χ^2 minimum will be a curve in this space. However, this is sufficient to distinguish between oscillation and non-oscillation cases.

6.1.1 The Simple Method

The simplest possible approach to analyzing this data is to compare the number of observed events to the number of expected events, accounting for statistical and systematic errors, and derive a probability based on the χ^2 for each point in the parameter space. We observed 56 fully contained neutrino interactions at Super–Kamiokande but expected $80.6^{+7.3}_{-8.0}$ in the absence of oscillations. We define the χ^2 as follows:

$$\chi^2 = \frac{(n-\mu)^2}{\sigma_{sys}^2 + \sigma_{stat}^2} \tag{6.1}$$

where n is the number of observed events, μ the expected number of events for that set of oscillation parameter values, σ_{sys} the total systematic error, and σ_{stat} the total statistical error.

Here we assume that systematic and statistical errors are independent and add them in quadrature. This χ^2 is then converted to a probability using the standard χ^2 relation for one degree of freedom. There has been some debate as to whether one degree of freedom is appropriate for this case, and I assert that it is. There is only one measurement here, the number of events observed, and no free parameters. This is not a fit, since nothing is allowed to float, so the probability distribution for one degree of freedom is the correct one to use.

It is tempting to assign σ_{stat} the value of the square root of the number of observed events on the grounds that this is the statistical error on the mean number of events which we would expect to observe if we were to repeat the

experiment, but this is not value we want. We are doing a hypothesis test that our observation of 56 events is consistent with a theoretical expectation. There is no statistical uncertainty on the actual number of events which we have observed. It is nonsensical to ask, "What is the probability that our observation of 56 events would fluctuate to our expectation?" We have observed this number of events and that will not change. What we need to ask is, "What is the probability that a Poisson distribution with our expected mean would produce a result as low as we have observed?" When phrased this way it is clear that σ_{stat} is the square root of the expectation, not the observation.

The proper treatment of σ_{sys} is somewhat less clear. The difficulty comes in with handling error correlations between different portions of the energy spectrum. The correct way to do this is to use the Monte Carlo simulation to fully map out the error space and deduce a correlation matrix for such errors, but as of this writing this work is incomplete. In this section I will include three different treatments for σ_{sys}, which I'll call "liberal", "moderate", and "conservative"[1]. While none of these approaches is fully mathematically correct, they do give us a general impression of what the K2K experiment can say about neutrino physics.

The liberal approach is the simplest. We have calculated the systematic error on the number of expected neutrino events in the absence of oscillations as described in the previous chapter. We can simply take the same relative error in the presence of oscillations, ignoring possible correlations between errors in different parts of the spectrum.

The allowed region given by this approach is shown in Figure 6.1. In this analysis, the χ^2 minimum is precisely zero for all points in the graph for which the expected value is the observed value. Because of this, these contours represent both an allowed region and an exclusion region.

The liberal approach is reasonable, but not thorough, because it doesn't take into account that the systematic error on the expected flux is not evenly distributed across the energy spectrum. If, for example, oscillation were to occur in a particular energy band where we have low error, the relative error should increase for that set of oscillation parameters. For example, imagine as a pathological case, a line spectrum consisting of only two lines containing equal flux but with negligible error on the low energy line and 20% error on the higher energy line. This gives a 10% error on the integrated spectrum. If for a given set of parameter values the low energy line were to fully oscillate,

[1] It has been suggested by some that these treatments would be better called moderate, conservative, and right-wing-fundamentalist.

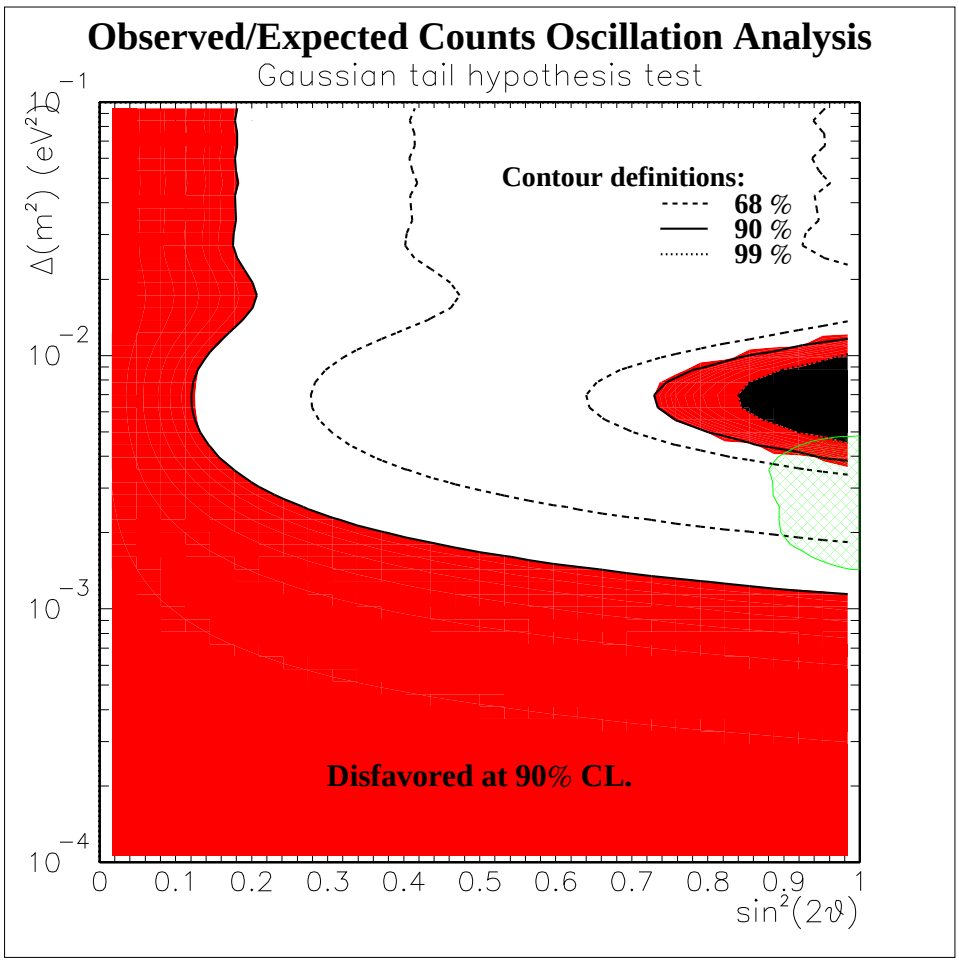

Figure 6.1: Oscillation allowed region, single bin χ^2 method, with liberal interpretation of systematic errors. The Super–Kamiokande atmospheric neutrino 90% allowed region is denoted by the hatched region in green.

but the high energy line was only lightly affected by oscillation, then the error on the expectation for those parameter values should be 20%, not 10%. If this situation seems contrived, it is, but it illustrates the point that the liberal approach may be undercounting errors. The moderate approach is to take the absolute error on the neutrino event rate in the absence of oscillation and apply it across the board for all values of $\sin^2 2\theta$ and Δm^2. This gives the correct error in the case of the two line spectrum and conservatively overestimates the error for more likely scenarios. Figure 6.2 shows the allowed region using this method.

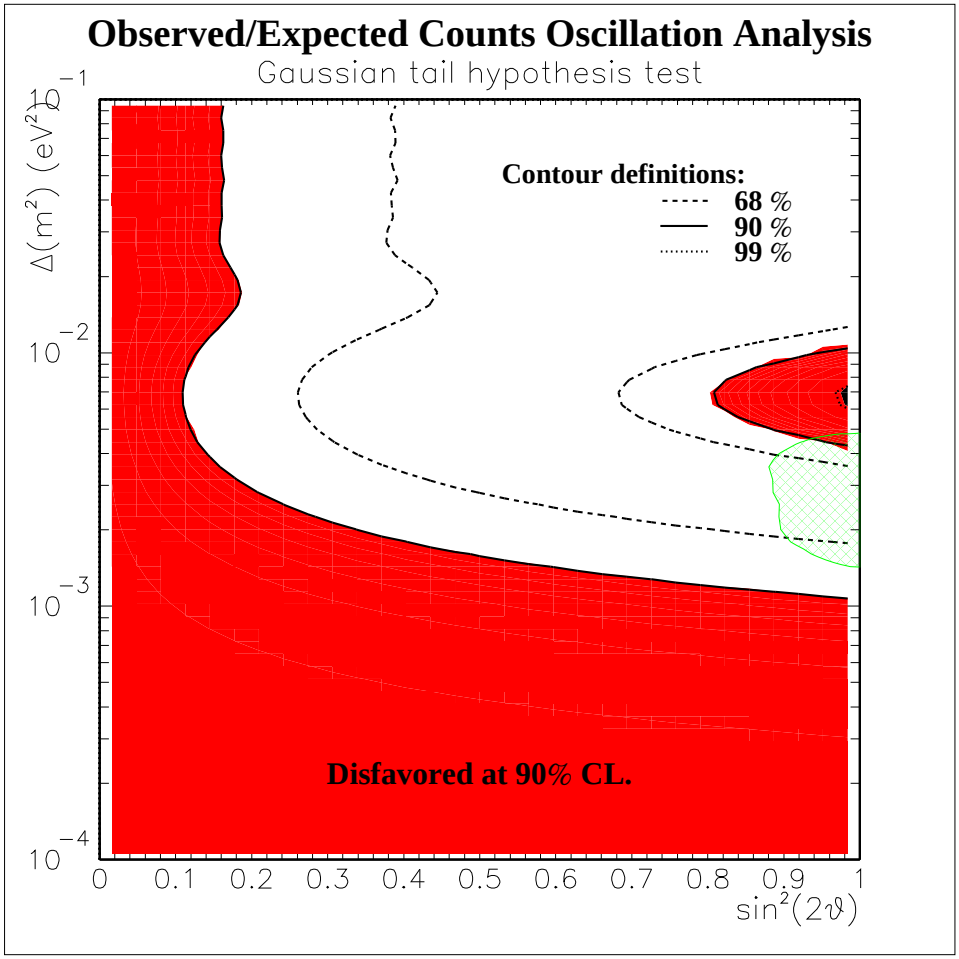

Figure 6.2: Oscillation allowed region, single bin χ^2 method, with moderate interpretation of systematic errors. The Super–Kamiokande atmospheric neutrino 90% allowed region is denoted by the hatched region in green.

Although using the absolute systematic error is more conservative, this value of $80.6^{+7.3}_{-8.0}$ was itself calculated assuming some cancellation of correlated errors specifically for the case of non-oscillation. The final and most conservative approach presented here attempts to separate the effects of uncertainties of the shape of the energy spectrum from its normalization.

Any shape which can be described by series of N points with correlated errors, can also be expressed as N points with $N+1$ errors, with one error on the overall normalization, and N "shape errors" on the values of each point. When the normalization error is taken out in this fashion, the shape errors are, in general, anti-correlated. In other words, if one bin were to move up, another bin (or bins) must move down to keep the normalization fixed.

The correlation matrix of the shape errors for the expected neutrino spectrum is not well known. Since it is conservative to treat anti-correlated errors as uncorrelated errors, we will assume no correlation and aad the shape errors in quadrature. The overall normalization error is taken as 9.0%, and the flux weighted quadrature sum of shape errors is 7.9% (6.14 events). The only other important systematic error is the neutral current fraction. The conservative estimate of 30% uncertainty in the neutral current fraction gives only a 3.3 event error on the number of events. This does not depend on the oscillation parameters since the rate of neutral current events is not affected by oscillations. The final systematic error term is then just the quadrature sum of the absolute errors from the shape and neutral current fraction with the relative error from the normalization.

$$\sigma_{sys} = (\sigma_{shape} + \sigma_{NC})\mu_{noosc} + (\sigma_{norm})\mu_{osc}$$

where σ_{shape}, σ_{NC}, and σ_{norm} are the systematic errors due to shape, neutral current, and normalization expressed as a fraction of the expectation. Here we distinguish between μ_{noosc}, the expected observation in the absence of oscillation, and μ_{osc}, the expected observation at a particular $\sin^2 2\theta$ and Δm^2. Adding these three errors in quadrature gives a null oscillation expectation of 80.6 ± 10.0 events, which is a larger error than our official expected number of $80.6^{+7.3}_{-8.0}$ because we have ignored the correlation of errors in the shape of the spectrum. The allowed region given by this method is shown in Figure 6.3.

This final figure is an official K2K result.

6.1.2 The Energy Dependent Method

As we have seen in Chapter 4, neutrino oscillation is an energy dependent phenomenon, so we can get much more resolving power if we take the observed

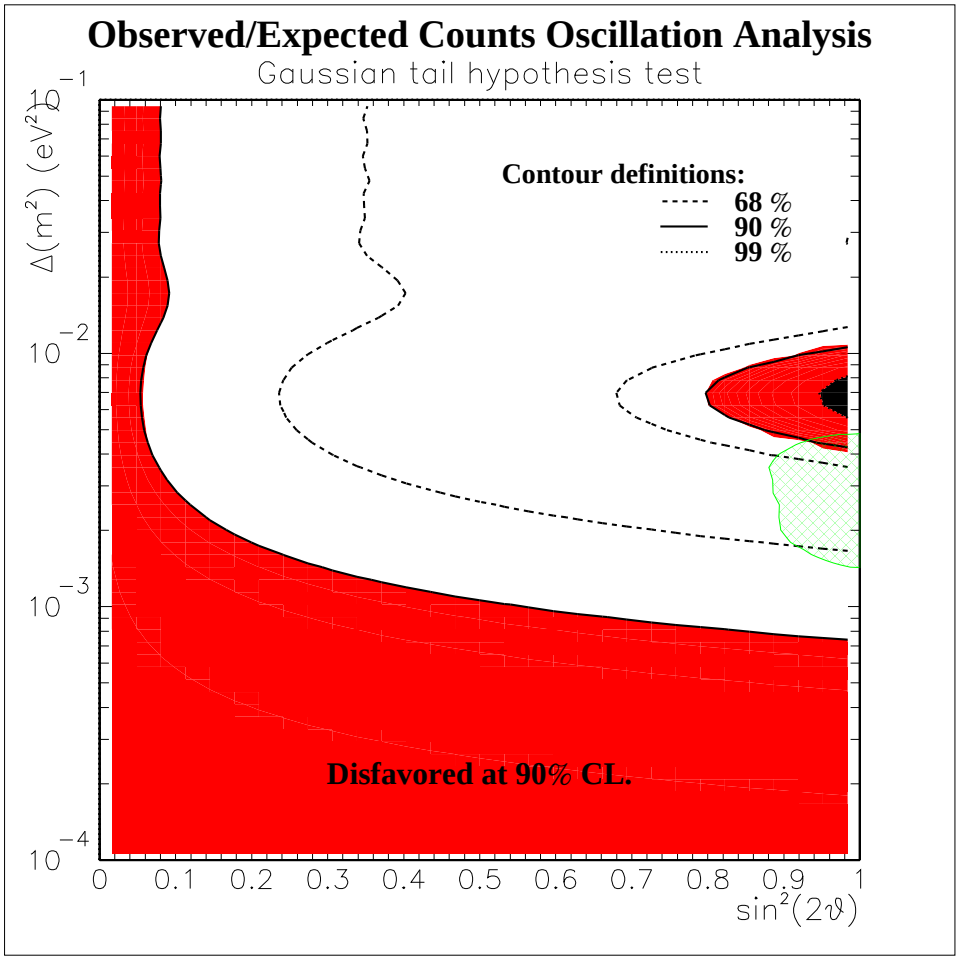

Figure 6.3: Oscillation allowed region, single bin χ^2 method, with conservative interpretation of systematic errors. The Super–Kamiokande atmospheric neutrino 90% allowed region is denoted by the hatched region in green. This plot is a K2K official result.

energy into account. The results presented in this section are preliminary in nature and illustrate the techniques that can be used to a final oscillation result once the energy spectrum systematic errors are completely understood. Nothing in this chapter is an official K2K result.

Maximum Likelihood Fitting

When the statistics of experimental data are limited, as is the case for K2K, a maximum likelihood fit is commonly used to extract the most information out of the event sample[42]. To perform a maximum likelihood fit to our data, we use the expected observable energy spectrum for each Δm^2 and $\sin^2 2\theta$ to calculate the probability of observing a given event at a given energy by simply taking the fraction of Monte Carlo events which reconstruct near that energy.

$$P(E) = \frac{n_{MC}(E)}{N_{MC}}$$

where $P(E)$ is the probability of observing an event at energy E, $n_{MC}(E)$ is the number of Monte Carlo events generated at energy E, and N_{MC} the total number of Monte Carlo events generated. The numbers of Monte Carlo events are weighted by one minus the oscillation probability for each of those events. The likelihood for a given point in the parameter space is then given by the product of the probabilities for each observed event.

$$L = \prod_{i=1}^{N} P(E_i)$$

where L is the likelihood of the parameter set, N is the total number of events in the data and E_i is the energy of each event.

Performing the likelihood fit is then just a matter of calculating L for all points on a grid in $\sin^2 2\theta$ and Δm^2 and selecting the point of maximum likelihood. The best fit point is at $\sin^2 2\theta = 1$ and $\Delta m^2 = 3.25 \times 10^{-3}$. A comparison of the data spectrum to the non-oscillated and best fit point spectra is shown in Figure 6.4.

To convert the likelihood values to allowed region confidence levels, it is customary to assume a Gaussian error distribution. In other words, if the experiment were to be repeated many times, the distribution of best fit points would form a Gaussian centered on the true value. If this is the case, the nth σ contour for a single experiment is given by those points with a likelihood lower than the best fit point by a factor of $e^{-n^2/2}$. Unfortunately, this assumption is not valid for us.

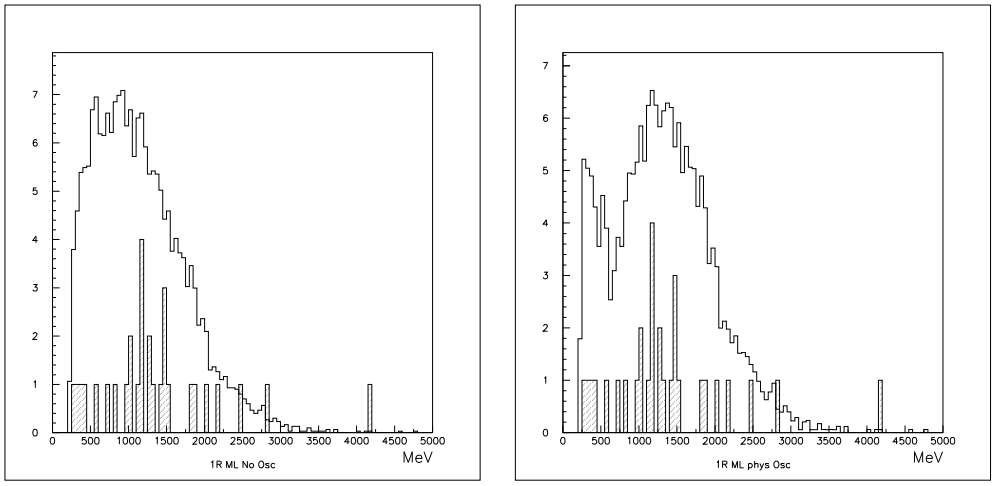

Figure 6.4: The predicted single ring muon-like event reconstructed energy spectrum for nonoscillated (left) and physical best fit oscillated (right) spectra. Both Monte Carlo data sets are arbitrarily normalized to 200 events and overlaid with the 30 observed events in the data.

Although we know that the value of $\sin^2(2\theta)$ must be bounded between 0 and 1, within the context of the fit it is possible to generate values for $\sin^2(2\theta)$ outside of this region which fit the observed data better than points between 0 and 1. We call the region between 0 and 1 the "physical region", and refer to its compliment as the "non-physical region". If the true values of the oscillation parameters are near one of the boundaries of the physical region, there will be a significant amount of probability assigned by the fit to the non-physical region. Simply chopping the allowed region at the boundary means that our Gaussian is no longer a Gaussian, and the confidence region we would draw would therefore not be an accurate representation of our knowledge. If the best fit point fell outside the physical region, then our allowed region would be too small. If the best fit point was inside the physical region, then the allowed region would be too large.

There are two established methods to correct for this. The more traditional approach is to continue to assume a Gaussian likelihood distribution, integrate over the entire space, including the non-physical region, and normalize the likelihood function to one. To assign a confidence level to a point in the physical region, integrate over the portion of the Gaussian that is in the physical region.

A more recent proposal by Feldman and Cousins[43] eschews this approach and abandons all assumptions that the error distribution should be Gaussian.

In this method, a toy Monte Carlo is created to simulate many experiments for all points in the parameter space. In this way, the actual shape of the error distribution is mapped out. A point is then included in the 90% allowed region if the ratio of its likelihood to the best fit point likelihood is at least as high as 90% of the MC trials at that parameter set. This method is mathematically more robust, but at the same time more CPU intensive.

Both of these methods are described in detail as applied to the Super–Kamiokande atmospheric neutrino oscillation fits in [44]. In that case, the toy Monte Carlo (Figure 6.5) showed that the Gaussian approximation of the error distribution was in fact quite good and the two approaches showed quite similar results. However, in our case (Figure 6.6) our statistics are small enough that a particularly unlucky, but still likely set of interactions can occur which fit quite far into the non-physical region. This gives our error distribution non-Gaussian tails which cannot be properly handled using a Gaussian approximation.

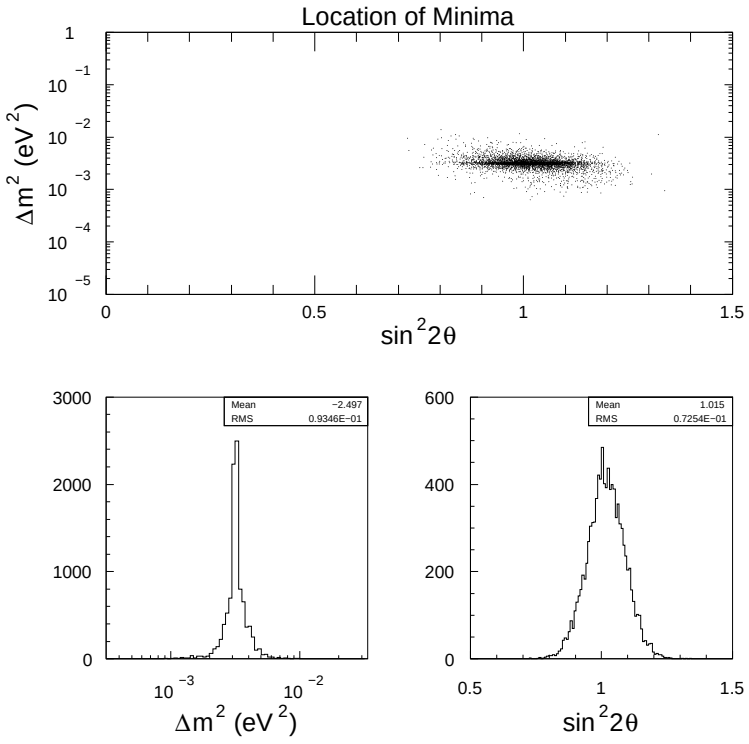

Figure 6.5: Distribution of χ^2 minima for 10,000 simulated measurements based on 736 days of atmospheric neutrinos.[44] The fit points cluster around the true point in a close approximation to the Gaussian distribution.

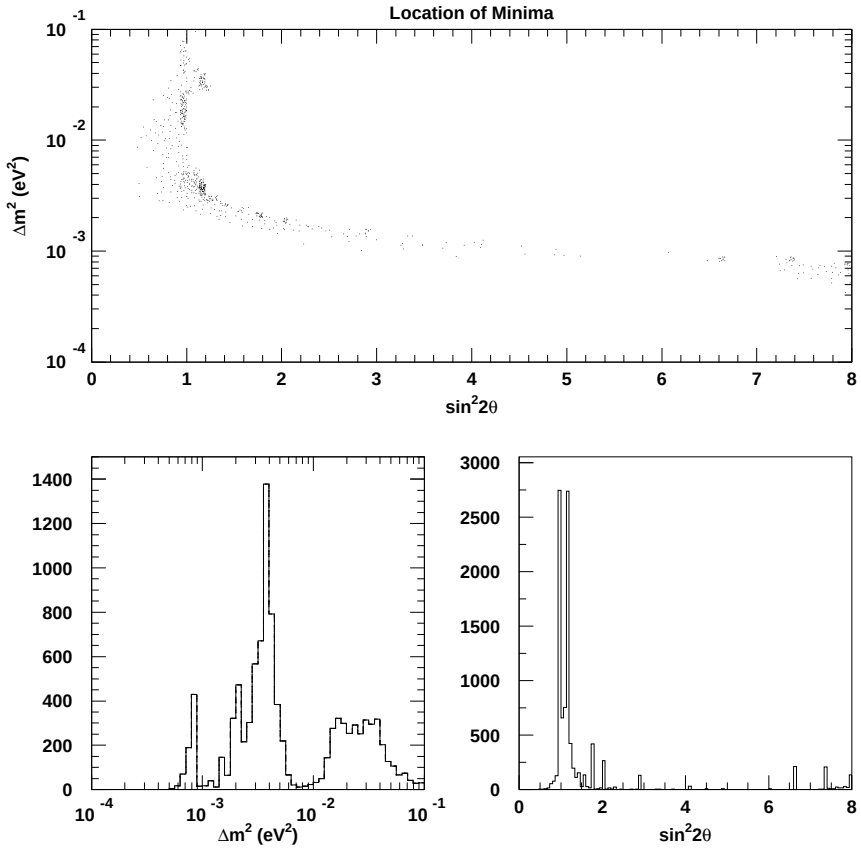

Figure 6.6: Distribution of maximum likelihood best fit points for 10,000 simulated measurements for the K2K experiment. Unlike the Super–Kamiokande case, the distribution of best fit points has large tails far from the best fit point which do not fit a Gaussian distribution.

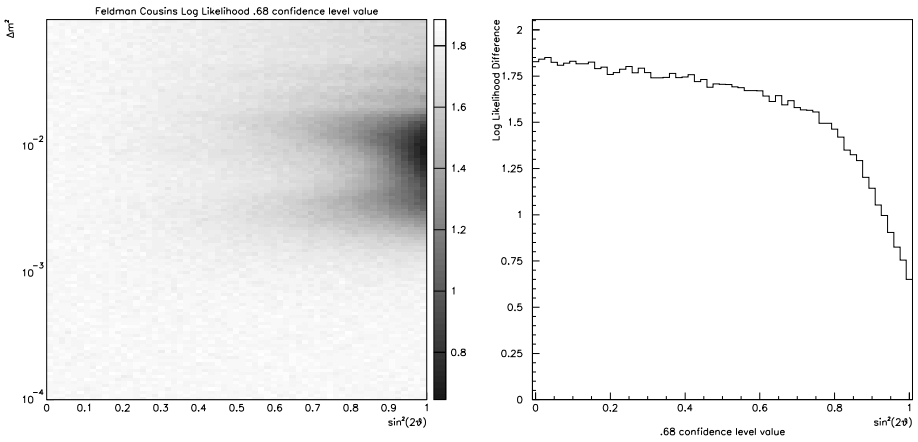

Figure 6.7: Feldman & Cousins likelihood map showing the value of the log likelihood difference between the true point and the best fit point which at the 68 % confidence level for the entire parameter space, and a slice along $\Delta m^2 = 0.01$. In a parameter space without borders and Gaussian errors this plot would be flat at 0.5.

Systematic Error on the Far Detector Spectrum

The beam Monte Carlo prediction of the observed events at the far detector is based on the Sanford Wang parameterization of pion production at the proton target. This parameterization has eight adjustable parameters denoted as $\mathcal{W}_i$ in Equation 6.2.

$$\begin{aligned} \mathrm{E} \times \left(\frac{\mathrm{d}^3\sigma}{\mathrm{dp}^3}\right)(\mathrm{mbarns/GeV^2}) &= \sigma_{total}\mathcal{W}_1 \mathrm{P}_\pi^{\mathcal{W}_2} \cdot (1 - \mathrm{P}_\pi/\mathrm{P}_\mathrm{p}) \\ &\times \mathrm{e}^{-\left(\mathcal{W}_3 \mathrm{P}_\pi^{\mathcal{W}_4}/\mathrm{P}_\mathrm{p}^{\mathcal{W}_5}\right)} \\ &\times \mathrm{e}^{-\left(\mathcal{W}_6\theta_\pi\left(\mathrm{P}_\pi - \mathcal{W}_7 \mathrm{P}_\mathrm{p}(\cos\theta_\pi)^{\mathcal{W}_8}\right)\right)} \end{aligned} \quad (6.2)$$

It is these eight parameters which account for the bulk of our uncertainty in the far detector prediction. A χ^2 fit was done using data from Cho and Dekkers, and the errors from this fit give us errors on each of these parameters and their correlations.

$\mathcal{W}_1$ is the overall normalization and has no effect on the spectral prediction. Also, since we work with a monochromatic proton beam, $\mathcal{W}_3$ and $\mathcal{W}_5$ both have the same effect so they may be combined. This give us six values we can twiddle.

To include the effects of this error in the allowed region calculation we'll employ the standard Baysian[41] relation $P(A) = \int P(A|B)P(B)dB$. Here, A represents the probability of point in the $sin^2(2\theta) \cdot \Delta m^2$ parameter space, and B represents a Sanford Wang parameter $\mathcal{W}$. Because it is highly CPU intensive to computer this integral fully, we will vary each $\mathcal{W}$ by one standard deviation in each direction, producing 64 alternate Monte Carlo predictions. The probability at each point is then the integral of the probabilities given for that point by each alternate prediction multiplied by the probability for that prediction.

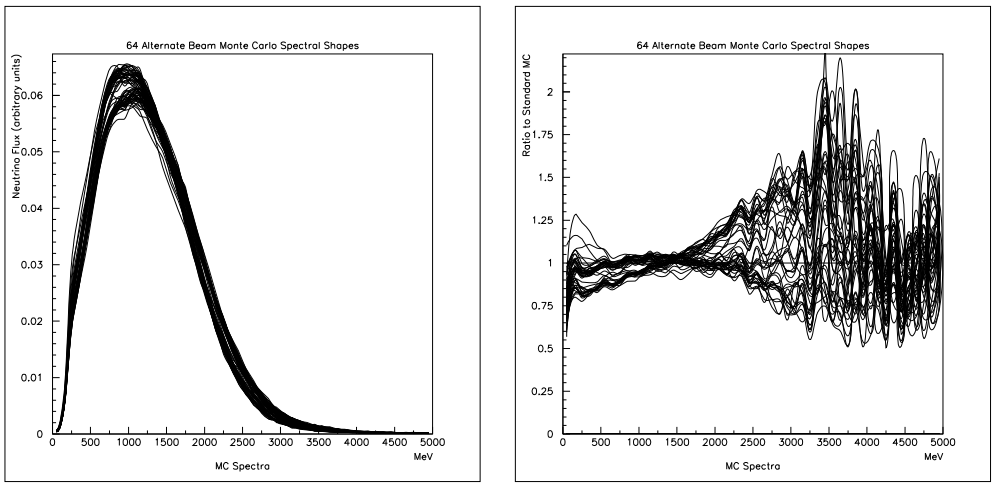

Figure 6.8: The standard beam Monte Carlo neutrino flux prediction superimposed with 64 alternate models created by adjusting six of the Sanford Wang parameters by $\pm 1\sigma$. The left portion shows the absolute flux (in arbitrary units) and the right portion shows the spectra plotted relative to the standard case. All spectra are normalized to the same total flux, so only changes in shape are presented here. The wild oscillations seen in the high energy tail of the relative plot are due to statistical fluctuations in the Monte Carlo sample. The effects of neutrino interaction cross sections are not included in this figure.

Figure 6.9 shows the allowed region using this method. The statistical fluctuations in the toy Monte Carlo are responsible for the wobbly lines denoting the confidence levels. This figure uses the shape of the spectrum alone and its predictive power is limited. The resulting allowed region is essentially controlled by the deficit of events at lower energies. We see islands of higher probability at values of Δm^2 which cause oscillation in this energy region interleaved with regions of low probability at values which suppress other energies.

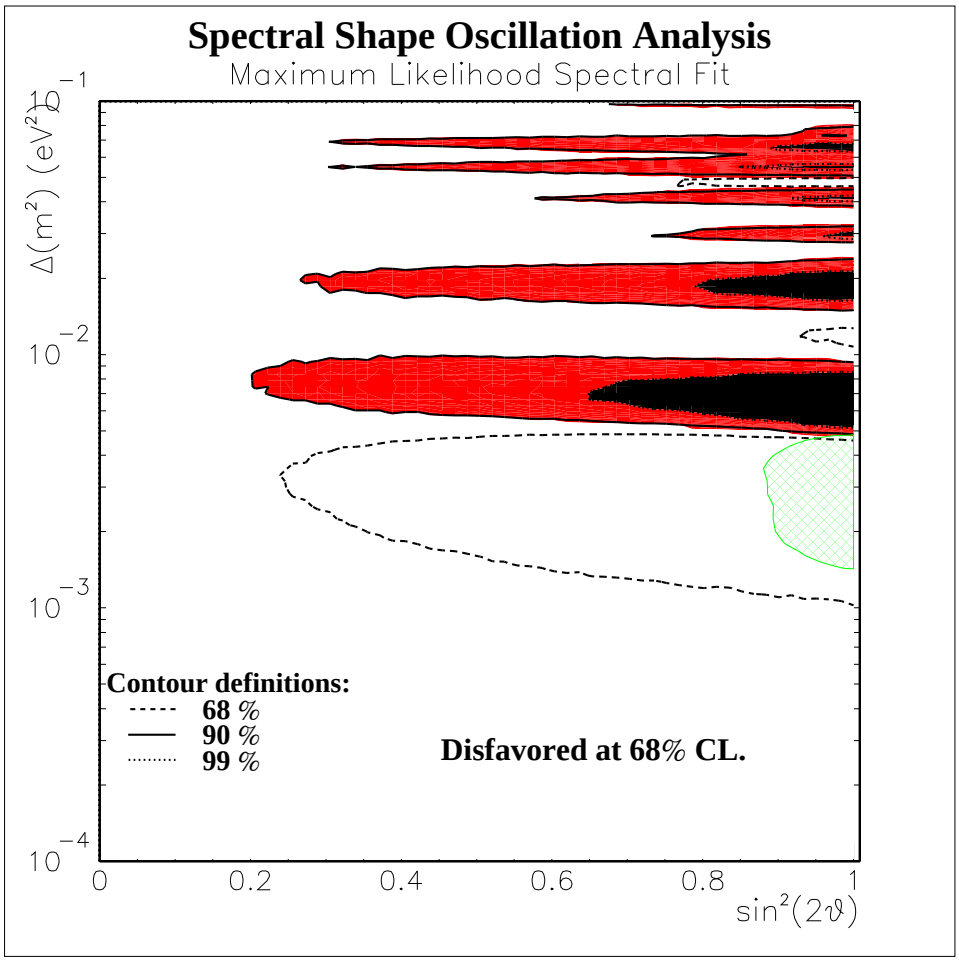

Figure 6.9: Oscillation Allowed Region, Maximum Likelihood Spectral Fit

The importance of this technique is that it can easily be combined with the method that uses only the measurement of the number of events.

Combined Allowed Regions

To combine both the spectral shape and event rate information all that is needed is to repeat the spectral shape calculation but alter the probability calculation used to compute the likelihoods. The probability of a set of events is simply the product of probabilities of observing each event at its energy, as above, multiplied by the χ^2 probability for the total number of events using the same relation described in Section 6.1.1. The rest of the calculation proceeds unaltered.

$$L = \prod_{i=1}^{N} P(E_i) \times PROB(\frac{(n-\mu)^2}{\sigma_{sys}^2 + \sigma_{stat}^2}, 1 d.o.f.)$$

Figure 6.10 shows the allowed region using both the event rate and spectral shape distribution. The best fit point is at $\sin^2 2\theta = 1$ and $\Delta m^2 = 2.74 \times 10^{-3}$. The null oscillation case is ruled out at the 99% confidence level.

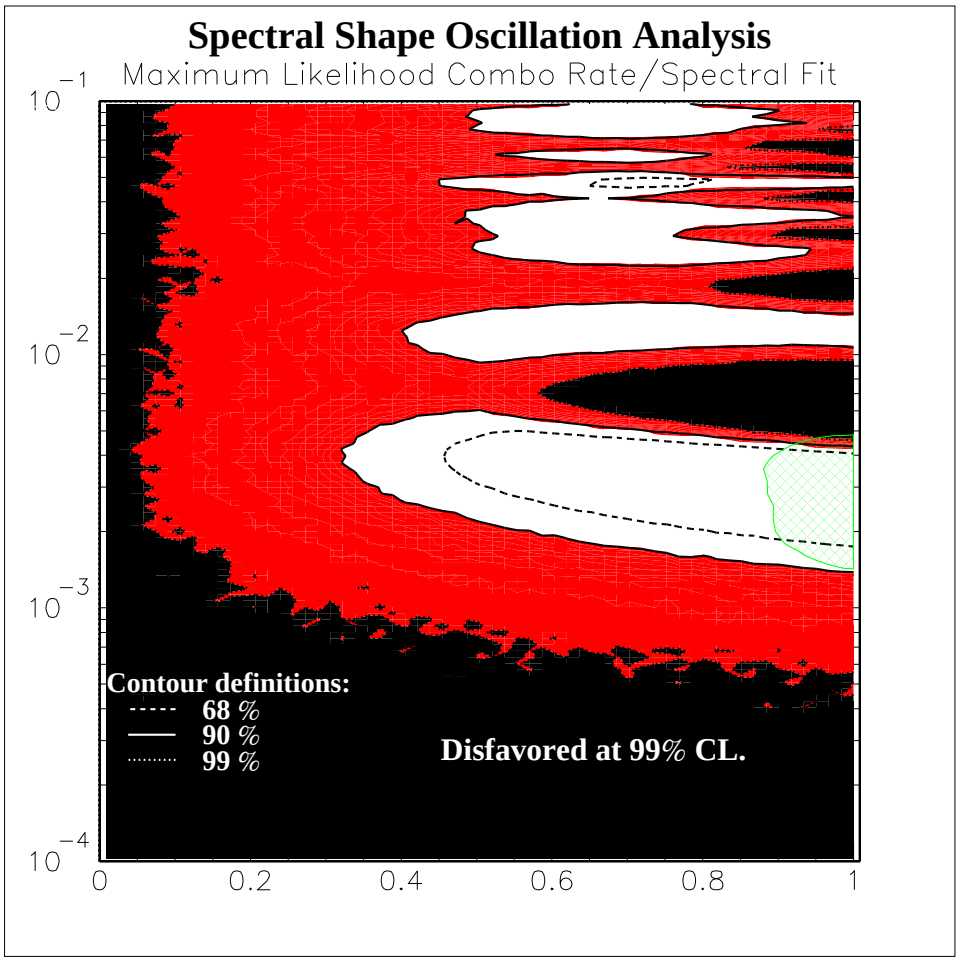

Figure 6.10: Oscillation Allowed Region, Combined Method

Chapter 7

Conclusions and Future

7.1 Conclusions

A search for neutrino oscillations in the mode $\nu_\mu \rightarrow \nu_x$ was performed using data corresponding to 4.8×10^{19} protons on target in the K2K long baseline neutrino oscillation experiment[45].

The number of predicted events for non-oscillation at the Super–Kamiokande detector was $80.6^{+7.3}_{-8.0}$ events. The observation of only 56 events is sufficient to rule out the nonoscillation hypothesis at the 97% confidence level based on the event rate comparison alone.

The shape of the neutrino spectrum observed at Super–Kamiokande differed from the expected spectrum enough to rule out nonoscillation at the 68% confidence level. When information from the event rate and spectral shape are combined, nonoscillation is ruled out at the 99% confidence level.

The allowed regions acquired using all methods are consistent with the oscillation parameters obtained by the Super–Kamiokande experiment.

7.2 The Future

The K2K experiment is still largely limited by statistics. It was expected to run at least three more years, more than doubling its current exposure. Unfortunately, on November 12th, 2002 the Super–Kamiokande detector suffered severe damage caused by an apparent chain reaction implosion of about 60% of its photomultiplier tubes. Super–Kamiokande is expected to be rebuilt and it could be possible to resume taking K2K data as early as November of 2002.

Even without additional data, much work remains to be done. Of primary importance are continued tuning of the beam Monte Carlo and a more complete systematic error study.

In 2005 and beyond a new generation of long baseline neutrino oscillation experiments will begin taking data. The MINOS[46] experiment will fire neutrinos from the Fermi National Accelerator Laboratory in Chicago to a new far detector in the the Soudan mine, almost tripling the baseline used by K2K.

Another $\approx$ 730 km baseline experiment is under construction in Europe. The CERN Neutrino beam to Gran Sasso[47] (CNGS) uses the CERN Super Proton Synchrotron to produce a neutrino beam aimed at two neutrino detectors, Icarus and Opera, in Gran Sasso, Italy. This experiment is expected to start taking data some time shortly after MINOS.

In 2007 another long baseline experiment in Japan using Super–Kamiokande will go online. The JHF-Kamioka[49] neutrino project will use the Japan Hadron Facility's 50 GeV proton synchrotron to deliver a high intensity neutrino beam from the Japan Atomic Energy Research Institute in Tokai to the Super–Kamiokande site.

This next generation of experiments are designed not just to measure the disappearance of muon neutrinos, but also detect the appearance of tau neutrinos, especially at the CNGS experiment.

In the more distant future, high precision neutrino oscillation experiments may be made possible by the creation of high flux neutrino beams at a neutrino factory and very large neutrino detectors, such as UNO[48] or Hyper-Kamiokande.

Bibliography

[1] J. Chadwick, Verhandl. Dtsch. phys. Ges. **16**, 383 (1914).

[2] F. Reines and C.L. Cowan, Phys. Rev. **92**, 830 (1953).

[3] F. Reines and C.L. Cowan, Nature **178**, 830 (1953).

[4] J. N. Bahcall, N. A. Bahcall, G. Shaviv, Phys. Rev. Lett. **20**, 1209 (1968).

[5] R. Davis Jr., D. S. Harmer, F. Neely, Phys. Rev. Lett. **20**, 1205 (1968).

[6] V. Gribov, B. Pontecorvo, Phys. Lett. **28B**, 493 (1969).

[7] J. N. Abdurashitov *et al.* [SAGE Collaboration], Phys. Rev. C **60**, 055801 (1999). [astro-ph/9907113].

[8] W. Hampel *et al.* [GALLEX Collaboration], Phys. Lett. B **447**, 127 (1999).

[9] J. Bahcall, *john bahcall home page.* Available from: http://www.sns.ias.edu/∼jnb

[10] T. K. Gaisser. *Cosmic Rays and Particle Physics.* Cambridge University Press, 1990.

[11] M. F. Crouch *et al.*, Phys. Rev. D **18**, 2239 (1978).

[12] M. r. Krishnaswamy *et al.*, Pramana **19**, 525 (1982).

[13] D. Casper *et al.* [IMB Collaboration], Phys. Rev. Lett. **66** 2561 (1991).

[14] R. Becker-Szendy *et al.* [IMB Collaboration], Phys. Rev. **D46** 3720 (1992).

[15] K.S. Hirata *et al.* [Kamiokande Collaboration], Phys. Lett. **B205**, 416 (1988).

[16] K.S. Hirata *et al.* [Kamiokande Collaboration], Phys. Lett. **B280**, 146 (1992).

[17] M. C. Goodman [Soudan-2 Collaboration], Nucl. Phys. Proc. Suppl. **38**, 337 (1995).

[18] W. W. Allison *et al.* [Soudan-2 Collaboration], Phys. Lett. B **449**, 137 (1999) [hep-ex/9901024].

[19] C. Berger *et al.* [Frejus Collaboration], Phys. Lett. B **227**, 489 (1989).

[20] O. Perdereau [Frejus Collaboration], LAL-91-06 *Presented at Tests of Fundamental Laws in Physics: Rencontre de Moriond, Les Arcs, France, Jan 26 - Feb 2, 1991.*

[21] Y. Fukuda *et al.* [Super-Kamiokande Collaboration], Phys. Rev. Lett. **81**, 1562 (1998) [arXiv:hep-ex/9807003].

[22] C. Athanassopoulos *et al.* [LSND Collaboration], Phys. Rev. C **54**, 2685 (1996) [arXiv:nucl-ex/9605001].

[23] C. Athanassopoulos *et al.* [LSND Collaboration], Phys. Rev. Lett. **81**, 1774 (1998) [arXiv:nucl-ex/9709006].

[24] L. Borodovsky *et al.*, Neutrino Beam. Bnl-776 Experiment," Phys. Rev. Lett. **68**, 274 (1992).

[25] B. Armbruster *et al.*, Phys. Rev. C **57**, 3414 (1998) [arXiv:hep-ex/9801007].

[26] M. Apollonio *et al.* [CHOOZ Collaboration], Phys. Lett. B **466**, 415 (1999) [arXiv:hep-ex/9907037].

[27] J. E. Hill, [arXiv:hep-ex/9504009].

[28] J. E. Hill, UMI-99-36813.

[29] J. D. Jackson. *Classical Electrodynamics, Second Edition.* John Wiley & Sons, 1975.

[30] E. Segrè. *Nuclei and Particles, Second Edition.* Benjamin/Cummings Publishing Company, Inc., 1977.

[31] A. Suzuki *et al.*, Nucl. Inst. and Meth. **A329**, 299 (1993).

[32] R. Claus *et al.*, Nucl. Inst. and Meth. **A261**, 540 (1987).

[33] R. Becker-Szendy *et al.*, Nucl. Instrum. Meth. **A324** (1993) 363.

[34] S. Kawabata, *et al.,* Nucl. Instr. Methods **A270**, 11, 1988.

[35] Y. Ikegami, IEEE Trans. Nucl. Sci. **36**, 665, 1989.

[36] J. Kanzaki, *ZBS Primer.* Available from: http://nngroup.physics.sunysb.edu/∼sharkey/zbs

[37] Cho, *et al.* Phys. Rev. **D4**, 1967 (1971)

[38] C. L. Wang. Phys. Rev. **D16** 2196 (1997)

[39] Dekkers, *et al.* Phys. Rev. **137** 962 (1965)

[40] K. Ishihara. *Study of $\nu_\mu \to \nu_\tau$ and $\nu_m u \to \nu_{sterile}$ Neutrino Oscillations with the Atmospheric Neutrino Data in Super-Kamiokande* PhD thesis, University of Tokyo, 1999.

[41] R. Goodman. *Introduction to Stochastic Models.* Benjamin/Cummings Publishing Company, 1988.

[42] R.J. Wilkes, *Physics 576A: Experimental Particle Astrophysics Notes*, 1997. Available from: http://www.phys.washington.edu/∼jeff/courses/ph576

[43] G. Feldman, R. Cousins, Phys. Rev. **D57** 3873 (1998)

[44] M. Messier. *Evidence for Neutrino Mass from Observations of Atmospheric Neutrinos with Super-Kamiokande* PhD thesis, Boston University, 1999.

[45] S. H. Ahn *et al.* [K2K Collaboration], Phys. Lett. B **511**, 178 (2001) [hep-ex/0103001].

[46] A. Weber, Nucl. Phys. Proc. Suppl. **98**, 57 (2001).

[47] A. Ereditato, Nucl. Phys. Proc. Suppl. **100**, 200 (2001).

[48] M. Goodman, *et al.* [UNO Proto-collaboration], Preprint #SBHEP01-3, (2001). Available from: http://nngroup.physics.sunysb.edu/uno

[49] Y. Itow *et al.*, arXiv:hep-ex/0106019.

[50] N. Tagg, *On Egg Sandwhiches and Neutrinos*, 1998. Available from: http://ccshst07.cs.uoguelph.ca/~ntagg/eggsandwich/eggsandwich.html

[51] J. Peltoniemi, *The Ultimate Neutrino Page*. Available from: http://cupp.oulu.fi/neutrino